ENGINEERING OF NOVEL FUEL CELL CATHODE INTERFACES WITH SURFACE-INITIATED IONOMER FILMS BASED ON MODIFIED POLYNORBORNENE

By

Bradley Joseph Berron

Dissertation

Submitted to the Faculty of the

Graduate School of Vanderbilt University

in partial fulfillment of the requirements

for the degree of

DOCTOR OF PHILOSOPHY

in

Chemical Engineering

May, 2008

Nashville, Tennessee

Approved:

Professor G. Kane Jennings

Professor Paul E. Laibinis

Professor Kenneth A. Debelak

Professor Scott A. Guelcher

Professor Charles M. Lukehart

To my parents, Richard and Susan Berron

ACKNOWLEDGEMENTS

I would like to thank my advisor, Dr. Kane Jennings for his support and encouragement throughout my graduate school career. I found it a joy to learn through research under his guidance. He has always been supportive of my creativity in approaches to problems in our research. It was truly my pleasure to work in his research group at Vanderbilt. I would also like to thank my committee members, Dr. Paul Laibinis, Dr. Scott Guelcher, Dr. Ken Debelak, and Dr. Charles Lukehart who gave me support and direction during my graduate school career. Their thoughtful criticism has helped me to hone my skills as a researcher. I wish them the best in their endeavors.

I would like to thank Miles Barr, Evan Graybill, Andrew Payne, Remington Fischer, Dr. Eric Brantley, and Peter Ciesielski for their contributions to this research, as well as Dr. Dongshun Bai, Dr. Helen Kincaid, Chris Faulkner, Angeline Cione and Brandon Booth for their helpful discussions throughout my time at Vanderbilt. I consider myself luck to have worked with such a group of intelligent and humorous individuals. They have enriched my time in the lab and for that, I am grateful. I also would like to thank Dr. Bob Geil, Nirav Vora, Mekha George, Ben Schmidt, and James Burst for their understanding and willingness to help with characterizations in their lab.

I thank Dr. Bridget Rogers for the use of the ellipsometer and XPS, Dr. Tomlinson Fort for the use of the contact angle goniometer, and Dr. David Cliffel for use of the optical microscope.

I thank all of my friends for the various distractions which have made my time at Vanderbilt much more entertaining. I also appreciate all my family has done for me in

my career. They are always there when I needed a pep talk, and I know I would not be here without them. I thank Dr. Christy Payne for keeping me happy (and well fed). I look forward to being with her in Colorado soon.

This project was supported by the US Department of Energy (ER46239). I thank Dr. Ed Elce (Promerus Electronic Materials) for generously providing the alkylnorbornene monomers. I appreciate Dr. SonBinh T. Nguyen at Northwestern University for helpful discussions on ROMP. I would like to thank the Vanderbilt Institute of Nanoscale Science and Engineering and the Harold Sterling Vanderbilt Fund for fellowships.

TABLE OF CONTENTS

Page

LIST OF TABLES

LIST OF FIGURES

CHAPTER I

INTRODUCTION

With the increasing interest in hydrogen as a viable energy currency,[1] a need to improve current fuel cell efficiencies while driving down equipment costs is essential. Proton exchange membrane (PEM) fuel cells have exceptionally good qualities for power generation. PEM fuel cells can operate at low temperature[2] with high theoretical efficiency[3] and excellent durability.[4] In particular, a redesign of the PEM fuel cell electrode assembly has the greatest potential to increase overall performance with the molecular optimization of proton, electron, and gas transport properties while reducing cost through more efficient use of materials.[5]

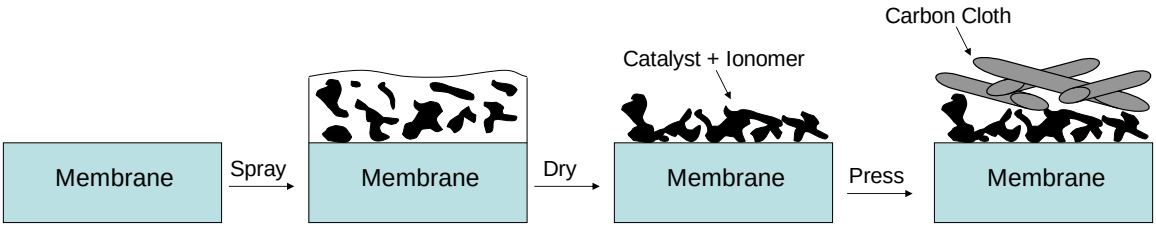

Figure 1.1. Preparation of a typical membrane electrode assembly.

Current fabrication approaches[4,6] for proton exchange membrane (PEM) fuel cells are highly empirical and utilize poorly controlled coating and processing methods. As an example of a common integration of catalyst layers within a fuel cell, a microscopically ill-defined mixture of catalyst and ionomer is sprayed or brushed onto a Nafion® membrane, and the resulting structure is pressed against a carbon cloth (Figure 1.1).[6]

Due to the poor control of this method, a significantly thicker catalyst layer must be prepared to assure complete coating of the membrane, leading to waste of expensive materials.[6] Coupled with the empirical nature of the mixing process, this overly thick catalyst layer will result in poor utilization of catalyst since many catalyst particles are not wired to the electron- or proton-conductive elements and are therefore inactive in the electrode reaction.[7] In addition, the empirical nature of these processes leads to poor reproducibility and the inability to compare results from different laboratories.

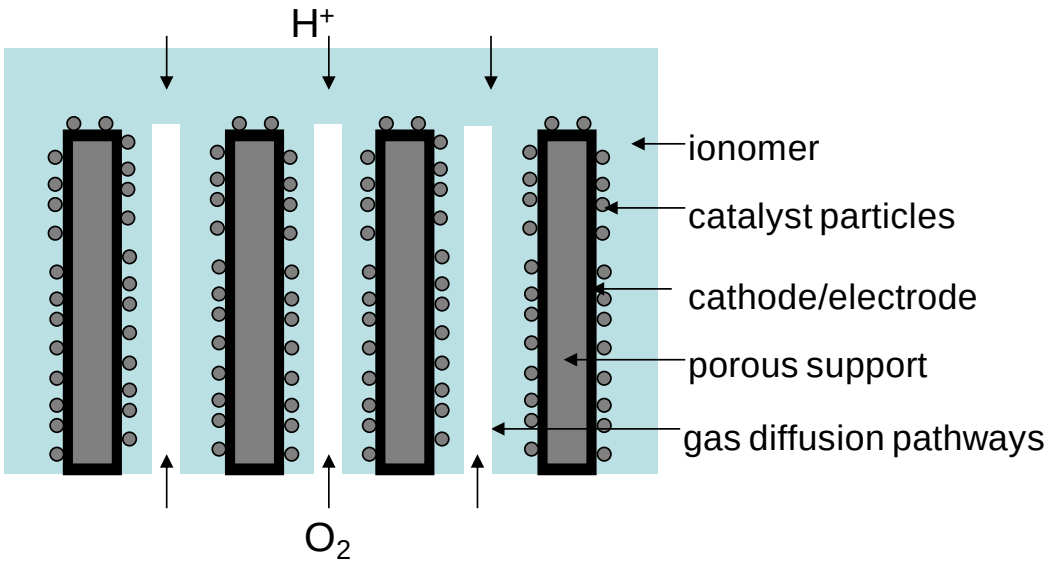

Figure 1.2. Cross sectional view of proposed integrated catalyst/ionomer network.

The research presented herein seeks to radically alter PEM fuel cell processing and integrate the catalyst support, gas diffusion pathways, and ionomer into a single network based on a bottom-up, templated approach. We utilize the similar nanoscale dimensions of the catalyst particles and the pores that transport oxygen and ions to construct a highly controlled, well-defined interface for the triple access by protons, electrons, and gas molecules to the catalyst particles. Figure 1.2 shows a schematic of

the proposed design of an integrated cathode where catalyst nanoparticles are supported on a nanoporous gold structure. These pores effectively double as conduits for gas diffusion. A new class of ionomer film is grown from the pore walls to develop proton conducting pathways throughout the pores and to the adsorbed catalyst particles. This ionomer film can be integrated with a bulk membrane or an anode that is engineered in a similar way. Each catalyst particle will be electronically accessible from the metal cathode and in contact with proton-conducting ionomer to yield extremely high utilization efficiencies of the catalyst (approaching 100%).[5,8] A network based on nanoporous structures enables high catalytic surface areas (> 10,000 cm^2 of active area per cm^2 of geometrical area) and rapid transport of oxygen to the catalyst particles.[5,9,10]

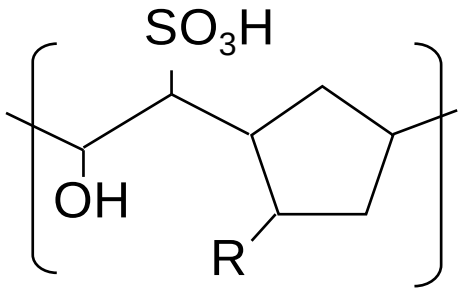

Figure 1.3. New class of ionomer materials to be prepared based on poly(n-alkylnorbornenes). R represents an n-alkyl group.

As an integral part of this project, we will introduce new classes of interfacial ionomers based on a controlled surface-initiated ring-opening metathesis polymerization of hydrocarbon-functionalized norbornenes (see Figure 1.3). The hydrophobicity of the ionomer is tailored to promote self organization of conductive pathways to enhance proton transport.[5,11] The surface-initiated growth of the films should enable uniform

growth throughout the pores and precise tailoring of the catalyst/ionomer interface, which has often been neglected in previous work. This innovative processing will utilize highly controlled methods of thin film fabrication to enable a stronger fundamental understanding of the relevant atomic- and molecular-scale factors required to optimize performance of electrode interfaces.

References

1. Schultz, M. G.; Diehl, T.; Brasseur, G. P.; Zittel, W. *Science* **2003,** 302, (5645), 624-627.

2. Barbir, F., *PEM Fuel Cells: Theory and Practice*. Elsevier Academic Press: Boston, 2001.

3. Appleby, A. J.; Foulkes, F. R., *Fuel Cell Handbook*. Van Nostrand Reinhold: New York, 1989.

4. Carrette, L.; Friedrich, K. A.; Stimming, U. *ChemPhysChem* **2000,** 1, 162-193.

5. Middelman, E. *Fuel Cells Bulletin* **2002**, (11), 9-12.

6. Litster, S.; McLean, G. *Journal of Power Sources* **2004,** 130, (1-2), 61-76.

7. Cha, S. Y.; Lee, W. M. *J. Electrochem. Soc.* **1999,** 146, 4055-4060.

8. Brankovic, S. R.; Wang, J. X.; Adzic, R. R. *Surface Science* **2001,** 474, (1-3), L173-L179.

9. Martin, C. R. *Chem. Mater*. **1996,** 8, 1739-1746.

10. Che, G.; Lakshmi, B. B.; Fisher, E. R.; Martin, C. R. *Nature* **1998,** 393, 346-349.

11. Saito, M.; Arimura, N.; Hayamizu, K.; Okada, T. *J. Phys. Chem. B* **2004,** 108, 16064-16070.

CHAPTER II

BACKGROUND

Fuel Cells

Proton exchange membrane fuel cells operate on the reaction of hydrogen and oxygen yielding water (Figure 2.1). Hydrogen is introduced at the anode side, where it is oxidized within the catalyst layer to form protons and electrons. The membrane consists of an ionomer designed to transport protons from the anode to the cathode while not allowing the mixing of the feed gasses. The protons combine with electrons and oxygen in the catalyst layer of the cathode to form water. For high efficiency in the anodic or cathodic half reactions, the catalyst must be wired to the proton conducting ionomer and the electron conducting gas diffusion matrix and be easily accessible to the appropriate feed gas.

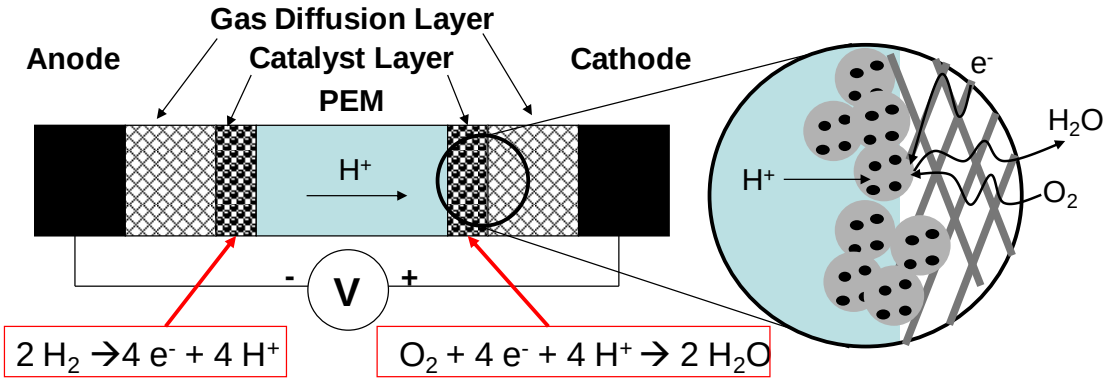

Figure 2.1. Schematic of a PEM fuel cell, and a zoomed in view of the key interfacial issues.

While we focus on proton exchange membrane fuel cells, many different types of fuel cells are currently being researched. Direct methanol fuel cells offer an alternative form of energy conversion in which methanol oxidized at the anode to CO_2 and oxygen is reduced at the cathode to produce water. Direct methanol fuel cells are attractive due to their low operating temperatures and the multiple renewable sources of methanol fuel.[1] Direct methanol fuel cells often use the same ionomers as PEM fuel cells, and also may benefit from technologies developed in this research.[2]

Membranes

Perfluorosulfonate polymers such as Nafion® have been predominately used as fuel cell membranes due to their chemical, mechanical, and thermal stability and high proton conductivity. The superior proton transport through these membranes is likely due to their high acidity and self organization of the hydrophilic sulfonate groups to form continuous regions of aqueous and ionic ribbon-like clusters that serve as proton wiring amidst a hydrophobic $-(CF_2)_n-$ matrix (Figure 2.2).[3,4] The effective concentration of sulfonate groups within this cluster region ranges from 1 – 10 mol/L.[5] Protons are believed to "hop" along sulfonate groups whereas larger cations (Li^+ and Na^+) are transferred by a water-facilitated vehicle mechanism.[4] Molecular dynamics simulations of Nafion and Dow membrane indicate the need for good connectivity of these ionic regions.[5] The shorter side chain length of the Dow ionomer is believed to provide less of a disturbance of cluster generation and increase the number of transport paths for ions and water; this may explain the higher ion conductivities for the Dow membrane.[5] The results of these simulations led the authors to conclude that membranes with higher

conductivity are possible if polymer structure is carefully controlled. While perfluorosulfonate ionomers have performed generally well, there has been concern over their expense, low resistance to gas transport, low temperature range of operation, and high osmotic drag, which complicates water management.[6]

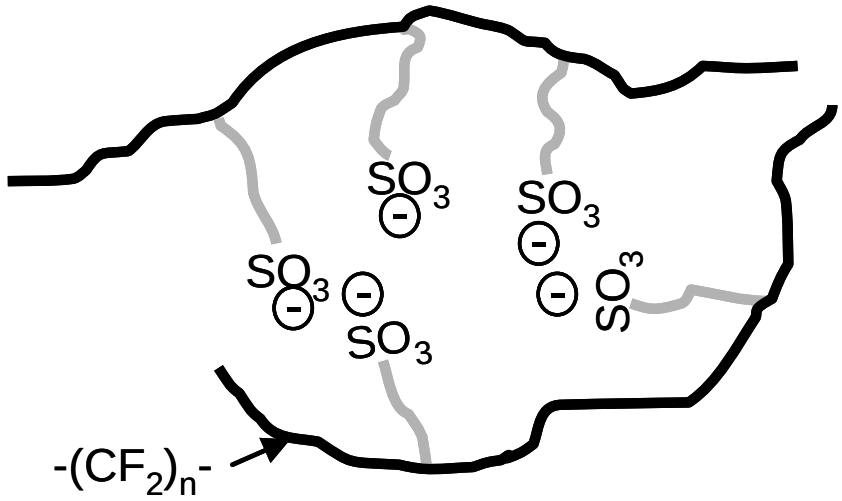

Figure 2.2. Self-organization within Nafion® to form ionic clusters. The gray lines represent fluorinated ether segments that connect sulfonates to the hydrophobic backbone.

Roziere and Jones[6] have reviewed the use of non-fluorinated polymers for PEM fuel cells. These materials typically consist of sulfonated heterocyclic- or aromatic-based polymers that have sufficient thermal stability for fuel cell operation at temperatures exceeding 80 °C. Problems with these materials have included low solubility, irreproducible sulfonation, poor stability once sulfonated, and/or poor conductivity at low water swelling. The poor stability was especially pronounced for polyaromatics in which sulfonates were attached directly on the aromatic ring.[6] The poor conductivity for many of these materials may be due to their ultra rigidity that prevents the polymer from self-organizing and forming ion-conducting pathways. New classes of non-fluorinated, non-

aromatic polymers that are structured to promote self-organization while still maintaining good stability should provide improved performance.

The ionomer materials introduced in this thesis are comprised of a family of sulfonated polynorbornenes as shown in Figure 1.3, and are designed to promote proton transfer near electrode/catalyst interfaces. In general, polynorbornenes exhibit excellent thermal and chemical stability,[7] and the asymmetry of the structure proposed here, considering the hydrophobicity of *R*, should promote self-organization to promote formation of a hydrophobic matrix for good gas transport along with SO_3^- lined channels for proton transport. A notable advantage of these polynorbornenes is that they can be grown from surfaces at low temperature using a controlled ring-opening metathesis polymerization (ROMP) to produce well-defined thin films on surfaces of any geometry.[8] The highly controlled and gentle surface chemistry combined with the stability of polynorbornenes creates unique opportunities to study and optimize proton transfer at ionomer/catalyst interfaces.

Surface-Initiated Polymerizations

Prior work in fuel cells has focused on bulk, casted polymers as membranes.[1,2] While these thick polymers are useful under operating conditions to prevent gas cross-over, their wide-spread use has masked important interfacial events. Thinner films, especially surface-initiated films, allow for a better defined and more assured integration of catalyst and ionomer. Surface-initiated polymerizations refer to the continual addition of repeat units at the termini of surface-tethered chains and offer several advantages over traditional coating methods, including rapid processing,[9] improved adhesion due to a

chemical coupling of the initiator/polymer chain to the substrate, the ability to prepare uniform, conformal coatings on objects of any shape,[10,11] excellent control over film thickness,[12] from a few nanometers up to the micron level,[9] tunable grafting densities,[13] and good control over depth-dependent composition by enabling the growth of additional blocks to prepare copolymer films.[14-16] These films are already used in applications traditionally dominated by spin coating and solution casting, such as polymer dielectric layers,[9] etch resists for lithography,[17,18] responsive polymer films,[19,20] and membrane separations.[21,22] The ability to grow films with new compositions, architectures, and properties could have a profound impact on the development of new fuel cell ionomers.

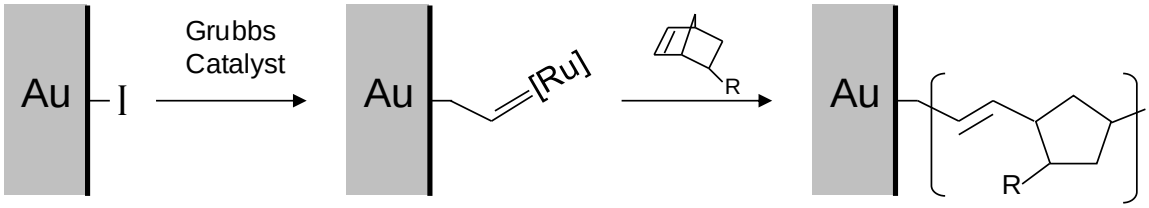

Figure 2.3. Schematic representation of surface initiated polynorbornene film growth.

Ring-opening metathesis (ROMP) polymerizations exhibit rapid kinetics under mild conditions, producing among the thickest surface-initiated films (Figure 2.3) ever produced (> 1 μm).[8,9,12,23,24] The predominate ROMP monomer studied in surface-initiated cases has been norbornene and its functional derivatives. Polymerization of unfunctionalized norbornene yields primarily hydrophobic films with low dielectric constants. Functional derivatives of norbornene can polymerize to produce films with wide ranging properties and applications, including functionalization of chromatographic supports[8,11,25,26] to improve selectivity, and modification of carbon nanotubes to improve dispersability in common solvents.[10] Surface initiated ROMP on gold occurs by

anchoring an olefinic initiator group to the surface via thiolate/Au linkage. The olefin functionality in the covalently bound monolayer is exposed to a metathesis catalyst (Grubbs Catalyst) to generate active sites bound to the surface. Non-bound catalyst is rinsed away, and the surface is exposed to a ROMP active monomer. The reactivity of a ROMP monomer is typically related to the ring strain of the monomer. The high ring strain of the norbornene family tends to result in highly reactive monomers. Typical surface initiated ROMP experiments are run for short time periods (5 - 60 min). Since the most preferred thermodynamic conditions for ROMP are at low temperatures,[27] most experiments are run at room temperature.[8,23,28-31] Chain terminating reactions include reaction of the active site with olefin functionality in the pNB backbone (inter- or intra-molecular) and in vinyl terminated initiators, the ring closing reaction with neighboring uncatalyzed vinyl groups.

Alternate Architectures

The common architecture for PEM fuel cells leads to a poorly defined three-phase boundary and low utilization of expensive materials (Figure 1.1). Geoffrey Ballard, co-founder of Ballard Power Systems, was recently quoted in *Popular Science* as stating that there needs to be a "fundamental engineering rethink" of the architecture and geometry of PEM fuel cells.[32] In recent years, there have been numerous approaches at alternative electrode architectures. While many focused solely on shrinking the electrode dimensions,[33] some recognized the opportunity for increased efficiency with the orientation of the electrode microstructure. Middelman used a strong electric field to orient the electron conductor, pores and the bulk polymer normal to the membrane

surface, though no results were published detailing any improvements in performance over conventional electrodes.[3]

DeSimone and co-workers have prepared cross-linked, highly fluorinated PEMs that exhibit textured surfaces via soft lithography.[34] Membrane electrode assemblies containing these textured membranes exhibited up to 1.61 times more power than flat membranes, illustrating the importance of interfacial area in these systems. They achieved Pt loadings as low as 0.09 mg/cm^2.

Creager and co-workers have discussed the need for intimate contact between the electrode and ionomer and have bound an ionomer monolayer to a carbon electrode by reduction of a fluorosulfonimide aryl diazonium zwitterion.[35] The bound monolayers are highly stable to solvents and temperature but are very thin (~1 nm), thus providing low interfacial volume for pulling protons from the bulk ionomer into the interfacial region.

Martin and co-workers provided a foundation for an alternate design in 1998 when they deposited graphitic carbon inside the walls of a porous alumina support to produce free-standing carbon membranes in which the inner and outer tubules were electrochemically active.[36] They demonstrated that Pt and Pt/Ru nanoparticles could be deposited within the tubules and were highly active for oxygen reduction and methanol oxidation, yielding currents 20 times higher than those at a flat Pt-coated electrode of similar geometric area. Consistent with typical post polymerization ionomer deposition methods, the Nafion ionomer coated the top of the membrane and was not integrated within the pores. The authors have not followed up this promising work, but the initial findings offer potential for the design of a well-defined interface in which catalyst, ionomer, and gas diffusion are integrated into one network. Such a templated system

may provide a highly reproducible test bed for examining basic issues in how interfacial effects and molecular design influence fuel cell performance.

In general, alumina films containing a homogeneous array of monodisperse pores with diameters varying between 5 and 250 nm can be prepared by the anodization of aluminum.[37] The pore size can be tuned by controlling the pH, anodization voltage, and choice of acid in the anodizing media. Martin's group[38] has used the pores of alumina membranes as templates to synthesize a wide variety of materials including tubules and fibrils composed of metals, polymers, and semiconductors. Others have adopted Martin's strategy to form ordered metal nanohole[39] or colloidal[40] arrays or membranes with self-assembled monolayers lining the pore walls.

Researchers at Johns Hopkins have developed simple techniques for the generation of nanoporous gold films that can function as electrodes of high surface area (Figure 2.4).[41,42] The process for their nanoporous gold is based on the etching of alloys of gold and silver with nitric acid. As gold is inert to nitric acid, the acid selectively etches the silver from the alloy.[43] The remaining gold tends to cluster into islands and allows the dissolution front to move further into the material, leaving behind nanoporous gold structures.[44,45] This process occurs rapidly (< 5 min) for thin sheets of the alloy, known as white gold leaf. The pores of the nanoporous gold structure are tunable through additional annealing time, which allows the gold structure to coarsen and lowers the specific surface area while increasing ligament and pore size.[41] The proposed work seeks to integrate ionomer, catalyst, and gas diffusion into one network to achieve improved performance in PEM fuel cells.

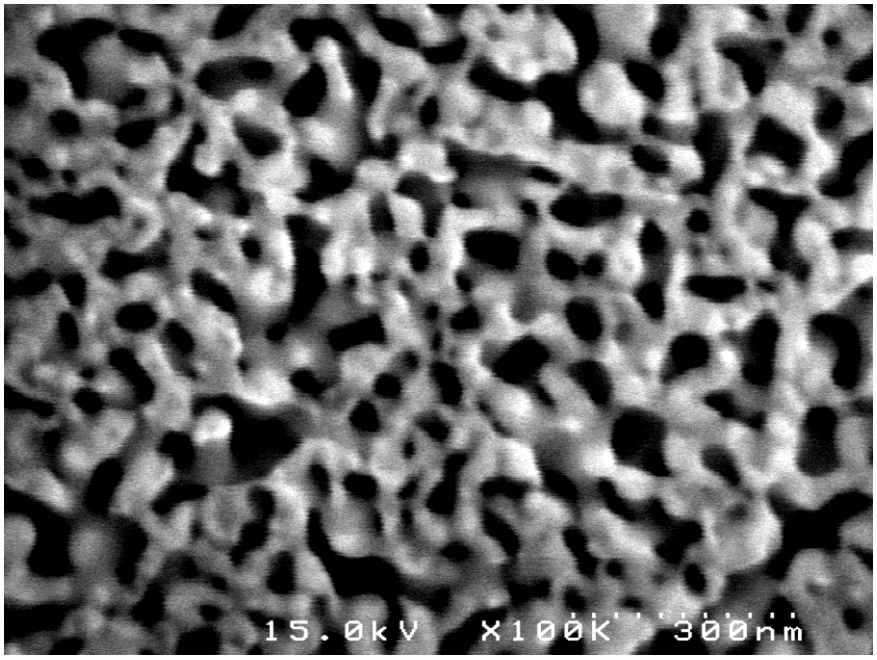

Figure 2.4. Scanning electron microscope image of nanoporous gold leaf after 30 min dealloying in concentrated nitric acid. Image courtesy of Peter Ciesielski.

References

1. Carrette, L.; Friedrich, K. A.; Stimming, U. *ChemPhysChem* **2000,** 1, 162-193.

2. Shao, Z. G.; Lin, W. F.; Zhu, F. Y.; Christensen, P. A.; Li, M. Q.; Zhang, H. M. *Electrochemistry Communications* **2006,** 8, (1), 5-8.

3. Middelman, E. *Fuel Cells Bulletin* **2002**, (11), 9-12.

4. Saito, M.; Arimura, N.; Hayamizu, K.; Okada, T. *J. Phys. Chem. B* **2004,** 108, 16064-16070.

5. Jinnouchi, R.; Okazaki, K. *J. Electrochemical Soc.* **2003,** 150, E66-E73.

6. Roziere, J.; Jones, D. J. *Annu. Rev. Mater. Res.* **2003,** 33, 503-555.

7. Muhlebach, A.; Schaaf, P. A. v. d.; Hafner, A.; Setiabudi, F. *J. Molecular Catalysis-A-Chemical* **1998,** 132, 181-188.

8. Buchmeiser, M. R.; Sinner, F.; Mupa, M.; Wurst, K. *Macromolecules* **2000,** 33, (1), 32-39.

9. Rutenberg, I. M.; Scherman, O. A.; Grubbs, R. H.; Jiang, W.; Garfunkel, E.; Bao, Z. *J. Am. Chem. Soc.* **2004,** 126, 4062-4063.

10. Jennings, G. K.; Brantley, E. L. *Adv. Mater.* **2004,** 16, 1983-1994.

11. Buchmeiser, M. R., Metathesis polymerization to and from surfaces. In *Surface-Initiated Polymerization I*, 2006; Vol. 197, pp 137-171.

12. Kim, N. Y.; Jeon, N. L.; Choi, I. S.; Takami, S.; Harada, Y.; Finnie, K. R.; Girolami, G. S.; Nuzzo, R. G.; Whitesides, G. M.; Laibinis, P. E. *Macromolecules* **2000,** 33, 2793-2795.

13. Jordi, M. A.; Seery, T. A. P. *J. Am. Chem. Soc.* **2005,** 127, (12), 4416-4422.

14. Matyjaszewski, K.; Miller, P. J.; Shukla, N.; Immaraporn, B.; Gelman, A.; Luokala, B. B.; Siclovan, T. M.; Kickelbick, G.; Vallant, T.; Hoffmann, H.; Pakula, T. *Macromolecules* **1999,** 32, (26), 8716-8724.

15. Boyes, S. G.; Brittain, W. J.; Weng, X.; Cheng, S. Z. D. *Macromolecules* **2002,** 35, 4960-4967.

16. Kim, J.-B.; Huang, W.; Bruening, M. L.; Baker, G. L. *Macromolecules* **2002,** 35, 5410-5416.

17. Zhou, F.; Liu, W. M.; Hao, J. C.; Xu, T.; Chen, M.; Xue, Q. J. *Advanced Functional Materials* **2003,** 13, (12), 938-942.

18. Husemann, M.; Mecerreyes, D.; Hawker, C. J.; Hedrick, J. L.; Shah, R.; Abbott, N. L. *Angewandte Chemie-International Edition* **1999,** 38, (5), 647-649.

19. Bai, D. S.; Habersberger, B. M.; Jennings, G. K. *J. Am. Chem. Soc.* **2005,** 127, (47), 16486-16493.

20. Ayres, N.; Boyes, S. G.; Brittain, W. J. *Langmuir* **2007,** 23, (1), 182-189.

21. Balachandra, A. M.; Baker, G. L.; Bruening, M. L. *Journal of Membrane Science* **2003,** 227, (1-2), 1-14.

22. Bai, D. S.; Elliott, S. M.; Jennings, G. K. *Chemistry of Materials* **2006,** 18, (22), 5167-5169.

23. Weck, M.; Jackiw, J. J.; Rossi, R. R.; Weiss, P. S.; Grubbs, R. H. *J. Am. Chem. Soc.* **1999,** 121, 4088-4089.

24. Liu, X. G.; Guo, S. W.; Mirkin, C. A. *Angew. Chem. Int. Ed.* **2003,** 42, (39), 4785-4789.

25. Buchmeiser, M. R. *Macromolecular Rapid Communications* **2001,** 22, (14), 1082-1094.

26. Mayr, B.; Buchmeiser, M. R. *Journal of Chromatography A* **2001,** 907, (1-2), 73-80.

27. Ivin, K. J.; Mol, J. C., *Olefin Metathesis and Metathesis Polymerization*. Academic Press: San Diego, 1997.

28. Nguyen, S. T.; Johnson, L. K.; Grubbs, R. H.; Ziller, J. W. *Journal of the American Chemical Society* **1992,** 114, (10), 3974-3975.

29. Lynn, D. M.; Kanaoka, S.; Grubbs, R. H. *Journal of the American Chemical Society* **1996,** 118, (4), 784-790.

30. Juang, A.; Scherman, O. A.; Grubbs, R. H.; Lewis, N. S. *Langmuir* **2001,** 17, (5), 1321-1323.

31. Seehof, N.; Grutke, S.; Risse, W. *Macromolecules* **1993,** 26, (4), 695-700.

32. Behar, M. *Popular Science* **2005,** 266, (Jan. 2), 64-68.

33. Lux, K. W.; Rodriguez, K. J. *Nano Letters* **2006,** 6, (2), 288-295.

34. Zhou, Z.; Dominey, R. N.; Rolland, J. P.; Maynor, B. W.; Pandya, A. A.; DeSimone, J. M. *J. Am. Chem. Soc.* **2006,** 128, 12963-12972.

35. Creager, S. E.; Liu, B.; Mei, H.; DesMarteau, D. *Langmuir* **2006,** 22, 10747-10753.

36. Che, G.; Lakshmi, B. B.; Fisher, E. R.; Martin, C. R. *Nature* **1998,** 393, 346-349.

37. Li, F.; Zhang, L.; Metzger, R. M. *Chem. Mater.* **1998,** 10, 2470-2480.

38. Martin, C. R. *Chem. Mater.* **1996,** 8, 1739-1746.

39. Masuda, H.; Fukuda, K. *Science* **1995,** 268, 1466-1468.

40. Hanaoka, T.-A.; Heilmann, A.; Kroll, M.; Kormann, H.-P.; Sawitowski, T.; Schmid, G.; Jutzi, P.; Klipp, A.; Kreibig, U.; Neuendorf, R. *Appl. Organometallic Chem.* **1998,** 12, 367-373.

41. Ding, Y.; Kim, Y. J.; Erlebacher, J. *Advanced Materials* **2004,** 16, (21), 1897-+.

42. Zeis, R.; Mathur, A.; Fritz, G.; Lee, J.; Erlebacher, J. *Journal of Power Sources* **2007,** 165, (1), 65-72.

43. Mathur, A.; Erlebacher, J. *Applied Physics Letters* **2007,** 90, (6).

44. Erlebacher, J.; Aziz, M. J.; Karma, A.; Dimitrov, N.; Sieradzki, K. *Nature* **2001,** 410, (6827), 450-453.

45. Erlebacher, J. *Journal of the Electrochemical Society* **2004,** 151, (10), C614-C626.

CHAPTER III

EXPERIMENTAL PROCEDURES AND CHARACTERIZATION METHODS

Experimental Procedures

Materials

5-n-butylnorbornene (98%), 5-n-hexylnorbornene (98%), and 5-n-decylnorbornene (98%) monomers were provided by Promerus Electronic Materials and used as received. Grubbs Catalyst - first generation (benzylidene-bis(tricyclohexylphosphine)dichlororuthenium), 4-mercapto-1-butanol (97%), 1-pentanethiol (98%), 1-dodecanethiol (98%), 2-propene-1-thiol (allyl mercaptan, 70%), hexane-1,6-dithiol (97%), copper (II) sulfate (99%), 11-Mercapto-1-undecanol (97%), KHCO3 (98%), Br_2 (99%), KOH (85%), $K_3Fe(CN)_6$ (99%), and $K_4Fe(CN)_6 \cdot 3H_2O$ (99%) were used as received from Sigma-Aldrich. Norbornene (NB, 99%) was used as received from MP Biomedicals. Gold leaf (Monarch 12 Kt) was used as received from fineartstore.com. Dichloromethane (99.9%), potassium tetrachloroplatinate (II) (46.5-47% Pt), trans-3,6-endo-methylene-1,2,3,6-tetrahydrophthaloyl chloride (97%), acetic anhydride (99%), dimethyl sulfoxide (99%), sodium sulfate (anhydrous), perfluorooctanoyl chloride (C7F15COCl, 98%), nitric acid (69.6%) and toluene (99.9%) were used as received from Fisher Scientific. Sulfuric acid (95%) was used as received from EM Science. Hexane (99.9%) and tetrahydrofuran (THF, 99.9%) were used as received from Burdlick & Jackson. n-Docosanethiol was used as received from Narchem

Corporation. Gold shot (99.99%) and chromium-coated tungsten filaments were obtained J&J Materials and R.D. Mathis, respectively. Silicon wafers (100) were obtained from Montco Silicon. Ethanol (absolute) was used as received from AAPER. Deionized water (16.7 MΩ·cm) was purified with a Modu-Pure system.

Preparation of Gold Substrates

Silicon wafers were rinsed with ethanol and water, then dried in a nitrogen stream. Chromium (100 Å) and gold (1250 Å) were sequentially evaporated onto the silicon wafers at rates of < 2 Å s-1 in a diffusion-pumped chamber with a base pressure of 4 x 10-6 torr. The wafers were typically cut into sample sizes of 1.5 cm x 3.5 cm.

Characterization Methods

Reflectance Absorption Infrared Spectroscopy (RAIRS)

Reflectance absorption infrared spectroscopy is used to determine structural and compositional information about thin organic films. The functional groups that compose the film absorb IR radiation (400-4000cm^{-1}) in specific regions of the spectrum due to specific vibrations (bending, stretching, etc.) of the molecules, allowing the identification of species present in the film. RAIRS is a specific type of IR spectroscopy which can aid in the determination of film structure. The peak intensity for a given mode from RAIRS is proportional to the square of the component of its dynamic dipole moment normal to the surface, as indicated by the following equation:[1]

$$I \propto cos^2 \theta_{mz} \quad (3\text{-}1)$$

where I represents the spectral intensity and θ_{mz} is the average angle between the transition dipole moment (m) for a particular band and the surface normal (z). This orientational dependence is due to the polarization of the incoming beam parallel to the substrate, causing an electric field normal to the substrate. [2] Thus, a functional group with a dipole oriented mostly normal to the substrate ($\theta_{mz} \rightarrow 0°$) will have a much higher spectral intensity than a functional group oriented mostly parallel to the substrate ($\theta_{mz} \rightarrow 90°$).

The CH stretching region of the RAIR spectrum for pNB consists of crisp and intense asymmetric and symmetric CH_2 (2948 cm^{-1} and 2866 cm^{-1}) and CH stretching (2911 cm^{-1}) peaks. The position of the CH_2 scissoring peak (~1450 cm^{-1}) is indicative of purely cyclic CH_2 functionality.[3] The Davydov splitting of the scissoring peak into a doublet observed in the pNB spectrum is unique to largely homogeneous, well ordered chain structures.[4] The olefin functionality is observed in the trans C=CH out of plane bending[3,5] peak (968 cm^{-1}), cis C=CH out of plane bending peak[3,5] (745 cm^{-1}), C=C stretching peak[3,5] (1661 cm^{-1}), and the C=CH stretching peak[5,6] (3030 cm^{-1}). The introduction of sulfonate functionality can be observed through the appearance of asymmetric and symmetric SO_3 stretching (~1343, 1203, ~1167, and 1040 cm^{-1}) modes.[3,5,7]

RAIRS was performed using a Varian 3100 FT-IR spectrometer in single reflection mode with a universal sampling accessory and a liquid nitrogen cooled, narrow-band MCT detector. p-Polarized light was incident at 80° from the surface

normal. Spectra were collected using 200 scans at a resolution of 2 cm^{-1} using a clean gold sample as a reference.

Electrochemical Impedance Spectroscopy (EIS)

Barrier properties of films may be measured with electrochemical impedance spectroscopy. In EIS, the film-coated electrode is part of an electrochemical cell with a solution containing redox probes and ions and connected to an alternating current source. During an EIS experiment, current is measured upon altering the potential of the working electrode with a sinusoidal perturbation of varying frequency. The following equation is then applicable to this situation:

$$Z = \frac{E(t)}{I(t)} = \frac{E_0 \cos(\omega t)}{I_0 \cos(\omega t - \phi)} = Z_0 \frac{\cos(\omega t)}{\cos(\omega t - \phi)} \tag{3-2}$$

where Z is the impedance in the system, $E(t)$ is the applied potential at time t, $I(t)$ is the resulting current at time t, E_0 is the amplitude of the potential, ω is the radial frequency (equals $2\pi f$ where f is the frequency in Hz), I_0 is the amplitude of the current, ϕ is the phase shift of the output signal, and Z_0 is the magnitude of the impedance. From these equations, the impedance of a system can be characterized by a magnitude and a phase shift. An impedance plot is obtained by measuring cell current while altering the frequency of the ac source. The impedance changes due to the ability of redox probes to reach the vicinity of the working electrode/metal surface underlying the film where they can be oxidized/reduced. Impedance is directly affected by the transport of ions through a film, and lower frequencies allow more time for diffusive processes to occur.[8] Since an

electrochemical cell is used, the results can be modeled using equivalent electrical circuits consisting of resistors and capacitors that represent film, interfacial, and solution properties. Resistance and capacitance values for the initiator and polymer layers in our films may be estimated using the following equations that apply to the equivalent circuits[9] shown in Figure 3.1.

$$|Z| = \sqrt{(Z_{real})^2 + (Z_{imag})^2} \tag{3-3}$$

$$Z_{real} = R \tag{3-4}$$

$$Z_{imag} = \frac{1}{j\omega C} \tag{3-5}$$

where $|Z|$ equals Z_0 and is the magnitude of the total impedance, Z_{real} and Z_{imag} are the real (resistances) and imaginary (capacitances) components of the impedance, R denotes a resistance, and C denotes a capacitance. As evidenced by the impedance equations for a resistor and capacitor, higher film resistance and lower film capacitance yield higher total impedance. Higher impedance corresponds with the inhibition of ion transport to the surface and signifies a better barrier film.[10]

EIS was performed with a Gamry Instruments CMS300 impedance system interfaced to a personal computer. A flat cell (EG&G) was used to selectively expose 1.0 cm^2 of each sample as the working electrode to an aqueous analyte solution. Measurements were taken using a Ag/AgCl/saturated KCl reference electrode with evaporated gold on silicon as the counter electrode. Data were collected between 10^{-1}

and 10^4 Hz and fit using to an appropriate equivalent circuit to determine resistance and capacitance values. Reported values and errors represent the averages and standard deviations, respectively.

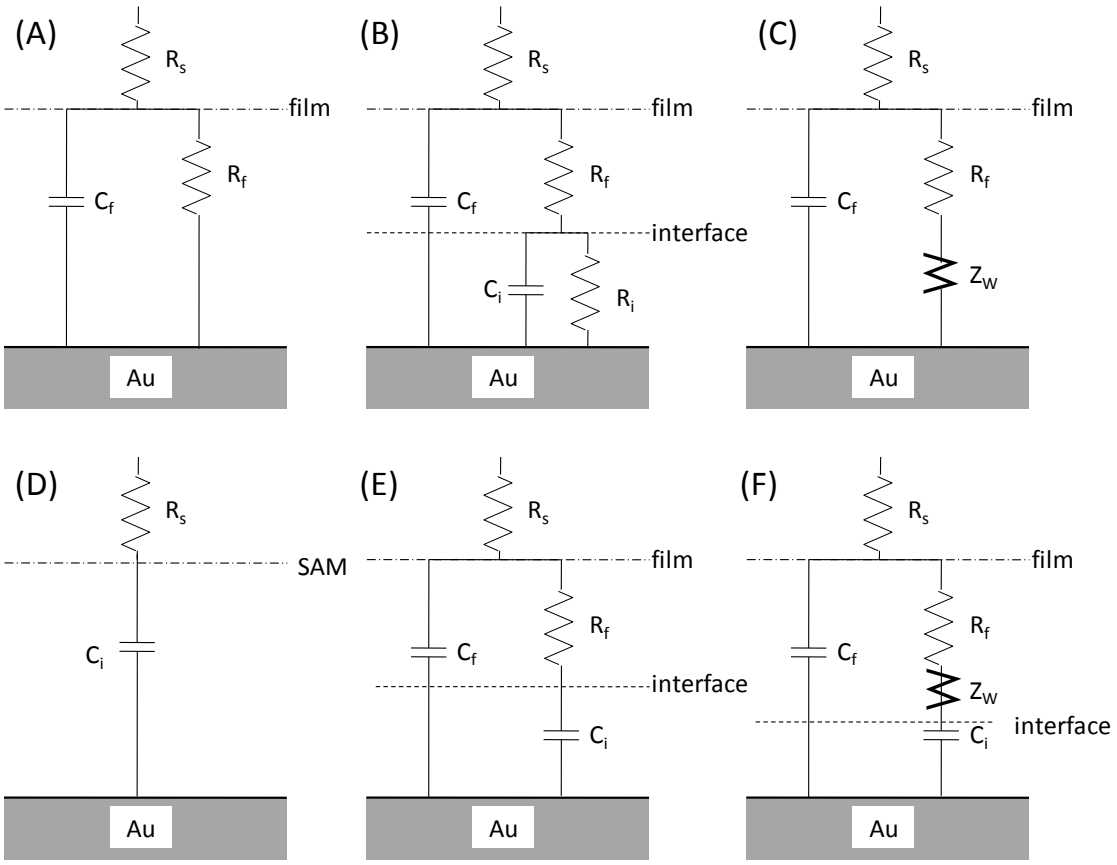

Figure 3.1. Equivalent circuit used to model impedance spectra for films on gold: (A) the commonly used Randles circuit model; (B) the model used for polymer films with two time constant functionality; (C) the Randles circuit model modified with a Warberg impedance; (D) the Randles circuit model in the absence of redox probes; (E) the two time constant model in the absence of redox probes; (F) the two time constant model in the absence of redox probes with mass transfer limitations.[9]

Cyclic Voltammetry (CV)

Cyclic voltammetry is the dynamic measurement of current at the working electrode as a result of a linearly-sweeping potential in a standard three electrode

electrochemical cell. The potential is applied and is varied at a constant rate to a predefined potential limit, at which the direction of the scan is reversed and the potential is scanned in the opposite direction.[8,11] In a redox experiment, species deposited via reduction on the forward scan are reduced on the reverse scan.

CV was performed with a Gamry Instruments CMS300 impedance system interfaced to a personal computer. A flat cell (EG&G) was used to selectively expose 1.0 cm^2 of each sample as the working electrode to an aqueous analyte solution. Reported values and errors represent the averages and standard deviations, respectively obtained from at least 3 different experiments. Details of the specific CVs used for the oxygen reduction reaction and copper deposition are given in Chapter VI.

Underpotential Deposition (UPD)

Underpotential deposition is a plating technique where the deposition of a metal adlayer onto a metal substrate occurs at potentials more positive than the equilibrium potential of the given species. This equilibrium potential (E_{eq}) is governed by the Nernst Equation:

$$E_{eq} = E^o + \frac{RT}{nF} ln\left(\frac{a^{reduced}}{a^{oxidized}}\right) \quad (3\text{-}6)$$

where E^o is the standard potential, R is the gas constant, T is the temperature, n is the number of electrons transferred, a is the chemical activity, and F is the Faraday constant.[12] UPD allows the deposition of submonolayer coverages of a less noble onto a more noble substrate. UPD is typically accomplished in a CV experiment, where

deposition of the adlayer is observed as cathodic current and removal of the adlayer is observed as anodic current. The potential is held at a value corresponding to the desired adlayer coverage, and the working electrode is removed under constant potential. We utilize UPD to deposit a submonolayer of copper (less noble adlayer) onto polycrystalline gold (more noble) substrates. Potentials are cycled between 500 and 50 mV vs. $Cu^{0/1+}$ in a solution of 1.0 mM $CuSO_4$ in 0.1 M H_2SO_4 (aq, nitrogen saturated). On polycrystalline gold, only one copper UPD peak (~200 mV) can typically be distinguished from the deposition of bulk copper.[13] Underpotential deposition of copper was performed with a Gamry Instruments CMS300 impedance system interfaced to a personal computer. After at least two cycles, the potential was held just negative of the UPD peak on the cathodic sweep(~100 mV), and the sample was removed from solution under potential control. Samples were rinsed in ethanol and dried in a nitrogen stream.

Ellipsometry

The use of ellipsometry allows simple estimation of film thickness at the angstrom scale. Light is polarized linearly and reflected off the substrate. The reflection of the light causes an elliptical polarization where the detector collects phase (Δ) and amplitude (Ψ) information. Thin film models are used to fit the data to theoretical phase and amplitude response. The proposed polymer films are fit to a generic two-term Cauchy layer model. Since both the film refractive index, n, and thickness are usually not known, this model allows both of these physical film parameters to be determined by fitting experimental data to the model and minimizing the mean square error between the

two.[14] Data are collected at one angle (75°) and over an extensive wavelength range (usually 400 – 700 nm) to ensure more accurate fits of the data to theoretical models.

Contact Angle Goniometry

Contact angle goniometry is a simple and convenient method of evaluating the surface properties of thin films.[15] When a small drop of liquid is placed onto a surface, the interfacial tensions between the drop, the film surface, and air determine the shape of the drop. The interfacial tensions are denoted as γ_{SV} at the solid-vapor interface, γ_{SL} at the solid-liquid interface, and γ_{LV} at the liquid-vapor interface. A force balance of these tensions involved in the surface-liquid-air interface leads to Young's equation:

$$\gamma_{SV} - \gamma_{SL} = \gamma_{LV} \cos \theta \qquad (3\text{–}7)$$

where the contact angle, θ, is the angle between the line drawn tangent to the edge of the liquid drop (at the liquid-vapor interface) and the line flush with the surface underneath the drop (the solid-liquid interface). For a given liquid, typically water or hexadecane, γ_{LV} is held constant while all other values change depending on surface composition. A goniometer, an optical microscope with a protractor built into the lens, is used to determine θ. Water contact angles are used to indicate the relative hydrophilicity/hydrophobicity of a surface, while hexadecane is used for oleophilicity / oleophobicity. Larger measured angles result from more hydrophobic and oleophobic surfaces.

Contact angles are useful in providing insight into surface roughness, chemical composition, and interfacial structure. By adding small liquid drops (~5μL) to the surface using a microliter syringe, the advancing contact angle θ_A and receding contact angle θ_R are generally measured. θ_A is measured after liquid has been added to the drop, causing it to slowly advance across the surface, and θ_R is measured after liquid has been removed from the drop, causing it to slowly recede across the surface. The chemical composition at the surface also greatly affects the measured contact angles. Depending on whether a surface is dominated by $-CH_2-$, $-CH_3$, $-CF_2-$, $-CF_3$, or higher energy ($-SO_3^-$, -OH) groups, the contact angles will be altered.[16] The contact angle hysteresis, $\theta_A - \theta_R$, gives a measure of the roughness or chemical heterogeneity of the surface. More homogeneous surfaces have a very low hysteresis while heterogeneous surfaces have a much larger hysteresis.[17]

Atomic Force Microscopy (AFM)

Atomic force microscopy consists of a small cantilever with a nanometer scale tip which is brought into contact with the surface being examined. The deflection of the cantilever by the surface is monitored by the position of laser light reflected off the cantilever.[18,19] Tapping mode (intermittent contact mode or dynamic contact mode) AFM refers to the oscillation of the cantilever and detecting changes in the phase or amplitude of the oscillations to provide information on the surface. Tapping mode allows the tip to approach the surface to allow the detection of short range forces while preventing the tip from sticking to the surface and is useful for soft materials.[19]

We used a Digital Instruments MultiMode Nanoscope IIIa AFM to investigate surface morphology and uniformity of surface-initiated polymer films. Height contrast images (25 μm x 25 μm) were collected in tapping mode with a silicon tip.

Optical Microscopy

Optical microscopy is a simple and straightforward method to observe microscopic structures.[18] Film coverage and surface morphology were investigated with an Olympus BX41 microscope with Pixera camera and Pixera Viewfinder Pro imaging software. We used a 10x magnification lens to produce 250 μm x 250 μm images.

X-ray Photoelectron Spectroscopy (XPS)

X-ray photoelectron spectroscopy is an ultra high vacuum technique where a material is irradiated with x-rays while the kinetic energy and number of escaping electrons are measured. The kinetic energy can be used to determine the composition, chemical state, and electronic state of the outermost ~10 nm of a material.[20] Data are typically reported as counts per second against binding energy. Binding energy (E_B) is related to the kinetic energy (E_K) by equation 3-8, where hv is the energy of the incident photons and Φ is the work function of the spectrometer.[20]

$$E_K = hv - E_B - \Phi \qquad (3\text{-}8)$$

XPS was used to monitor the deposition of copper and platinum onto planar gold substrates. We used a Leybold-Heraeus LHS-10 surface analysis system equipped with a

non-monochromatic dual Mg/Al anode x-ray source. The analysis chamber pressure was ~2e-9 torr. Data on were collected over binding energies from 950 to 920 eV and 100 to 60 eV using the Mg Kα anode (E_{photon} = 1253 eV). Spectra were averaged over 10 scans at a constant pass energy of 50 eV. Spectra were referenced to Au $4f_{7/2}$ at 84.0 eV.

References

1. Nuzzo, R. G.; Dubois, L. H.; Allara, D. L. *Journal of the American Chemical Society* **1990,** 112, (2), 558-569.

2. Greenler, R. G. *Journal of Chemical Physics* **1966,** 44, (1), 310-&.

3. Silverstein, R.; Webster, F.; Kiemle, D., *Spectrometric Identification of Organic Compounds*. 7 ed.; John Wiley & Sons, Inc.: New Jersey, 2005.

4. de Silva, D. S. M.; Zeng, X. B.; Ungar, G.; Spells, S. J. *Macromolecules* **2002,** 35, (20), 7730-7741.

5. Planche, J. P.; Revillon, A.; Guyot, A. *Journal of Polymer Science Part a-Polymer Chemistry* **1988,** 26, (2), 429-444.

6. Kim, N. Y.; Jeon, N. L.; Choi, I. S.; Takami, S.; Harada, Y.; Finnie, K. R.; Girolami, G. S.; Nuzzo, R. G.; Whitesides, G. M.; Laibinis, P. E. *Macromolecules* **2000,** 33, 2793-2795.

7. Langner, R.; Zundel, G. *Journal of Physical Chemistry* **1995,** 99, (32), 12214-12219.

8. Bard, A. J.; Faulkner, L. R., *Electrochemical Methods: Fundamentals and Applications*. 2nd ed.; Wiley: New York, 2001.

9. Nahir, T. M.; Bowden, E. F. *Electrochimica Acta* **1994,** 39, (16), 2347-2352.

10. Park, S. M.; Yoo, J. S. *Analytical Chemistry* **2003,** 75, (21), 455A-461A.

11. Monk, P. M. S., *Fundamentals of Electro-Analytical Chemistry*. John Wiley & Sons Ltd.: Chichester, England, 2001.

12. Herzog, G.; Arrigan, D. W. M. *Trac-Trends in Analytical Chemistry* **2005,** 24, (3), 208-217.

13. Jennings, G. K.; Laibinis, P. E. *Journal of the American Chemical Society* **1997,** 119, (22), 5208-5214.

14. Woollam, J. A.; Bungay, C.; Hilfiker, J.; Tiwald, T. *Nuclear Instruments & Methods in Physics Research Section B-Beam Interactions with Materials and Atoms* **2003,** 208, 35-39.

15. Laibinis, P. E.; Bain, C. D.; Nuzzo, R. G.; Whitesides, G. M. *Journal of Physical Chemistry* **1995,** 99, (19), 7663-7676.

16. Laibinis, P. E.; Palmer, B. J.; Lee, S.-W.; Jennings, G. K., Self-Assembled Monolayers of Thiols. In *Thin Films*, Ulman, A.; Powell, R.; Francombe, M. H., Eds. Academic Press: 1998; Vol. 24, pp 1-41.

17. Zisman, W. A., *Contact Angle, Wettability, and Adhesion*. American Chemical Society: Washington, D.C., 1964; Vol. 43.

18. Brundle, C. R.; Evans, C. A.; Wilson, S., *Encyclopedia of Materials Characterization: Surfaces, Interfaces, Thin Films*. Butterworth-Heinemann: Boston, 1992.

19. Garcia, R.; Perez, R. *Surface Science Reports* **2002,** 47, (6-8), 197-301.

20. Briggs, D.; Seah, M. P., *Practical Surface Analysis*. John Wiley & Sons Ltd.: Chichester, England, 1983.

CHAPTER IV

GROWTH AND STRUCTURE OF SURFACE-INITITATED POLY(N-ALKYLNORBORNENE) FILMS

Introduction

We report the development of a surface-initiated polymer film composed of poly(n-alkylnorbornene)s. Our approach (Figure 4.1) begins by preparing a vinyl-terminated monolayer on a gold substrate via exposure to allyl mercaptan. The terminal vinyl group is then reacted with a metathesis catalyst, immobilizing the catalyst on the substrate. The bound catalyst is then reacted with the desired monomer through ring-opening metathesis polymerization (ROMP) to create a surface-tethered poly(n-alkylnorbornene) film. This chapter reports the first surface-initiated growth of poly(n-alkylnorbornene) films as well as the first use of allyl mercaptan as a linkage between a substrate and a metathesis catalyst. Allyl mercaptan is a convenient choice, as it is inexpensive and commercially available. Previously reported thiol-based linking molecules all have been custom synthesized for the particular application.

Ring-opening metathesis polymerizations exhibit rapid kinetics under mild conditions, producing among the thickest surface-initiated films ever produced when norbornene is used as the monomer (> 1 μm).[1,4,15-17] Typical surface-initiated ROMP experiments are run for short time periods (< 60 min) at room temperature. The predominate ROMP monomers studied in surface-initiated cases have been norbornene and its functional derivatives,[1,4,5,15-18] due to the high reactivity of norbornene in ROMP and the ease of functionalized monomer synthesis.[19]

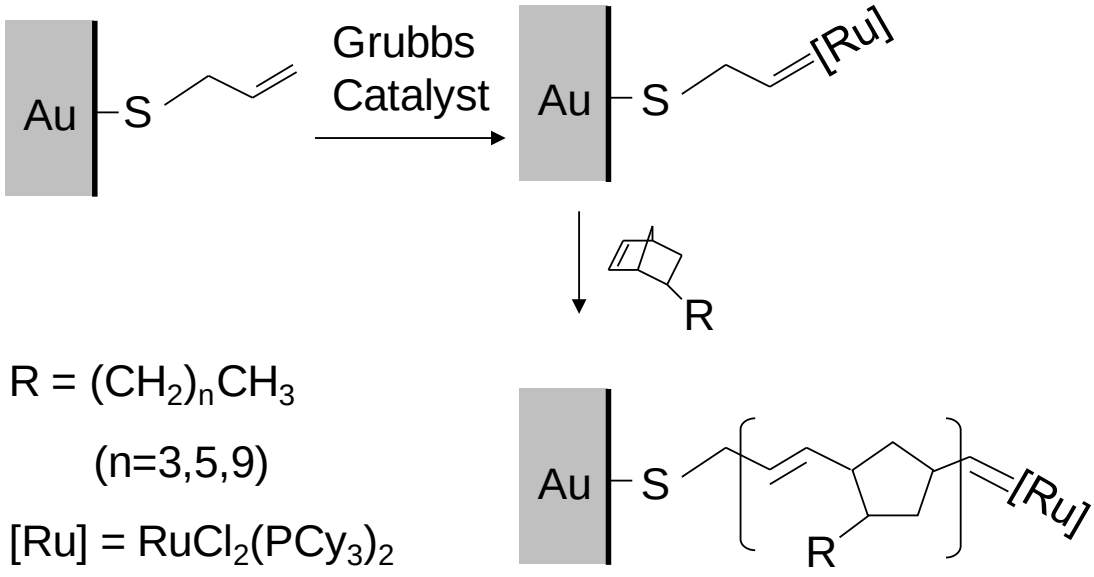

Figure 4.1. Schematic illustration of the gold surface preparation by attachment of allyl mercaptan, attachment of Grubbs' catalyst, and the ring-opening metathesis polymerization of alkylnorbornenes.

Functional derivatives of norbornene can polymerize to produce films with wide ranging properties and applications, including functionalization of chromatographic supports[15,20] to improve selectivity and modification of carbon nanotubes to improve dispersability in common solvents.[2] The conservation of the olefin functionality in these films provides an opportunity for further functionalization, which may lead to a wide variety of end uses for this family of films. Boyd and Schrock have demonstrated facile sulfonation and epoxidation of modified polynorbornenes.[21] A sulfonated thin film could be useful in proton/ion/water transport applications,[22] whereas an epoxide is a useful intermediate for further film functionalization including conversion to an alcohol.[21] For traditional barrier films, hydrogenation would be useful in preventing unwanted side reactions.[23,24] While surface-initiated poly(alkylnorbornene) films have yet to be

reported, Hatjopoulos and Register[23] recently published a study on the bulk elastomeric properties of ROMP-type poly(alkylnorbornene)s and their hydrogenated derivatives. They observed a decrease in glass transition temperature with increasing alkyl chain length which was attributed to the alkyl side chains of the polymer acting as plasticizers to disrupt packing within the polymer.

Previous studies have shown the polymerization kinetics of substituted norbornene monomers to be slower than that of norbornene.[23,25,26] The polymerization kinetics of n-alkylnorbornenes in solution using a Schrock-type catalyst was studied by Hatjopoulos and Register.[23] They reported a moderate decrease in the polymerization rate constant as the length of the alkyl side chain increased. The kinetic penalty associated with the alkyl side chain may be exaggerated on a surface due to steric hindrances associated with a solid support.

Here, we investigate the effect of alkyl chain length on the kinetics of surface-initiated polymerization of alkylnorbornenes. We use a series of poly(alkylnorbornene) films of comparable thickness to evaluate the dependence of film structure, as well as surface and barrier properties, on alkyl side chain length. Surface-initiated poly(alkylnorbornene) films should have a low surface energy, due to a surface composed of both methyl and methylene functionality. Surface-initiated ROMP has been shown to grow uniform coatings given appropriate monomers and reaction conditions.[1,4,17,27,28] We use AFM to investigate the uniformity and morphology of the surface initiated poly(alkylnorbornene) films and electrochemical impedance spectroscopy to measure the barrier properties of the films. The barrier properties of hydrocarbon-based surface-initiated films have been extensively studied, and show

excellent resistance to water and ion transport.[29-32] The barrier properties of some poly(alkylnorbornene) films should prove to have comparable film resistances to dense hydrocarbon-based surface-initiated films, making them suitable for numerous applications as surface coatings.

Experimental Procedures

Preparation of Poly(n-alkylnorbornene) Films

Gold substrates were placed in a 2.0 mM ethanolic solution of allyl mercaptan for 30 min. The initiator coated substrates were exposed to a 5 mM solution of Grubbs catalyst in dichloromethane for 15 min. The catalyst-coated films were rinsed with dichloromethane and immediately placed in a monomer solution containing either 0.27 M norbornene, 0.50 M butylnorbornene, or 1.89 M hexylnorbornene in dichloromethane for 15 min to achieve ~45 nm polymer films. Poly(decylnorbornene) films were analogously prepared with a 3.00 M solution of decylnorbornene in dichloromethane to yield ~10 nm polymer films. The films were sequentially rinsed with dichloromethane, ethanol, and water and dried in a nitrogen stream. Catalyst-coated films were immersed in 1.0 M monomer solutions for 10 s, 2, 15, and 60 min for the determination of kinetic rate constants. Samples for kinetic studies were also sonicated in dichloromethane for 2 min after polymerization to remove any unbound material.

Growth Kinetics

We investigated the kinetics of film growth by exposure of the ROMP-active monolayers to 1.0 M alkylnorbornene solutions for 10 s, 2, 15, and 60 min, followed by measuring the thicknesses of the resulting films. Figure 4.2 shows the experimental thickness for films grown from norbornene (NB), butylnorbornene (C4NB), hexylnorbornene (C6NB), and decylnorbornene (C10NB) monomers. At short times, the

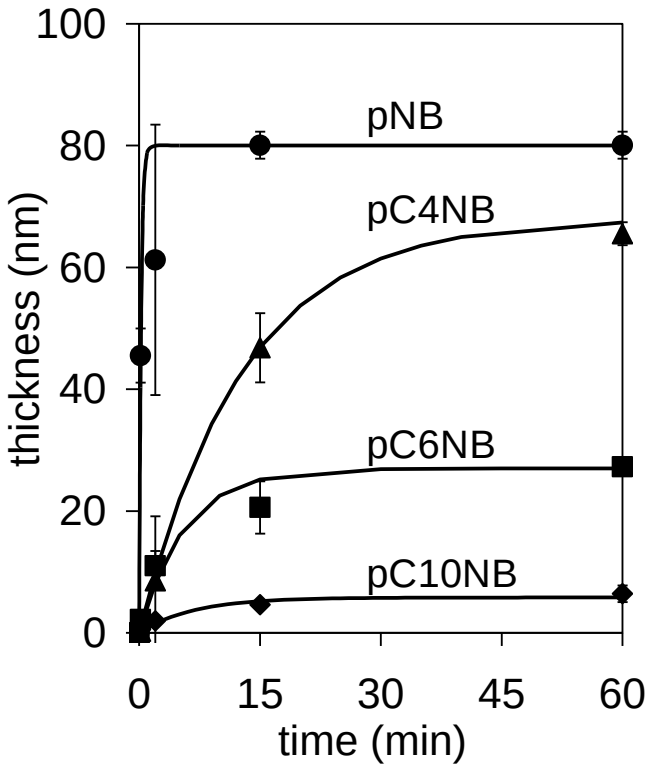

Figure 4.2. Ellipsometric film thickness of poly(alkylnorbornene) films grown from 1.0 M alkylnorbornene solutions in dichloromethane for the indicated times. Solid curves represent fits of the data using a polymerization kinetics model.

active chains grow and the thickness of the poly(alkylnorbornene) film increases rapidly with time. As the catalyst deactivates, the growth of the poly(alkylnorbornene) chains ceases and the film thickness approaches a constant value that decreases as the side chain length is increased.

The description of ROMP kinetics necessitates the determination of initiation, polymerization, and termination kinetic rate constants. As a tool to estimate the *relative* kinetics of film growth for this series of alkylnorbornenes, we begin with a simplified kinetic model set forth by Harada et al.,[27] which assumes an initial chain density. The time-dependence of film thickness (d) was given as

$$d = \left(\frac{k_p M}{k_t}\right)\left(\frac{m_o P_I}{\rho}\right)\left(1 - e^{-k_t t}\right) \tag{4-1}$$

where k_p is the propagation rate constant and k_t is an apparent, first-order termination rate constant, M is the monomer concentration, m_o is the mass of the monomer unit, P_I is the initial concentration of propagating chains, and ρ is the polymer density on the surface. Since P_I is unknown for this series of monomers and highly challenging to determine for films initiated from 2-D surfaces, we combine k_p and P_I as a single rate term (K) for film growth

$$K = k_p P_I \tag{4-2}$$

that reflects both initiation and propagation and enables an overall comparison of film growth kinetics for this series of monomers. The resulting equation becomes

$$d = \frac{KMm_o}{k_t \rho}\left(1 - e^{-k_t t}\right) \tag{4-3}$$

We also estimate the density of the polymer on the surface from the density of the monomer (~0.865 g/cm^3), as similar to others.[27,33] The rate constants obtained from this analysis are used to assess the relative reactivity of the monomers studied.

Table 4.1 contains estimates of K and k_t based on fits of the kinetic results with Equation 4-3. The rate constant for film growth (K) decreases with increasing length of the alkyl side chain, consistent with that found by Hatjopoulos and Register for the same monomers in solution using a Schrock-type catalyst.[23] While Hatjopoulos and Register reported a 37% decrease in the rate of polymerization from NB to C10NB, our surface-initiated system exhibits a three order of magnitude decrease in K over the same range of monomers. The contrast in the magnitude of change is not surprising due to the numerous differences (catalyst, cocatalyst, solvent, bulk vs. surface) between the system reported by Hatjopoulos and Register and the surface-initiated system we employed, especially considering that K here represents effects due to both initiation and propagation. The surface-immobilization of the catalyst will likely exaggerate the steric penalty associated with an alkyl substituent on the monomer over that of a solution polymerization. The choice of solvent also has a strong impact on film growth. While a 1.0 M NB solution can grow films of comparable thickness solvated in both toluene (56 nm) and dichloromethane (78 nm), the thickness of a film grown from 1.0 M C4NB is ~35 times

lower when grown in toluene (2 nm) versus dichloromethane (68 nm). Also shown in Table 4.1, the termination rate constant is reduced by a factor of 20 - 50 for n-alkylnorbornenes as compared with norbornene. The reduction is attributable to the alkyl side chain sterically hindering coupling and backbiting[27] (secondary-metathesis) based termination reactions.

Table 4.1. Relative Film Growth and Termination Rate Constants for Surface-Initiated Growth in Dichloromethane

Monomer	K (m s^{-1})	k_t (s^{-1})
NB	5.0×10^{-8}	0.0700
C4NB	5.0×10^{-10}	0.0013
C6NB	4.0×10^{-10}	0.0030
C10NB	5.3×10^{-11}	0.0025

Influence of n-Alkyl Side Chains on Film Composition and Structure

We used RAIRS to probe the composition and structure of the polynorbornene films. Control of the NB, C4NB, and C6NB monomer concentration allowed the growth of films of comparable thicknesses (~45 nm). The limited reactivity of the C10NB monomer prohibited the growth of 45 nm films; thus, ~8 nm pC10NB films are used for comparison. Figure 4.3 shows the relevant regions of representative RAIR spectra for all polymer films studied. The C-H stretching region of the RAIR spectra for polynorbornene consists of strong cyclic methylene stretching peaks (υ_{as} = ~2948 cm^{-1}, υ_s = ~2866 cm^{-1}) as well as a less intense tertiary C-H stretching peak at ~2911 cm^{-1}.[34] The position of the methylene scissoring peak at ~1450 cm^{-1} is indicative of purely cyclic methylene functionality.[35] The olefin functionality is observed in the trans C=CH out of plane bending[34,35] peak (968 cm^{-1}) and the C=CH stretching peak (3030 cm^{-1}). Other groups have reported peak positions consistent with our observations.[4,34]

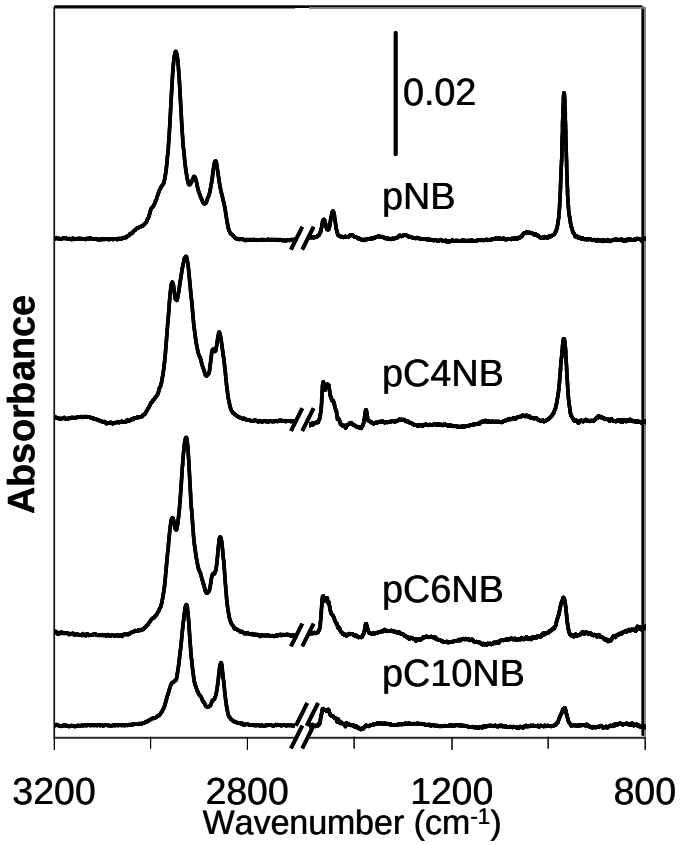

Figure 4.3. Reflectance-absorption infrared spectra of the indicated polymer films. The spectra have been offset vertically for clarity.

The addition of an n-alkyl side chain to the 5 position of the norbornene monomer alters the composition and structure of the resulting polymer. The polymer films with longer alkyl substituents exhibit increased n-alkyl functionality in the RAIR spectra with diminished polynorbornene functionality when compared to their shorter chained analogues. Specifically, the contribution of the acyclic methylene stretching (υ_{as} = 2926-28 cm^{-1}, υ_s = 2854-58 cm^{-1}) increases while the contributions of the cyclic methylene stretching (υ_{as} = 2948-2955 cm^{-1}, υ_s = 2866-71 cm^{-1}) and the trans C=CH out of plane bending (968-9 cm^{-1}) decrease in an inversely proportional fashion. The shift of the

methylene scissoring peak with the addition of the alkyl side chain is indicative of a deviation from a purely cyclic methylene component (δ CH_2 ~1447 cm^{-1}) toward a largely acyclic film (δ CH_2 ~1467 cm^{-1}).[35] The positions of the cyclic methylene stretching peaks in the poly(alkylnorbornene)s are shifted towards higher wavenumbers (υ_{as} = ~2955 cm^{-1}, υ_s = ~2870 cm^{-1}) indicative of a less crystalline conformation of the cyclopentane groups as compared to those in the original poly(norbornene) film.

Table 4.2. Peak Positions From RAIR Spectra

	Wavenumber (cm^{-1})			
Mode	pNB	pC4NB	pC6NB	pC10NB
υ - CH_2 cyclic	2948	2955	2955	2955
υ - CH_2 cyclic	2866	2871	2869	2871
υ – CH	2911	-	-	-
υ_{as} - CH_2 acyclic	-	2928	2927	2926
υ_s - CH_2 acyclic	-	2858	2856	2854
δ - CH_2 scissor	1466 / 1447	1467	1467	1468
δ - C=CH	968	968	969	969

Previous studies on polymethylene chains with highly crystalline chain packing exhibit asymmetric (υ_{as}) and symmetric (υ_s) methylene stretching at ~2918 cm^{-1} and ~2850 cm^{-1}, respectively, while polymethylene chains in a liquid-like packing are shifted to higher wavenumbers. The poly(alkylnorbornene) films exhibit asymmetric and symmetric methylene stretching peaks at ~2926-28 cm^{-1} and ~2854-8 cm^{-1} (Table 4.2) indicative of liquid-like alkyl packing,[36] with incrementally more crystalline packing (lower wavenumber) as alkyl chain length is increased. We previously observed a comparable correlation in alkyl chain length with peak position in poly(hydroxyethyl methacrylate) films with n-alkyl side chains.[30] The greater van der Waals interactions

between the longer n-alkyl chains likely drives the slight improvement in crystallinity in these polymers.[30]

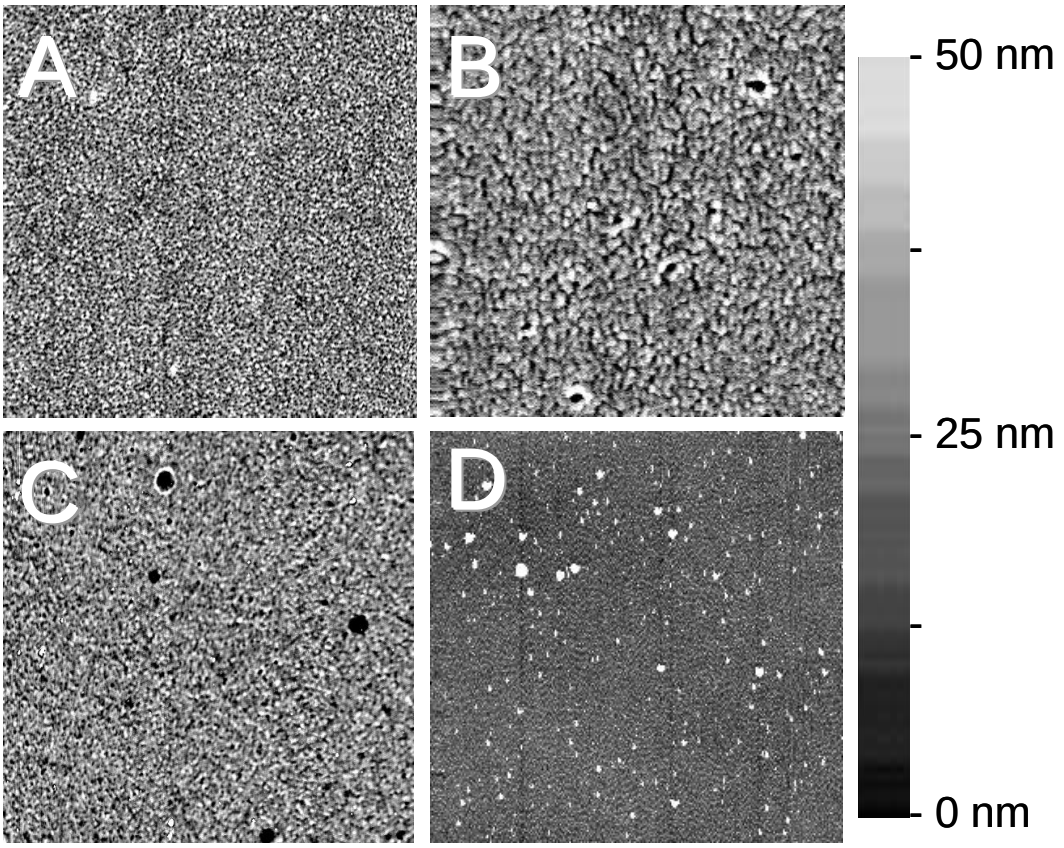

Figure 4.4. Atomic force microscopy images (25 μm x 25 μm) of pNB (A), pC4NB (B), pC6NB (C), and pC10NB (D) films.

Though the RAIR spectra demonstrate a slight increase in alkyl crystallinity in the poly(alkylnorbornene) films with increasing side chain length, the crystallinity of the remainder of the film is likely hindered due to internal plasticization.[37] Hatjopoulos and Register have reported a T_g decrease in bulk ROMP-type poly(alkylnorbornene)s with an increase in side chain length, a strong indication that the structuring of the polymers and the analogous surface initiated films is disrupted by moderate length alkyl chains.[23]

We used AFM to determine the morphology of the pNB and polyalkylnorbornene films. The surface-initiated polymerization of NB, C4NB, and C6NB generated a dense polymer coating (~45 nm) on the gold surface (Figure 4.4).[38] The small pinholes observed for the pC4NB and pC6NB are similar to much larger holes formed for pNB when NB was obtained from a different supplier (see Supporting Information).[1] In contrast, the polymerization of C10NB resulted in the growth of polymeric islands on the gold surface. The ellipsometric film thickness for the pC10NB polymer layers (~8 nm) is used as a means to quantify the polymer on the surface and is not indicative of a true 8 nm film.

Contact angle goniometry is used to qualitatively access the composition and roughness of the surface of a film. Table 4.3 shows the advancing and receding water and hexadecane contact angles collected on all films studied. The advancing water contact angle for pNB ($\theta_A(H_2O)$ ~106°) is consistent with a predominant CH_2 surface and is similar to values of ~103° reported on polyethylene surfaces.[39] The contribution of the methyl terminus on the alkyl chain causes an increase in hydrophobicity in the pC4NB, pC6NB, and pC10NB films ($\theta_A(H_2O)$ = 109°-114°), comparable to values obtained on pure methyl surfaces of SAMs ($\theta_A(H_2O)$ = 115°).[40] The low surface tension of hexadecane amplifies surface energy differences in low energy films and allows a more distinguishing measure of the surface properties of low energy films via contact angle goniometry. The predominant CH_2 surface of the pNB film allows the wetting of the surface by hexadecane ($\theta_A(HD) < 15°$). The methyl functionality of the pC4NB films causes an increase in the hexadecane contact angle to 29°. Interestingly, the hexadecane contact angle decreases as the length of the alkyl side chain increases to that of a pC6NB

(θ_A(HD) = 23°) and a pC10NB film (θ_A(HD) < 15°). The additional length of the alkyl side chain of the polymer dilutes the methyl functionality, which is responsible for the oleophobicity of the film. In the case of pC10NB, the cluster-like morphology (see Figure 4.4D) leads to a lower hexadecane and higher water contact angles, as predicted by the effect of roughness on contact angles.[2,41,42]

Table 4.3. Water and Hexadecane Advancing and Receding Contact Angles (°) for Films on Gold

	water		Hexadecane	
Film	θ_A	θ_R	θ_A	θ_R
pNB	106 ± 2	81 ± 3	<15	<15
pC4NB	109 ± 2	83 ± 4	29 ± 5	<15
pC6NB	114 ± 2	78 ± 3	23 ± 5	<15
pC10NB	113 ± 2	81 ± 1	<15	<15

Barrier Properties

We used electrochemical impedance spectroscopy to investigate the barrier properties of the surface-initiated poly(alkylnorbornene) films in the presence of $K_3Fe(CN)_6$ and $K_4Fe(CN)_6$ in 0.1 M $NaSO_4$ (aq). Representative Bode plots for ~45 nm films of pNB, pC4NB, and pC6NB are shown in Figure 4.5. Due to the limited reactivity of the C10NB monomer, an ~8 nm pC10NB films is used. The impedance spectra of the polymer films are best fit with a Randle's equivalent circuit[43] modified with a Warburg impedance term to account for a resistance to mass transfer.[44] Table 4.4 shows film thicknesses along with the resistance (R_f) of the films against penetration by redox probes, and capacitance (C_f) values. Good barrier films typically exhibit high resistance and low capacitance values.[2,30-32,44] The film resistances (R_f~10^5 Ω•cm^2) and capacitances (~200 nF) of the pNB, pC4NB, and pC6NB films are comparable to that of

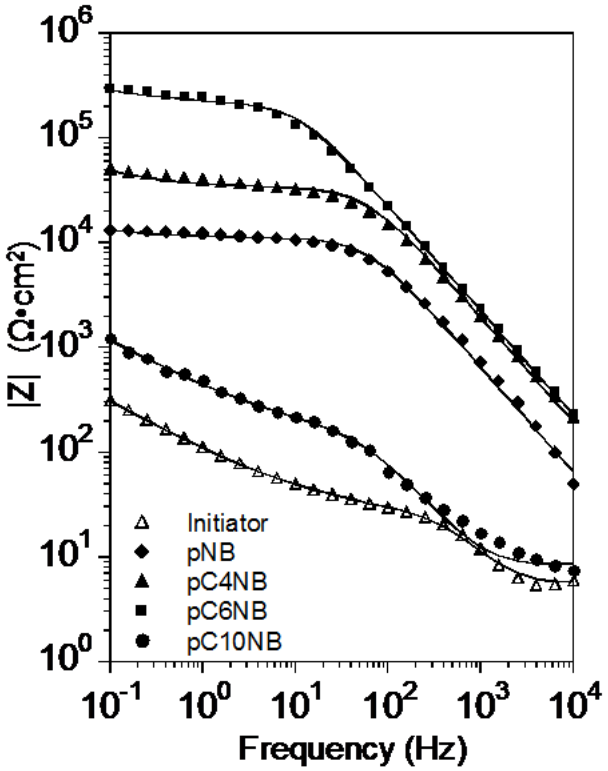

Figure 4.5. Electrochemical impedance spectra obtained in 1 mM $K_3Fe(CN)_6$ and 1 mM $K_4Fe(CN)_6$ in 0.1 M Na_2SO_4(aq) for the indicated films on gold. Solid curves represent fits of the data using appropriate equivalent circuit models.

Table 4.4. Film Capacitance, Resistance and Ellipsometric Thickness Values for pNB and poly(alkylnorbornene) films

Film	thickness (nm)	log(R_f) (Ω•cm^2)	C_f (nF/cm^2)
vinyl linkage/catalyst	not measured	1.3 ± 0.1	19000 ± 1200
pNB	49 ± 2	4.3 ± 0.6	250 ± 170
pC4NB	47 ± 5	4.5 ± 0.5	140 ± 60
pC6NB	42 ± 7	5.1 ± 0.6	150 ± 50
pC10NB	8 ± 2	2.2 ± 0.2	11000 ± 4000

other hydrocarbon surface-initiated films with a pronounced increase in film resistance as the chain length of the hydrophobic alkyl group is increased.[30] When compared to pNB, the increase in resistance due to the added hydrophobicity for the pC4NB and pC6NB appears to outweigh the greater density of pinholes in these films (Figure 4.4). The low

film resistance ($R_f \sim 10^2$ $\Omega \bullet cm^2$) and high capacitance (C_f ~11 μF) of the pC10NB films are attributed to the non-uniform, cluster-like film growth as shown in Figure 4.4D.

Conclusions

The preparation of surface-initiated ROMP-type poly(n-alkylnorbornene) films is easily achieved through three sequential and rapid reactions, including assembly of allyl mercaptan, catalyst attachment, and polymerization. Polymerization of butylnorbornene and hexylnorbornene yields dense films with liquid-like packing of the alkyl side chains whereas decylnorbornene polymerizes into discrete clusters. Increasing the length of the alkyl side chain on the monomer decreases the rate of film growth and limits the ultimate thickness of the polymer film. The methyl terminus of the alkyl side chains decreases the surface energy beyond that of a typical polynorbornene film. The added hydrophobicity of pC4NB and pC6NB correlates with an enhanced resistance against redox probes as compared with pNB films, while barrier properties of the pC10NB are consistent with a poor coverage of the metallic substrate. These films contain internal olefin groups to enable further reactive processing and tailorability of film and surface properties, which will be discussed in the following chapter.

References

1. Rutenberg, I. M.; Scherman, O. A.; Grubbs, R. H.; Jiang, W.; Garfunkel, E.; Bao, Z. *J. Am. Chem. Soc.* **2004,** 126, 4062-4063.

2. Jennings, G. K.; Brantley, E. L. *Adv. Mater.* **2004,** 16, 1983-1994.

3. Buchmeiser, M. R., Metathesis polymerization to and from surfaces. In *Surface-Initiated Polymerization I*, 2006; Vol. 197, pp 137-171.

4. Kim, N. Y.; Jeon, N. L.; Choi, I. S.; Takami, S.; Harada, Y.; Finnie, K. R.; Girolami, G. S.; Nuzzo, R. G.; Whitesides, G. M.; Laibinis, P. E. *Macromolecules* **2000,** 33, 2793-2795.

5. Jordi, M. A.; Seery, T. A. P. *J. Am. Chem. Soc.* **2005,** 127, (12), 4416-4422.

6. Matyjaszewski, K.; Miller, P. J.; Shukla, N.; Immaraporn, B.; Gelman, A.; Luokala, B. B.; Siclovan, T. M.; Kickelbick, G.; Vallant, T.; Hoffmann, H.; Pakula, T. *Macromolecules* **1999,** 32, (26), 8716-8724.

7. Boyes, S. G.; Brittain, W. J.; Weng, X.; Cheng, S. Z. D. *Macromolecules* **2002,** 35, 4960-4967.

8. Kim, J.-B.; Huang, W.; Bruening, M. L.; Baker, G. L. *Macromolecules* **2002,** 35, 5410-5416.

9. Zhou, F.; Liu, W. M.; Hao, J. C.; Xu, T.; Chen, M.; Xue, Q. J. *Advanced Functional Materials* **2003,** 13, (12), 938-942.

10. Husemann, M.; Mecerreyes, D.; Hawker, C. J.; Hedrick, J. L.; Shah, R.; Abbott, N. L. *Angewandte Chemie-International Edition* **1999,** 38, (5), 647-649.

11. Bai, D. S.; Habersberger, B. M.; Jennings, G. K. *J. Am. Chem. Soc.* **2005,** 127, (47), 16486-16493.

12. Ayres, N.; Boyes, S. G.; Brittain, W. J. *Langmuir* **2007,** 23, (1), 182-189.

13. Balachandra, A. M.; Baker, G. L.; Bruening, M. L. *Journal of Membrane Science* **2003,** 227, (1-2), 1-14.

14. Bai, D. S.; Elliott, S. M.; Jennings, G. K. *Chemistry of Materials* **2006,** 18, (22), 5167-5169.

15. Buchmeiser, M. R.; Sinner, F.; Mupa, M.; Wurst, K. *Macromolecules* **2000,** 33, (1), 32-39.

16. Weck, M.; Jackiw, J. J.; Rossi, R. R.; Weiss, P. S.; Grubbs, R. H. *J. Am. Chem. Soc.* **1999,** 121, 4088-4089.

17. Liu, X. G.; Guo, S. W.; Mirkin, C. A. *Angew. Chem. Int. Ed.* **2003,** 42, (39), 4785-4789.

18. Li, X. M.; Huskens, J.; Reinhoudt, D. N. *Nanotechnology* **2003,** 14, (10), 1064-1070.

19. Pasquale, A. J.; Fornof, A. R.; Long, T. E. *Macromolecular Chemistry and Physics* **2004,** 205, (5), 621-627.

20. Buchmeiser, M. R. *Macromolecular Rapid Communications* **2001,** 22, (14), 1082-1094.

21. Boyd, T. J.; Schrock, R. R. *Macromolecules* **1999,** 32, (20), 6608-6618.

22. Iojoiu, C.; Marechal, M.; Chabert, F.; Sanchez, J. Y. *Fuel Cells* **2005,** 5, (3), 344-354.

23. Hatjopoulos, J. D.; Register, R. A. *Macromolecules* **2005,** 38, (24), 10320-10322.

24. Lee, L. B. W.; Register, R. A. *Macromolecules* **2005,** 38, (4), 1216-1222.

25. Seehof, N.; Grutke, S.; Risse, W. *Macromolecules* **1993,** 26, (4), 695-700.

26. Feast, W. J.; Gimeno, M.; Khosravi, E. *Journal of Molecular Catalysis a-Chemical* **2004,** 213, (1), 9-14.

27. Harada, Y.; Girolami, G. S.; Nuzzo, R. G. *Langmuir* **2003,** 19, (12), 5104-5114.

28. Juang, A.; Scherman, O. A.; Grubbs, R. H.; Lewis, N. S. *Langmuir* **2001,** 17, (5), 1321-1323.

29. Guo, W.; Jennings, G. K. *Adv. Mater.* **2003,** 15, 588-591.

30. Brantley, E. L.; Holmes, T. C.; Jennings, G. K. *Journal of Physical Chemistry B* **2004,** 108, (41), 16077-16084.

31. Bantz, M. R.; Brantley, E. L.; Weinstein, R. D.; Moriarty, J.; Jennings, G. K. *Journal of Physical Chemistry B* **2004,** 108, (28), 9787-9794.

32. Brantley, E. L.; Holmes, T. C.; Jennings, G. K. *Macromolecules* **2005,** 38, (23), 9730-9734.

33. Yamamoto, S.; Ejaz, M.; Tsujii, Y.; Fukuda, T. *Macromolecules* **2000,** 33, (15), 5608-5612.

34. Planche, J. P.; Revillon, A.; Guyot, A. *Journal of Polymer Science Part a-Polymer Chemistry* **1988,** 26, (2), 429-444.

35. Silverstein, R.; Webster, F.; Kiemle, D., *Spectrometric Identification of Organic Compounds*. 7 ed.; John Wiley & Sons, Inc.: New Jersey, 2005.

36. Berron, B.; Jennings, G. K. *Langmuir* **2006,** 22, 7235-7240.

37. Internal plasticization is a phenomenon where polymer side chains disrupt the overall polymer packing.

38. AFM images obtained from different norbornene feedstocks is included in Supporting Information.

39. Holmes-Farley, S. R.; Reamey, R. H.; McCarthy, T. J.; Deutch, J.; Whitesides, G. M. *Langmuir* **1985,** 1, (6), 725-740.

40. Laibinis, P. E.; Whitesides, G. M.; Allara, D. L.; Tao, Y. T.; Parikh, A. N.; Nuzzo, R. G. *J. Am. Chem. Soc.* **1991,** 113, (19), 7152-7167.

41. Wenzel, R. W. *Industrial and Engineering Chemistry* **1936,** 28, (8), 988-994.

42. Sun, T. L.; Wang, G. J.; Feng, L.; Liu, B. Q.; Ma, Y. M.; Jiang, L.; Zhu, D. B. *Angewandte Chemie-International Edition* **2004,** 43, (3), 357-360.

43. Jennings, G. K.; Laibinis, P. E. *Journal of the American Chemical Society* **1997,** 119, (22), 5208-5214.

44. Brantley, E. L.; Jennings, G. K. *Macromolecules* **2004,** 37, 1476-1483.

CHAPTER V

SULFONATION OF SURFACE INITITATED POLYNORBORENENES

Introduction

The unique chemical behavior of sulfonated polymer films has made them of particular interest in modern technologies. Sulfonated polymers are well established as the standard in proton exchange media for fuel cells.[1-5] These polymers are commonly prepared as thick films by solution casting,[6-8] a method that is inadequate to achieve conformal coatings on irregular substrates that are becoming utilized as fuel cell architectures evolve.[7,9-12] Sulfonated polymers are also useful in ion exchange applications including water purification and desalination.[13,14] Alternative sulfonated polymeric structures are of relevance given the increasing research interest in efficiently extracting water from saltwater sources.[13]

The abundance of naturally occurring biopolymers which include or interact with sulfonate functionality suggests the promise that sulfonated polymer surfaces hold for applications as biomimetic materials. Eckenrode and Dai recently highlighted the ability for sulfonated polystyrene surfaces to adsorb positively charged polylysine.[15] The biological adsorption of charged molecules has shown to play a key role in immunoadsorption as well as blood clotting.[16] Huck and coworkers recently reported the application of silver-loaded poly(3-sulfopropylmethacrylate) films as an antibacterial surface.[17] The ion exchange properties of new types of sulfonated polymer surfaces, as

well as the ability to incorporate these films into more complex architectures should continue to drive the development of the next generation of biomaterials.

Surface-initiated polymerization offers advantages over spin coating and solution casting due to a chemisorbed linkage of the polymer to the surface,[18-23] the ability to conformally coat substrates of any geometry,[18,24,25] and the exceptional film uniformity at a low film thickness.[21,26-28] Surface-initiated films with sulfonate functionality are typically prepared through the growth and sulfonation of polystyrene. [29,30] Alternatively, the growth and sulfonation of polynorbornene films would be advantageous because they are grown rapidly through ring-opening metathesis polymerization (ROMP), yielding an 80 nm film after 15 min of polymerization at room temperature.[31] In contrast, almost 36 h at temperatures in excess of 75˚C are required to grow polystyrene films of comparable thickness.[29,30] The surface-initiated polymerization of a sulfonate-containing monomer via atom transfer radical polymerization (ATRP) also has slow polymerization rates when compared to ROMP, requiring over 5 h to grow an 80 nm film.[17] The tailorable functionality of norbornene-based monomers allows for a variety of modified ROMP-type films to be sulfonated films via an analogous approach.[32]

Here, we demonstrate the growth and sulfonation of surface-initiated polynorbornene films. Our approach is outlined in Figure 5.1. An alcohol-terminated self-assembled monolayer (SAM) (Au/SC_4OH) is prepared by exposure of a gold coated silicon substrate to 1-mercapto-4-butanol. The alcohol-terminated monolayer is then reacted with a diacid-chloride-functionalized norbornene ($NB(COCl)_2$) to tether the norbornene group to the surface via ester linkages. Exposure to Grubbs first generation catalyst results in a submonolayer of immobilized ROMP-active catalyst.[24] The bound

catalyst is then reacted with the appropriate norbornene (NB) monomer, resulting in a surface-tethered ROMP-type polymer film, which is then sulfonated by exposure to freshly-prepared acetyl sulfate. The immobilization of an acid chloride functionalized norbornene on an alcohol terminated monolayer is a fast and convenient method for achieving a norbornene-decorated surface through the sequential exposure to commercially available materials. This approach allows techniques based on SAMs to control the nature of the linkage of the polymer to the underlying gold support.

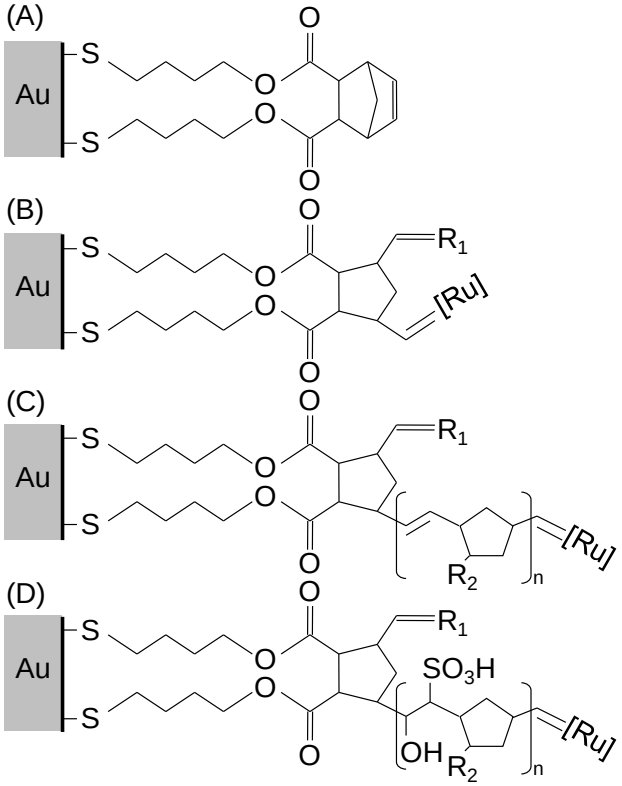

Figure 5.1. Schematic illustration of the gold surface preparation by attachment of the norbornenyl decorated SAM system (A), attachment of Grubbs' catalyst (B), the ring-opening metathesis polymerization of norbornene (C) and the sulfonation of the surface tethered film (D). [Ru] = $(PCy_3)_2Cl_2Ru$, Cy= cyclohexyl. R_1 = CHPh. R_2 = -H for polynorbornene, $-(CH_2)_3CH_3$ for poly(butylnorbornene). Figure not indicative of actual bond lengths and angles.

The versatility of olefin chemistry offers many reaction pathways for the sulfonation of polynorbornene.[33] Typically, the unsaturated polymer is exposed to an adduct of sulfur trioxide yielding a highly unstable β-sultone. Upon exposure to water, the sultone is rapidly converted to either an olefinic sulfonate or a hydroxylsulfonate.[32,33] The distinction between the products is determined by the nature of the adduct as well as the olefin.[33,34] Previously, Planche et al. have sulfonated solution-phase polynorbornene with the SO_3-triethylphosphate adduct yielding almost exclusively an olefinic sulfonate product.[34,35] In the interest of polymer stability, the persistence of the olefin functionality in the sulfonated product is not desirable. Boyd and Schrock have published a study on the solution-phase sulfonation reaction of modified polynorbornenes using an SO_3-dioxane adduct.[32] They observed >80% conversion of the olefin as well as selectivity towards the more desirable hydroxylsulfonate product. Dioxane was chosen as a complexing reagent, due to the lack of reactivity of SO_3-dioxane with the aromatic sidechains present in their studies.[32] Hoffman and Simchen developed a more convenient preparation of SO_3-dioxane by observing the addition of dioxane to trimethylsilyl chlorosulfonate yields SO_3-dioxane and chlorotrimethylsilane,[36,37] alleviating the need to use sulfur trioxide as a reagent. The chloromethylsilane byproduct is typically removed by vacuum distillation. Acetyl sulfate is another conveniently prepared, reactive sulfonation reagent achieved by the stoichiometric addition of sulfuric acid to acetic anhydride.[38,39] Acetyl sulfate has been shown to be reactive with olefin functionality to generate a β-sultone[39] and is promising for utility in the sulfonation of polynorbornene.

Here, we investigate the use of acetyl sulfate as a sulfonation reagent for surface-tethered polynorbornene and poly(butylnorbornene) and the applicability of these

materials as proton-conducting films. We use reflectance-absorption infrared spectroscopy (RAIRS) to probe the structural and chemical changes during sulfonation. In Chapter IV, we demonstrated the uniformity of surface-initiated polynorbornene and poly(butylnorbornene) films.[31] Here, we use optical microscopy to investigate the microscopic changes in film morphology upon sulfonation and further surface treatment. Electrochemical impedance spectroscopy is used to determine the proton transport properties of the films. We have previously reported that surface-initiated polynorbornene films provide excellent resistance to the transport of water and large ions.[31] Upon sulfonation, the sulfonate functionality of the polymer should provide hydrophilic domains in the polymer structure which facilitate proton and water transport through the film. The reorganization of polymers into hydrophobic and hydrophilic domains is known to be vital to proton transport through commercial proton exchange membranes due to a water-mediated proton transport mechanism.[1,3,4] In addition, we highlight the versatility of this sulfonation procedure through the sulfonation of surface initiated poly(n-butylnorbornene).

Experimental Section

Preparation of Polymer Films

Gold substrates were placed in a 1.0 mM ethanolic solution of 4-mercapto-1-butanol for at least 60 min to yield a hydroxyl-terminated self-assembled monolayer. The samples were rinsed in ethanol and dried in a stream of nitrogen. Exposure of the SAM to a 5.0 mM solution of trans-3,6-endo-methylene-1,2,3,6-tetrahydrophthaloyl chloride in

dichloromethane for 30 min yields the acylation product of a surface tethered norbornenyl group. The samples were rinsed in ethanol and dried in a stream of N_2. The norbornenyl decorated substrates were exposed to a 5 mM solution of Grubbs catalyst in dichloromethane for 15 min. The catalyst-coated films were rinsed with dichloromethane and immediately placed in a monomer solution containing 1.0 M norbornene in toluene for 15 min to achieve ~120 nm polymer films. The films were sequentially rinsed with toluene, ethanol, and water and dried in a stream of nitrogen. Poly(n-butylnorbornene) films were prepared analogously using a monomer solution containing 1.0 M 5-n-buytlnorbornene in dichloromethane.

Sulfonation

A 1.0 M acetyl sulfate solution in dichloromethane was prepared immediately prior to use similar to Tran et al.[38] Acetic anhydride (2.8 mL) was added to dichloromethane (14.0 mL) at 0˚C. Concentrated sulfuric acid (1.0 mL) was added dropwise to the acetic acid solution resulting in a 1.0 M acetyl sulfate solution in DCM. 1.0 mL of the 1.0 M acetyl sulfate solution was diluted to 0.1 M through the addition of 9.0 mL of dichloromethane. Polymer-coated substrates were exposed to the 1.0 M solution of acetyl sulfate for 60 s to yield a surface-tethered sulfonated polymer coating. Samples were rinsed with dichloromethane and ethanol and dried in a nitrogen stream. The resulting polymer films were exposed to dimethyl sulfoxide (DMSO) for 5 to 30 min.

Polarization Modulation Infrared Reflection Absorption Spectroscopy

IR spectra of monolayer films were collected using polarization modulation infrared reflection absorption spectroscopy (PM-IRRAS). Data were collected using a Bruker PMA-50 attachment on a Bruker Tensor 26 infrared spectrometer equipped with a liquid-nitrogen-cooled MCT detector and a Hinds Instruments PEM- 90 photoelastic modulator. The source beam was modulated at a frequency of 50 kHz with half-wavelength retardation and set at 80° incident to the sample surface. Spectra for SAMs on gold substrates were collected over 5 min (380 scans) at a resolution of 4 cm^{-1}. The differential reflection spectra ($\Delta R/R$) were calculated from the s- and p-polarized signals simultaneously collected by a lock-in-amplifier. All reported IR spectra were repeated at least twice using independent sample preparations.

Hydrolysis of Surface-Tethered Unreacted Acid Chlorides

Norbornenyl decorated SAMs were rinsed with water or ethanol for 30 s immediately after exposure to $NB(COCl)_2$. Samples were then dried in a stream of nitrogen. IR Spectra were collected via PM-IRRAS.

Proton Conductivity Study

Electrochemical impedance spectroscopy (EIS) was performed with a Gamry Instruments CMS300 impedance system interfaced to a personal computer. A flat cell (EG&G) was used to selectively expose 1.0 cm^2 of each sample as the working electrode to an aqueous solution of 0.1 M H_2SO_4. Measurements were taken using a Ag/AgCl/saturated KCl reference electrode with evaporated gold on silicon as the

counter electrode. Data were collected between 10^{-1} and 10^{5} Hz and fit using an appropriate equivalent circuit[40] to determine film resistance, film capacitance and interfacial capacitance values, where applicable. Data collected between 10^{4} and 10^{5} Hz were omitted from the analysis due to inductive interference. Reported values and errors represent the averages and standard deviations, respectively, from at least 6 different films.

Results and Discussion

Growth of Surface-Initiated Polynorbornene

The exposure of a gold coated Si substrate to an ethanolic solution of 4-mercapto-1-butanol results in a thin, hydroxyl-terminated SAM on gold. The high surface energy ($\theta_A(H_2O) \sim 36^\circ$) of the SAM surface is consistent with that of a thin hydroxyl-terminated SAM. Hydroxyl-terminated SAMs on gold with 6 or fewer carbons in the thiolate backbone have been shown to exhibit a unique striped structure driven by intermolecular hydrogen bonding.[41] The striped structure leads to films that are thinner and of a more intermediate surface energy than predicted by the trans-extended, canted structure known to SAMs on gold with 10 or more carbons in the alkyl backbone.[42-45] The combination of the thin structure of the SAM and the typical adventitious layer of carbon on a bare gold substrate[44] results in the inability to ellipsometrically distinguish the SAM monolayer from the gold background (Table 5.1). Nonetheless, the presence of this SAM is required to anchor the norbornenyl group and initiate polymerization (*vide infra*), as no polymer is grown when this step is omitted.

Table 5.1. Ellipsometric Thicknesses Values, Advancing and Receding Water Contact Angles for Specified Films

Film	Thickness (nm)	θ_A(water) (°)	θ_R(water) (°)
-SC_4OH SAM	0.06 ± 0.09	36 ± 1	<10
NB decorated SAM	0.19 ± 0.08	59 ± 2	12 ± 6
catalyst decorated SAM	0.77 ± 0.27	62 ± 1	17 ± 4
pNB	120 ± 32	101 ± 1	74 ± 4
sulfonated pNB	71 ± 38	75 ± 7	<10

The immobilization of norbornenyl functionality is accomplished by exposure of the hydroxyl-terminated SAM to trans-3,6-endo-methylene-1,2,3,6-tetrahydrophthaloyl chloride ($NB(COCl)_2$) in dichloromethane. $NB(COCl)_2$ can attach to the hydroxyl surface by reacting to produce one or two ester linkages. We investigated the multiplicity of $NB(COCl)_2$ attachment to the monolayer via observation of ester formation using PMIRRAS. Immediately after the exposure to $NB(COCl)_2$, the films were rinsed with water for 30 s to hydrolyze the acid chloride of any norbornenyl groups only tethered by one ligand. As a control, separate samples were rinsed with ethanol to react with untethered acid chloride to form ethyl esters. In the IR spectrum, carbonyl stretching due to carboxylate ($\upsilon_{C=O}$ ~ 1560 cm^{-1}) and carboxylic acid ($\upsilon_{C=O}$ ~ 1710 cm^{-1}) functionality is differentiated from that due to ester ($\upsilon_{C=O}$ ~ 1735 cm^{-1}) functionality,[23,40,46,47] allowing a relative determination of the multiplicity of norbornenyl attachment through peak area integration. The IR spectra of the water rinsed samples (Figure 5.2 B) indicate additional carboxylate functionality at 1560 cm^{-1}. The IR spectra of ethanol rinsed samples (Figure 5.2 A) show a lower signal to noise ratio while indicating a lack of carboxylate functionality at 1560 cm^{-1}. Integration of peak areas for the carbonyl stretching due to ester and carboxylate functionality allows an estimation of the mean multiplicity (f) of norbornenyl attachment using equation 5-1.

$$f = \frac{A_{ester} - \frac{A_{ester} + A_{carboxylate}}{2}}{\frac{A_{ester} + A_{carboxylate}}{2}} + 1 \quad (5\text{-}1)$$

The majority (~92%) of the norbornenyl groups were attached via two ester bonds to the underlying monolayer. The resulting two ester attachment to the monolayer results in a chelated system which should improve the stability of the bound species.[48,49]

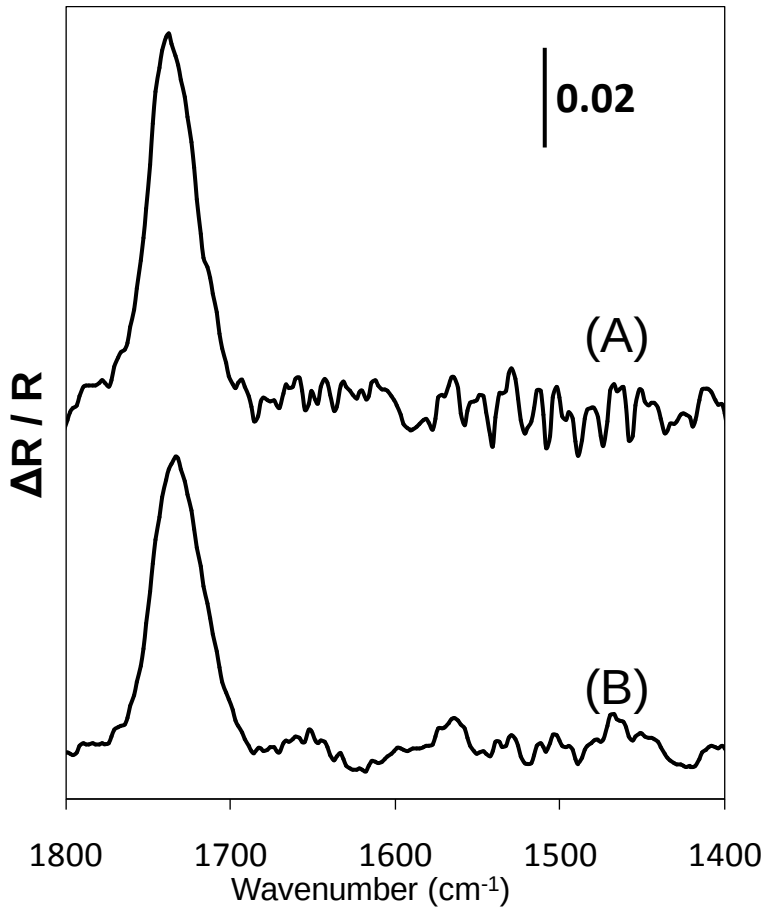

Figure 5.2. PM-IRRAS spectra of norbornenyl capped monolayers exposed to (A) ethanol or (B) water.

The increase in the advancing water contact angle ($\theta_A(H_2O) \sim 59^\circ$) over that of the SAM ($\theta_A(H_2O) \sim 36^\circ$) is consistent with the introduction of an incomplete adlayer of norbornenyl groups on a hydroxyl surface. We estimate the volume of the surface tethered norbornenyl group to be ~70 $Å^3$ through geometric calculations based on crystallographic data from representative molecular fragments.[50,51] On the basis of 5 different films measured at 3 different locations each, the film thickness is increased by 1.7 ± 0.3 Å after the exposure to $NB(COCl)_2$, corresponding to 2.7 ± 0.4 norbornenyl groups/nm^2. This average compares favorably with 1.8 ± 0.2 norbornenyl groups/nm^2 for the packing of norbornenyl groups tethered to the surface of Si nanoparticles reported by Jordi and Seery.[24]

Upon exposure of the norbornenyl decorated surface to Grubbs first generation catalyst, the film thickness is increased by 5.8 ± 2.8 Å, again based of 5 different films measured at 3 different locations each. The added volume of the Grubbs catalyst is approximately 570 $Å^3$ as determined by geometric calculations based on crystallographic data.[52] The density of catalyst on the substrate surface (1.0 ± 0.5 groups/nm^2) was determined as the ratio of the thickness of the adsorbed layer to the volume of the catalyst.

Immersion of the catalyst-coated substrate in a solution of 1.0 M norbornene in toluene for 15 min results in a 61 nm thick, surface-tethered film of ROMP-type polynorbornene. Surface-initiated polynorbornene films have been previously characterized by us[31] and others.[21,53] We will only highlight physical and chemical properties of polynorbornene relevant to this study. The advancing water contact angle ($\theta_A(H_2O) \sim 101^\circ$) is consistent with a hydrocarbon surface.[31,45] The RAIRS spectra of

polynorbornene (Figure 5.3) clearly shows crisp and intense asymmetric and symmetric CH_2 (2948 cm^{-1} and 2866 cm^{-1}) and CH stretching (2911 cm^{-1}) peaks. The position of the CH_2 scissoring peak (~1450 cm^{-1}) is indicative of purely cyclic CH_2 functionality.[54] The olefin functionality is observed in the trans C=CH out of plane bending[34,54] peak (968 cm^{-1}).

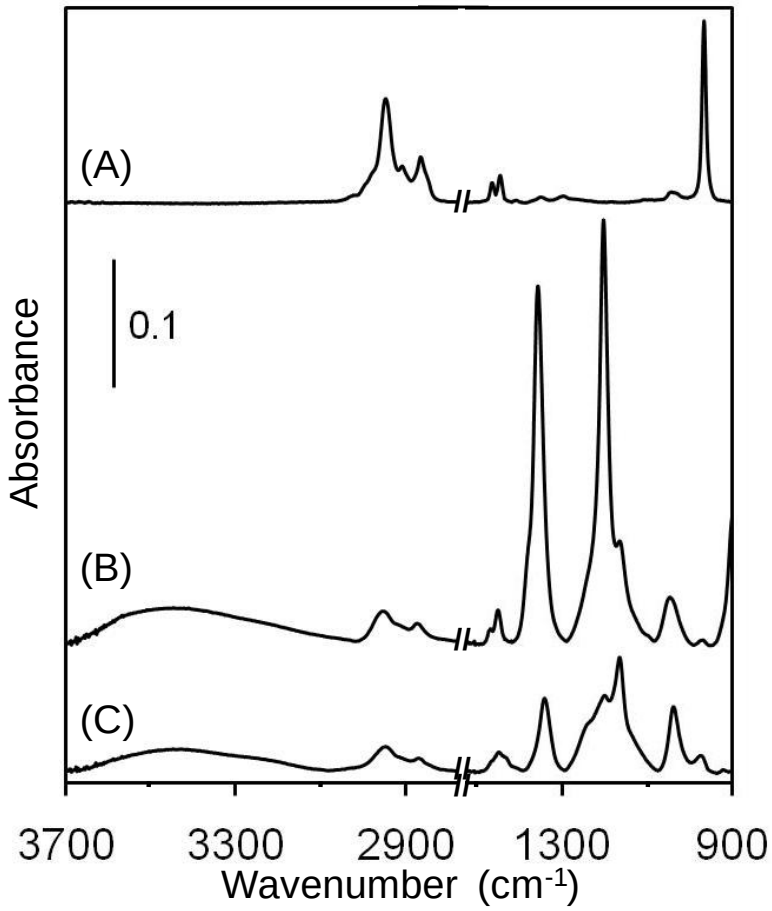

Figure 5.3. Reflectance-absorption infrared spectra of surface-initiated polynorbornene (A) and sulfonated polynorbornene before (B) and after (C) a 30 min exposure to DMSO. The spectra have been offset vertically for clarity.

Sulfonation of Polynorbornene

Upon subsequent exposure of the pNB film to 0.1 M acetyl sulfate for 1 min and to DMSO for 30 min (Figure 5.3 A and C), the RAIR spectrum indicates ~95% reduction of the trans C=CH out of plane bending peak (968 cm^{-1}) and reduction of all peaks associated with olefin functionality. The introduction of protonated sulfonate functionality is observed through the appearance of asymmetric and symmetric SO_3 stretching (~1343 and ~1167 cm^{-1}, respectively) and S-OH stretching (923 cm^{-1}) modes.[34,54,55] The corresponding asymmetric and symmetric SO_3 stretching modes for the deprotonated species are also observed in the sulfonated spectra at ~1201 and ~1040 cm^{-1}, respectively.[56] The C=CH out of plane bending peak at 810 cm^{-1} associated with the olefinic sulfonate product[34] is not present indicating the preferential formation of the hydroxysulfonate product. The introduction of the hydroxyl functionality, observed as a broad peak from 3700 to 3100 cm^{-1}, is further evidence of the hydroxysulfonate product. The decrease in olefin functionality coupled with an increase in all modes associated with sulfonate and alcohol functionality is consistent with the conversion of the olefin to the hydroxysulfonate product. The position of the CH_2 scissoring peak (~1450 cm^{-1}) is indicative of the conservation of the cyclic CH_2 functionality after sulfonation.[54] The crisp asymmetric and symmetric CH_2 (2948 cm^{-1} and 2866 cm^{-1}) and CH stretching (2911 cm^{-1}) peaks of the pNB spectrum[21] are reduced and distorted upon sulfonation. While it is common for the intensities[21,57] and positions[58] of peaks in the RAIR spectrum to be altered as the chains reorganize, the complimentary decrease in ellipsometric film thickness during sulfonation from 120 nm to 71 nm indicates a ~41% loss of polymer chains from the film.

Literature provides no record of or mechanism for chain scission at the olefin site during sulfonation.[32-35,39] To test if sulfonation was causing chain scission, the same procedure was performed without a sulfonating agent (acetyl sulfate) as a blank control. Film thicknesses of the polymer samples decreased 34 ± 22 % during the blank controls to indicate that the majority of film loss, if not all, is independent of exposure to acetyl sulfate. To test if the film was being cleaved at the thiolate linkage to the Au substrate, polymer was grown from a silicon surface using a more stable 7-octenyl trichlorosilane linkage and exposed to dichloromethane. Film thicknesses on the silane bound polymer films decreased 45 ± 13 % to indicate the film loss is also independent of the polymer / substrate linkage. There are several mechanisms for cleavage of the polynorbornene prior to sulfonation including secondary metathesis.[24,31,59] Secondary metathesis refers to the reaction of the metathesis catalyst with the olefin functionality in the repeat unit of a ROMP-type polymer, cleaving the polymer chain.[59] Exposure of the films to ethyl vinyl ether, an agent used to terminate the catalytic activity in Grubbs catalyst, resulted in no reduction in ellipsometric film loss (44 ± 17%), suggesting secondary metathesis is not the primary mechanism for film loss. Since the controls indicate the film loss is not due to the sulfonation agent, the polymer/substrate linkage, or secondary metathesis activity, it is likely the film loss occurs at the olefin site in the polymer backbone prior to sulfonation and the cleaved chain fragments are rinsed away during subsequent processing.

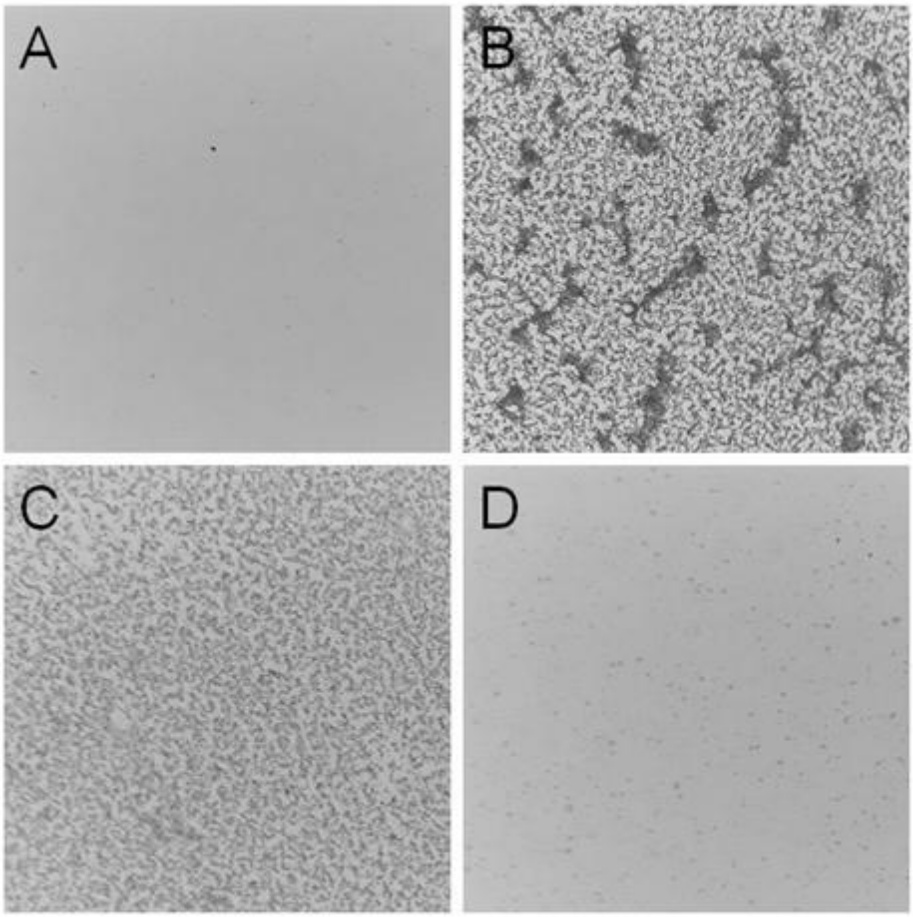

Figure 5.4. Optical Microscope images (250 μm x 250 μm) of surface-initiated polynorbornene before sulfonation (A), after sulfonation (B), and sulfonated polynorbornene after 5 min (C) and 30 min (D) exposure to DMSO.

Inspection of the polynorbornene films immediately after exposure to acetyl sulfate through optical microscopy (Figure 5.4B) reveals a non-uniform surface with polymer aggregates. These aggregates were shown via atomic force microscopy to be in excess of 500 nm tall. This unique surface morphology is a result of the contrasting solvation behavior of polynorbornene and sulfonated polynorbornene. During sulfonation, the polynorbornene chains are well solvated and likely stretched away from the substrate in dicholoromethane,[32,60] but the sulfonation product is not well solvated in dichloromethane.[32] As the reaction proceeds, the sulfonated polynorbornene forms

clusters to minimize polymer-solvent interactions, resulting in a highly non-uniform surface morphology. Through exposure to DMSO, a good solvent for sulfonated polynorbornenes,[32] the polymer chains relax into a less constrained conformation, providing a more uniform surface morphology (Figure 5.4 C and D). As the polymer relaxes, the average orientation of the backbone becomes less normal to the surface, and the average orientation of the sulfonate groups becomes more normal to the surface. This shift in orientation results in the SO_3 asymmetric stretching being less aligned with the RAIR induced electric field normal to the surface. As a result, the relaxation of the sulfonated ionomer film is observed in the RAIR spectra (Figure 5.3 B and C) through diminution of the asymmetric SO_3 stretching modes of the protonated and deprotonated state (1343 and 1201 cm^{-1}, respectively). Most importantly, the exposure of the sulfonated films to DMSO resulted in no reduction in symmetric SO_3 stretching modes (1167 and 1040 cm^{-1}) or CH stretching modes (2800 - 3000 cm^{-1}), indicating the stability of the sulfonated film due to the persistence of the SAM-based linkage of the film to the gold surface.

Proton Conduction in Sulfonated Polynorbornene Films

We used electrochemical impedance spectroscopy (EIS) with a 0.1 M sulfuric acid (aq) electrolyte solution to probe the resistance of the polymer films against proton transport. Characteristic impedance spectra in the form of Bode plots for the gold-coated substrate, the NB-decorated monolayer (initiator), a ~120 nm polynorbornene film, and a ~71 nm sulfonated polynorbornene film after a 30 min exposure to DMSO are shown in Figure 5.5. Values of film resistance (R_f) and interfacial capacitance (C_i) were

determined by fits to equivalent circuit models (Figure 3.1 D and E) and are provided in Table 5.2.

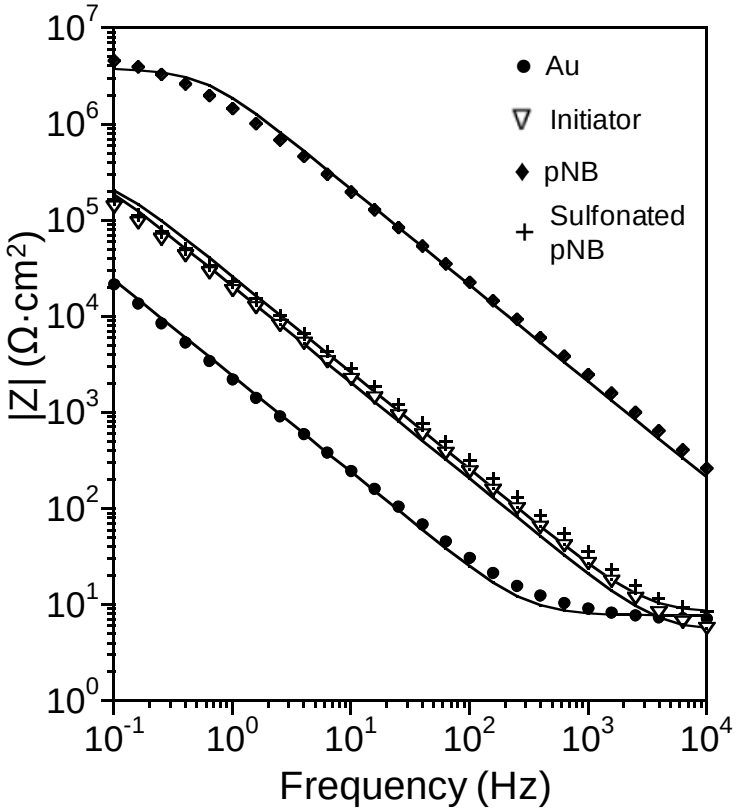

Figure 5.5. Electrochemical impedance spectra obtained in 0.1 M H_2SO_4 (aq) for the indicated films on gold. Solid curves represent fits of the data using appropriate equivalent circuit models.

Table 5.2. Film Resistance and Interfacial Capacitance for Indicated Films

Film	$\log(R_f)$ ($\Omega \cdot cm^2$)	C_i (μF)
bare gold	[a]	63.4 ± 3.6
NB decorated SAM	[a]	7.3 ± 1.1
pNB	6.5 ± 0.8	[b]
sulfonated pNB	0.21 ± 0.11	6.6 ± 0.7

[a] These systems are not modeled with a film resistance (see Figure 3.1 D)[61]
[b] beyond measurable range of instrument

In Chapter IV, we showed that surface-initiated polynorbornene films have a resistance to the transport of $K_3Fe(CN)_6$ and $K_4Fe(CN)_6$ redox probes that is comparable to that of other surface-initiated hydrocarbon films.[31] Similarly, surface-initiated polynorbornene films also offer an excellent resistance against proton transport ($R_f \sim 10^{6.5}$ $\Omega \cdot cm^2$). The polynorbornene film is the only film studied here in which the film resistance is sufficiently high to ascertain the film capacitance ($C_f = 110 \pm 50$ nF), which is comparable to values reported previously for polynorbornene in alternate electrolytes.[31] The charge separation at the gold / organic interface results in an interfacial capacitance. This capacitance probes the nature of the gold / organic interface and remains largely unchanged by the film growth and sulfonation procedure. The interfacial capacitance is comparable for the initiator ($C_f \sim 7.3$ μF) and sulfonated polynorbornene ($C_f \sim 6.6$ μF). The interfacial capacitance of the surface-initiated polynorbornene film is obscured in the available frequency range by the large impedance due to the film.

Upon sulfonation and exposure to DMSO, the film resistance drops by over 5 orders of magnitude to 1.6 $\Omega \cdot cm^2$. The film resistance of the sulfonated film is comparable to that of the solution resistance measured for the norbornenyl-decorated SAM and for bare gold (~ 6.9 $\Omega \cdot cm^2$). Exposure of the sulfonated polynorbornene to DMSO has a negligible effect on the impedance properties of the film. The low resistance to proton transfer in the sulfonated polynorbornene is encouraging for future investigation into these ionomer-modified interfaces.

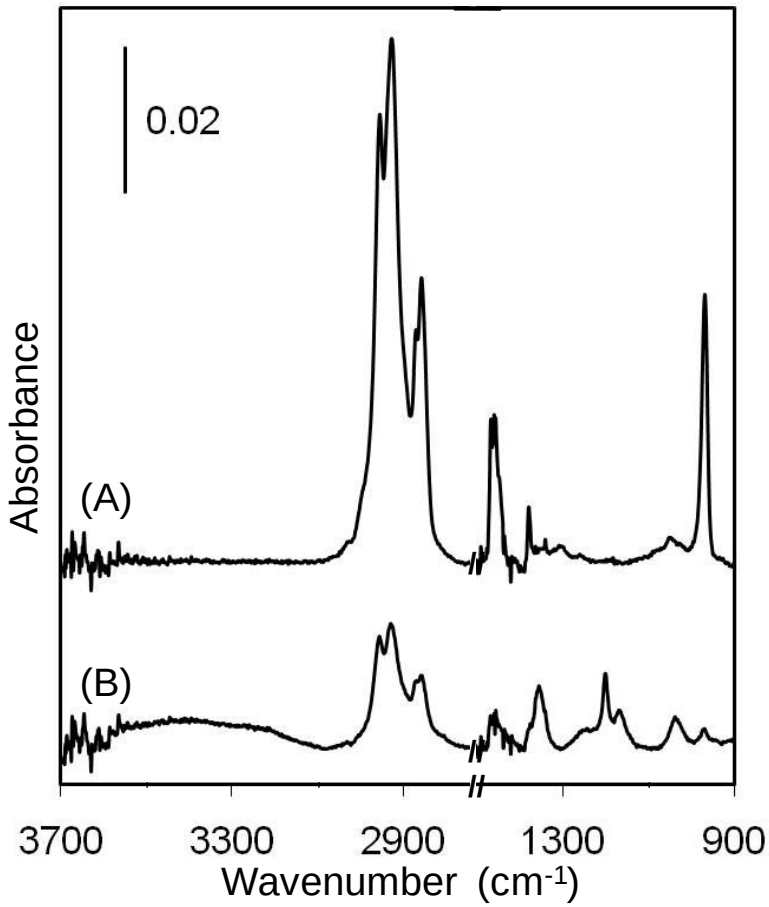

Figure 5.6. Reflectance-absorption infrared spectra of surface-initiated poly(n-butylnorbornene) before (A) and after sulfonation (B). The spectra have been offset vertically for clarity.

Sulfonation of Poly(n-butylnorbornene)

To demonstrate the versatility of this approach toward sulfonated films, we prepared and sulfonated surface-initiated poly(butylnorbornene) in a manner analogous to that of the polynorbornene films. These films were also exposed to DMSO for 30 min, in a manner consistent with polynorbornene samples. The reaction of poly(butylnorbornene) with acetyl sulfate was monitored via RAIRS (Figure 5.6). The spectrum of poly(butylnorbornene) is thoroughly described in our previous work.[31] Exposure to acetyl sulfate reduced the peak area corresponding to trans C=CH out of

plane bending (968 cm^{-1}) over 96%. Asymmetric and symmetric SO_3 stretching peaks at 1355 and 1168 cm^{-1}, respectively, indicate the additional sulfonate functionality.[34,54,55] The corresponding asymmetric and symmetric stretching modes for the deprotonated species are ~1200 and ~1038 cm^{-1}, respectively.[56] The C=CH out of plane bending peak at 810 cm^{-1} associated with the olefinic sulfonate product[34] is not present indicating the preferential formation of the hydroxysulfonate product. The cyclic and linear CH_2 stretching modes are reduced and shifted 1-2 cm^{-1} towards higher wavenumbers, indicative of a disruption of the original methylene packing.[42] The sulfonation of poly(butylnorbornene) exhibits similar film loss to that observed in the polynorbornene system. The ratio of total methylene functionality (3000-2800 cm^{-1}) to sulfonate functionality is higher in the sulfonated poly(butylnorbornene) films than the sulfonated polynorbornene films due to in additional butyl side chain. Sulfonated poly(butylnorbornene) films exhibit a higher surface energy ($\theta_A(H_2O) = 95 \pm 2^\circ$) than that of the poly(butylnorbornene) film ($\theta_A(H_2O) = 109 \pm 2^\circ$). The additional butyl functionality increases the advancing contact angle for sulfonated poly(butylnorbornene) beyond that of sulfonated polynorbornene ($\theta_A(H_2O) \sim 75^\circ$). The exceptionally high contact angle hysteresis in the sulfonated poly(butylnorbornene) film ($\theta_A - \theta_R > 85^\circ$) is consistent with that of a chemically heterogeneous surface.[62]

Conclusions

Surface-tethered sulfonated polymer films are easily prepared through the exposure of excess acetyl sulfate to surface-initiated polynorbornene films. The

sulfonated films are thinner than their polynorbornene precursors, due to some chain loss that is independent of the sulfonation reagent and likely occurs at the olefin site in the chain backbone. Sulfonation of surface-initiated polynorbornene results in a highly non-uniform surface morphology which can be relaxed to a more uniform surface through exposure to DMSO. Sulfonated polynorbornene films have an intermediate surface energy, and the film resistance to proton transfer due to the sulfonated polymer is very small. The ability to generate sulfonated films from functional polynorbornenes is demonstrated through the sulfonation of poly(butylnorbornene). We have highlighted a novel approach towards a norbornenyl-decorated SAM for the immobilization of a metathesis catalyst on a surface. The ability to create uniform sulfonated films on complex geometries has potential application in high surface area electrode assemblies, which we will highlight in Chapter VI.

References

1. Carrette, L.; Friedrich, K. A.; Stimming, U. *ChemPhysChem* **2000,** 1, 162-193.

2. Iojoiu, C.; Marechal, M.; Chabert, F.; Sanchez, J. Y. *Fuel Cells* **2005,** 5, (3), 344-354.

3. Jinnouchi, R.; Okazaki, K. *J. Electrochemical Soc.* **2003,** 150, E66-E73.

4. Roziere, J.; Jones, D. J. *Annu. Rev. Mater. Res.* **2003,** 33, 503-555.

5. Saito, M.; Arimura, N.; Hayamizu, K.; Okada, T. *J. Phys. Chem. B* **2004,** 108, 16064-16070.

6. Carrette, L.; Friedrich, K. A.; Stimming, U. *Chemphyschem* **2000,** 1, (4), 162-193.

7. Middelman, E. *Fuel Cells Bulletin* **2002**, (11), 9-12.

8. Litster, S.; McLean, G. *Journal of Power Sources* **2004,** 130, (1-2), 61-76.

9. Cha, S. W.; O'Hayre, R.; Prinz, F. B. *Solid State Ionics* **2004,** 175, (1-4), 789-795.

10. Cha, S. Y.; Lee, W. M. *J. Electrochem. Soc.* **1999,** 146, 4055-4060.

11. Lux, K. W.; Rodriguez, K. J. *Nano Letters* **2006,** 6, (2), 288-295.

12. Zeis, R.; Mathur, A.; Fritz, G.; Lee, J.; Erlebacher, J. *Journal of Power Sources* **2007,** 165, (1), 65-72.

13. Hinkebein, T. E.; Price, M. K. *Desalination* **2005,** 182, (1-3), 19-28.

14. Nagarale, R. K.; Gohil, G. S.; Shahi, V. K. *Advances in Colloid and Interface Science* **2006,** 119, (2-3), 97-130.

15. Eckenrode, H. M.; Dai, H. L. *Langmuir* **2004,** 20, (21), 9202-9209.

16. Hesselink, F. T., *Adsorption form Solution at the Solid/Liquid Interface*. Academic Press Inc.: New York, 1983.

17. Ramstedt, M.; Cheng, N.; Azzaroni, O.; Mossialos, D.; Mathieu, H. J.; Huck, W. T. S. *Langmuir* **2007,** 23, (6), 3314-3321.

18. Jennings, G. K.; Brantley, E. L. *Adv. Mater.* **2004,** 16, 1983-1994.

19. Bantz, M. R.; Brantley, E. L.; Weinstein, R. D.; Moriarty, J.; Jennings, G. K. *Journal of Physical Chemistry B* **2004,** 108, (28), 9787-9794.

20. Kim, J.-B.; Huang, W.; Bruening, M. L.; Baker, G. L. *Macromolecules* **2002,** 35, 5410-5416.

21. Kim, N. Y.; Jeon, N. L.; Choi, I. S.; Takami, S.; Harada, Y.; Finnie, K. R.; Girolami, G. S.; Nuzzo, R. G.; Whitesides, G. M.; Laibinis, P. E. *Macromolecules* **2000,** 33, 2793-2795.

22. Matyjaszewski, K.; Miller, P. J.; Shukla, N.; Immaraporn, B.; Gelman, A.; Luokala, B. B.; Siclovan, T. M.; Kickelbick, G.; Vallant, T.; Hoffmann, H.; Pakula, T. *Macromolecules* **1999,** 32, (26), 8716-8724.

23. Bai, D.; Hardwick, C. L.; Berron, B. J.; Jennings, G. K. *Journal of Physical Chemistry B* **2007,** 111, (39), 11400-11406.

24. Jordi, M. A.; Seery, T. A. P. *J. Am. Chem. Soc.* **2005,** 127, (12), 4416-4422.

25. Watson, K. J.; Zhu, J.; Nguyen, S. T.; Mirkin, C. A. *Journal of the American Chemical Society* **1999,** 121, (2), 462-463.

26. Harada, Y.; Girolami, G. S.; Nuzzo, R. G. *Langmuir* **2003,** 19, (12), 5104-5114.

27. Liu, X. G.; Guo, S. W.; Mirkin, C. A. *Angew. Chem. Int. Ed.* **2003,** 42, (39), 4785-4789.

28. Lee, W. K.; Caster, K. C.; Kim, J.; Zauscher, S. *Small* **2006,** 2, (7), 848-853.

29. Voronov, A.; Shafranska, O. *Langmuir* **2002,** 18, (11), 4471-4477.

30. Husseman, M.; Malmstrom, E. E.; McNamara, M.; Mate, M.; Mecerreyes, D.; Benoit, D. G.; Hedrick, J. L.; Mansky, P.; Huang, E.; Russell, T. P.; Hawker, C. J. *Macromolecules* **1999,** 32, (5), 1424-1431.

31. Berron, B. J.; Graybill, E. P.; Jennings, G. K. *Langmuir* **2007,** 23, (23), 11651-11655.

32. Boyd, T. J.; Schrock, R. R. *Macromolecules* **1999,** 32, (20), 6608-6618.

33. Gilbert, E. E., *Sulfonation and Related Reactions*. John Wiley & Sons, Inc.: New York, 1965.

34. Planche, J. P.; Revillon, A.; Guyot, A. *Journal of Polymer Science Part a-Polymer Chemistry* **1988,** 26, (2), 429-444.

35. Planche, J. P.; Revillon, A.; Guyot, A. *Journal of Polymer Science Part a-Polymer Chemistry* **1990,** 28, (6), 1377-1386.

36. Hofmann, K.; Simchen, G. *Synthesis-Stuttgart* **1979**, (9), 699-700.

37. Wuts, P. G. M.; Wilson, K. E. *Synthesis-Stuttgart* **1998**, (11), 1593-1595.

38. Tran, Y.; Auroy, P. *Journal of the American Chemical Society* **2001,** 123, (16), 3644-3654.

39. Bakker, B. H.; Cerfontain, H. *European Journal of Organic Chemistry* **1999**, (1), 91-96.

40. Bai, D. S.; Habersberger, B. M.; Jennings, G. K. *J. Am. Chem. Soc.* **2005,** 127, (47), 16486-16493.

41. Tsukamoto, K.; Kubo, T.; Nozoye, H. *Applied Surface Science* **2005,** 244, (1-4), 578-583.

42. Berron, B.; Jennings, G. K. *Langmuir* **2006,** 22, 7235-7240.

43. Porter, M. D.; Bright, T. B.; Allara, D. L.; Chidsey, C. E. D. *Journal of the American Chemical Society* **1987,** 109, (12), 3559-3568.

44. Bain, C. D.; Troughton, E. B.; Tao, Y. T.; Evall, J.; Whitesides, G. M.; Nuzzo, R. G. *Journal of the American Chemical Society* **1989,** 111, (1), 321-335.

45. Laibinis, P. E.; Palmer, B. J.; Lee, S.-W.; Jennings, G. K., The Synthesis of Organothiols and their Assembly into Monolayers on Gold. In *Thin Films*, Ulman, A., Ed. Academic Press: Boston, 1998; Vol. 24, pp 1-41.

46. Bai, D.; Jennings, G. K. *Journal of the American Chemical Society* **2005,** 127, (9), 3048-3056.

47. Bai, D. S.; Elliott, S. M.; Jennings, G. K. *Chemistry of Materials* **2006,** 18, (22), 5167-5169.

48. Park, J. S.; Vo, A. N.; Barriet, D.; Shon, Y. S.; Lee, T. R. *Langmuir* **2005,** 21, (7), 2902-2911.

49. Shon, Y. S.; Lee, T. R. *Journal of Physical Chemistry B* **2000,** 104, (34), 8192-8200.

50. Doms, L.; Vanhemelrijk, D.; Vandemieroop, W.; Lenstra, A. T. H.; Geise, H. J. *Acta Crystallographica Section B-Structural Science* **1985,** 41, (AUG), 270-274.

51. Jones, P. G.; Kirby, A. J.; Parker, J. K. *Acta Crystallographica Section C-Crystal Structure Communications* **1992,** 48, 847-849.

52. Schwab, P.; France, M. B.; Ziller, J. W.; Grubbs, R. H. *Angewandte Chemie-International Edition in English* **1995,** 34, (18), 2039-2041.

53. Rutenberg, I. M.; Scherman, O. A.; Grubbs, R. H.; Jiang, W.; Garfunkel, E.; Bao, Z. *J. Am. Chem. Soc.* **2004,** 126, 4062-4063.

54. Silverstein, R.; Webster, F.; Kiemle, D., *Spectrometric Identification of Organic Compounds*. 7 ed.; John Wiley & Sons, Inc.: New Jersey, 2005.

55. Langner, R.; Zundel, G. *Journal of Physical Chemistry* **1995,** 99, (32), 12214-12219.

56. Bellamy, L. J., The Infrared Spectra of Organo Sulfur Compounds. In *Organic Sulfur Compounds*, Kharasch, N., Ed. Pergamon Press: New York, 1961.

57. Nuzzo, R. G.; Dubois, L. H.; Allara, D. L. *Journal of the American Chemical Society* **1990,** 112, (2), 558-569.

58. Weinstein, R. D.; Moriarty, J.; Cushnie, E.; Colorado, R.; Lee, T. R.; Patel, M.; Alesi, W. R.; Jennings, G. K. *Journal of Physical Chemistry B* **2003,** 107, (42), 11626-11632.

59. Lynn, D. M.; Kanaoka, S.; Grubbs, R. H. *Journal of the American Chemical Society* **1996,** 118, (4), 784-790.

60. Bielawski, C. W.; Grubbs, R. H. *Macromolecules* **2001,** 34, (26), 8838-8840.

61. Nahir, T. M.; Bowden, E. F. *Electrochimica Acta* **1994,** 39, (16), 2347-2352.

62. Long, J.; Hyder, M. N.; Huang, R. Y. M.; Chen, P. *Advances in Colloid and Interface Science* **2005,** 118, (1-3), 173-190.

CHAPTER VI

ENABLING TECHNOLOGIES FOR HIGH SURFACE AREA ELECTRODES

Introduction

Since the power output of fuel cells is proportional to the electrochemically active catalyst surface area, the use of high surface area nanoporous electrodes and materials is an attractive approach to increase the power output of these electrochemical systems.[1] The use of submicrometer dimensions in carbon supports also provides short transport distances which lead to a higher utilization of Pt catalyst.[2,3] Both Tanaka Kikinzoku International K.K. and Johnson Matthey have recently introduced high surface area carbon supports coated with Pt specifically for fuel cell use.[4] Incorporation of the ionomer into highly porous substrates remains a challenge in developing support architectures, as current ionomer deposition techniques are often unable to access the high fraction of catalyst surface area that is within small pores.[4,5]

Ideally, a nanoscale porous electrode would be uniformly coated by a thin, uniform layer of ionomer, which will provide proton transport functionality while not inhibiting transport from the gas feed to the catalytically active site (Figure 6.1). Experimentally, a uniform coating at low thicknesses is difficult to achieve through solution casting methods.[6] In a porous PEM fuel cell cathode, poor ionomer incorporation into the pores will lead to poor catalyst utilization due to a proton deficiency,[7] while excess ionomer in the pores will lead to poor catalyst utilization due to reduced oxygen transport.[3]

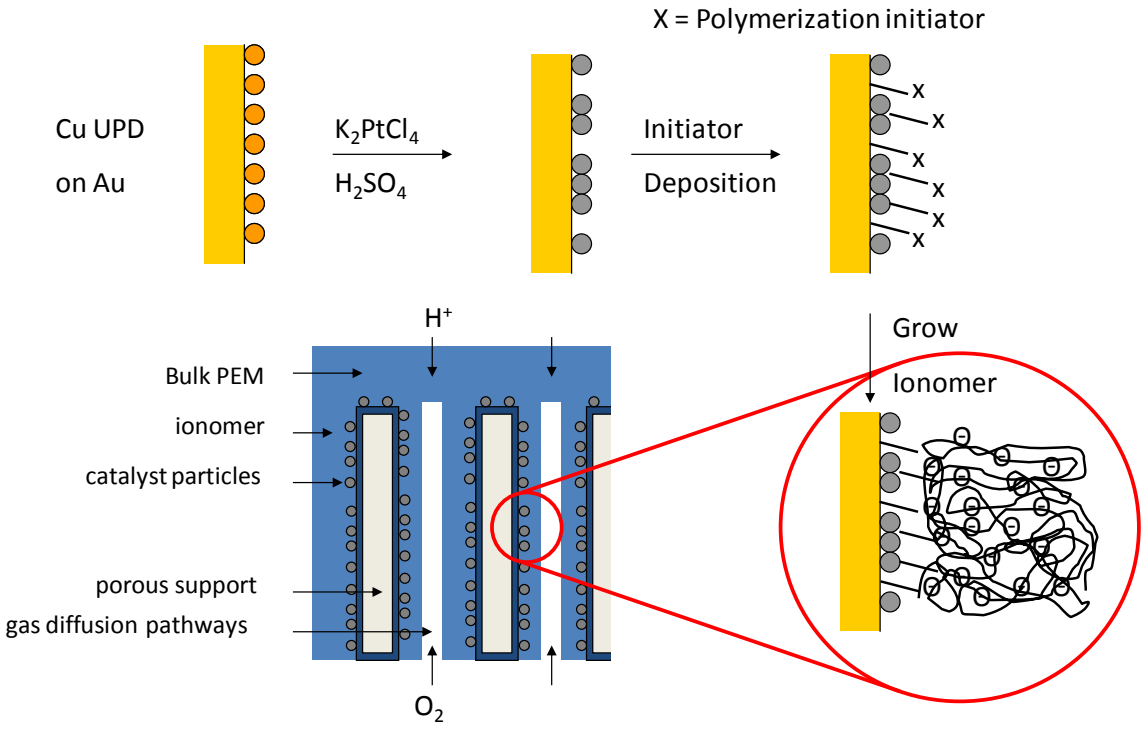

Figure 6.1. Schematic illustration of the deposition of catalyst and ionomer onto an idealized porous gold substrate.

Surface-initiated polymerization is a commonly used method for coating complex, three dimensional substrates.[5,6,8,9] In surface-initiated polymerization, the monomer reacts with a surface-tethered initiator or polymerization catalyst, resulting in the growth of a polymer chain from the surface. We employ the sulfonation of surface-initiated ring opening metathesis polymerization of polynorbornenes as a route towards a conformal coating of tunable thickness within the porous support structure (see Chapter V for details on sulfonated films).

In order to fully assess the performance of the ionomer coating, it must be evaluated in a catalytic electrode assembly. The deposition of platinum as an oxygen reduction reaction (ORR) catalyst is an essential step in the electrode assembly process.

The expense of platinum mandates sparse and controlled use both experimentally and in commercial applications. For maximum utilization of the Pt, a monolayer of Pt atoms on the support is desirable, allowing each Pt atom to be accessible by the reactants. Underpotential deposition (UPD) is a convenient way of electrochemically depositing a monolayer of atoms on surfaces of more noble electrode materials. The nobility of platinum excludes its deposition through UPD onto a gold surface. Nonetheless, Brankovic and Adzic developed a process of depositing adlayers of platinum onto gold surfaces through a two step process.[10] They utilize UPD to achieve sub-monolayer coverages of copper atoms onto the gold supports, and then electrolessly exchange the copper with platinum, thus immobilizing an adlayer of platinum on the gold surface. The planar arrangement of the platinum adlayer allows for nearly 100% utilization of the Pt catalyst. This platinum deposition approach has been previously exploited by Kongkanand and Kuwabata to deposit platinum monolayer islands onto Au(111) electrodes.[11] Platinum islands were deposited in void spaces created via the selective desorption of a thiolate species in a thiol-based mixed self-assembled monolayer. Through control of the monolayer composition, the platinum island size was varied, and a 5 to 10 nm Pt island was demonstrated as having the highest specific activity for oxygen reduction. While the formation of Pt islands allows for additional control over catalysis at the cathode, the additional processing steps required to form discrete islands are unattractive for our initial investigation into the utility of our ionomer system.

We will demonstrate this electrode assembly first on a planar gold support, and then on a high surface area, nanoporous gold support. Recent work by Erlebacher and coworkers has shown that dealloying gold leaf, a thin sheet of gold alloyed with silver, is

a simple and inexpensive route towards nanoporous gold supports.[12,13] Upon exposure to nitric acid, the silver is selectively etched and the gold remains as a nanoporous network. The pore size of these networks are tunable with varying etch times. Longer etching times allow the nanoporous gold structure to coarsen and larger void domains are created.

Experimental Section

Preparation of Nanoporous Gold Substrates

Gold mesh electrodes were prepared by a method similar to that of Erlebacher and coworkers.[12,13] Gold leaf was floated on deionized water, and then transferred to concentrated nitric acid with a microscope slide. The dealloyed gold sample was transferred to deionized water after 3 hours for neutralization. Distinct from Erlebacher's approach, a two-dimensional gold substrate was immersed in a 1.0 mM hexane-1,6-dithiol solution in ethanol overnight, producing a thiol-terminated monolayer. The thiol-terminated SAM-coated substrate is used to remove the dealloyed gold sample from the deionized water / air interface. The sample is allowed to dry into a stable nanoporous electrode film.

Polymerization

Gold substrates were placed in a 1.0 mM ethanolic solution of 4-mercapto-1-butanol for at least 60 min to yield a hydroxyl-terminated self-assembled monolayer. The samples were rinsed in ethanol and dried in a stream of nitrogen. Exposure of the SAM to a 5.0 mM solution of trans-3,6-endo-methylene-1,2,3,6-tetrahydrophthaloyl chloride in

dichloromethane for 30 min yields the acylation product of a surface tethered norbornenyl group. The samples were rinsed in ethanol and dried in a stream of nitrogen. The norbornenyl decorated substrates were exposed to a 5 mM solution of Grubbs catalyst in dichloromethane for 15 min. The catalyst-coated films were rinsed with dichloromethane and immediately placed in a monomer solution containing 1.0 M norbornene in toluene for 15 min to achieve ~60 nm polymer films. The films were sequentially rinsed with toluene, ethanol, and water and dried in a nitrogen stream.

Sulfonation

A 1.0 M acetyl sulfate solution in dichloromethane was prepared immediately prior to use similar to Tran et al.[14] Acetic anhydride (2.8 mL) was added to dichloromethane (14.0 mL) at 0˚C. Concentrated sulfuric acid (1.0 mL) was added dropwise to the acetic acid solution resulting in a 1.0 M acetyl sulfate solution in DCM. 1.0 mL of the 1.0 M acetyl sulfate solution was diluted to 0.1 M through the addition of 9.0 mL of dichloromethane at 0˚C. Polynorbornene coated substrates were exposed to the 0.1 M solution of acetyl sulfate for 60 s to yield a surface-tethered polynorbornene sulfonate coating. Samples were rinsed with dichloromethane and ethanol and dried in a nitrogen stream. The resulting polymer films were exposed to dimethyl sulfoxide (DMSO) for 30 min.

Copper and Platinum Deposition

Underpotential deposition of copper was performed with a Gamry Instruments CMS300 impedance system interfaced to a personal computer. Potentials were cycled at

20 mV/s between 500 and 50 mV vs $Cu^{0/1+}$ in 1.0 mM $CuSO_4$ in 0.1 M H_2SO_4 (aq, nitrogen saturated) using a polycrystalline gold coated counter electrode. After at least two cycles, the potential was held just negative of the UPD peak on the cathodic sweep, and the sample was removed from solution under potential control. Samples were rinsed in ethanol and dried in a nitrogen stream.

Copper-coated gold substrates were immediately placed in a nitrogen-saturated solution of 1.0 mM K_2PtCl_4 in 0.1 M H_2SO_4 (aq). After 5 min, samples were removed from solution, rinsed sequentially with water and ethanol and dried in a nitrogen stream.

Monitoring the Oxygen Reduction Reaction

The catalysis of the oxygen reduction reaction (ORR) was monitored via cyclic voltammetry (CV) with a Gamry Instruments CMS300 impedance system interfaced to a personal computer. ORR measurements were taken using a Ag/AgCl/saturated KCl reference electrode with a Pt mesh as the counter electrode in an oxygen saturated, aqueous solution of 0.1 M H_2SO_4. Samples were first cycled over potentials between 1000 and -200 mV vs. Ag/AgCl/saturated KCl to remove any remaining chloride from the electrode surface. Samples were then cycled at 50 mV/ s over potentials from 800 to 0 mV in an oxygen saturated H_2SO_4 aqueous solution. We define the onset potential as the potential of half the maximum current.

Results and Discussion

Planar Gold Electrode Assembly

We deposit a submonolayer of copper onto a polycrystalline gold-coated substrate via underpotential deposition (UPD).[15] Gold-coated substrates were exposed to an aqueous solution containing 1.0 mM copper sulfate and 0.1 M sulfuric acid, and the system potential was cycled between 500 and 50 mV vs. a copper wire reference in a specialized cell that only exposed 1.0 cm^2 of the electrode's geometric surface area (Figure 6.2). The position of the anodic Cu UPD peak (220 mV) and cathodic Cu UPD peak positions (170 mV) are consistent with previous reports,[15] and signify the stripping and deposition, respectively, of a submonolayer of copper on the gold surface.

On the cathodic sweep, the potential of the system was held just negative of the UPD peak (~100 mV), and the sample was emersed from the solution under constant potential. Polycrystalline gold substrates modified in this manner have been previously reported as having 55 ± 10 % coverage of copper atoms on polycrystalline gold substrates.[16] The presence of copper on the gold surface was confirmed through the copper $2p_{3/2}$ peak at 932 eV in the XPS spectra (Figure 6.3A). The shoulder on the Cu $2p_{3/2}$ peak extending towards higher binding energies is indicative of copper oxide species likely formed between the removal of the sample from the electrochemical cell and the introduction of the sample into the vacuum environment of the XPS system (~15 min).

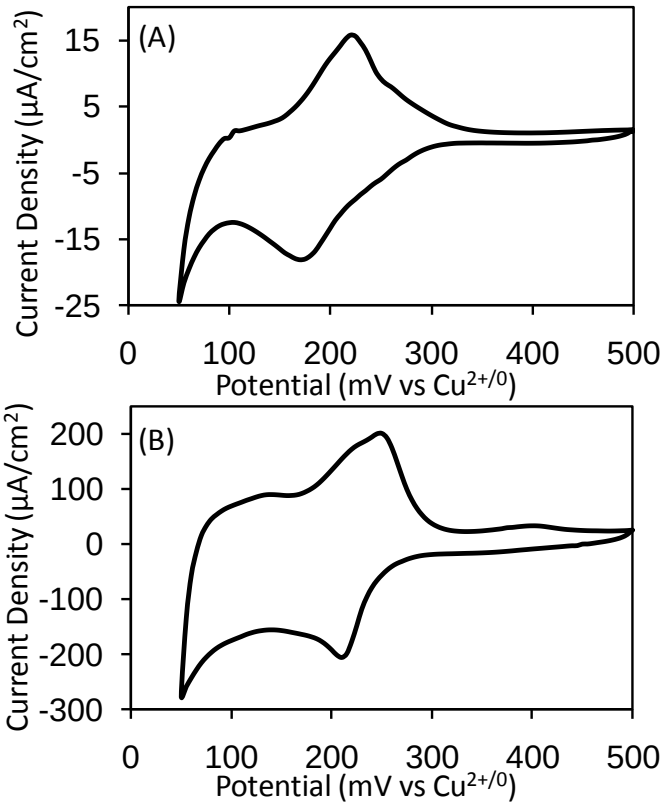

Figure 6.2. Cyclic voltammograms for planar gold coated substrates (A) and nanoporous gold structures (B) in 0.1 M H_2SO_4 and 1.0 mM $CuSO_4$ (aq). A flat cell was used to selectively expose 1.0 cm^2 of geometric surface area.

Copper coated samples were immediately placed in a solution of 1.0 mM K_2PtCl_4 in 0.1 H_2SO_4 (aq) for 5 min while the underpotentially deposited Cu layer was stoichiometrically exchanged with Pt. XPS spectra (Figure 6.3) show the complete diminution of Cu $2p_{3/2}$ peak at 932 eV and the introduction of the Pt $4f_{7/2}$ peak at 71.2 eV.[17,18] The replacement of copper with platinum has been previously demonstrated to occur at a 1:1 stoichiometry.[10] Assuming a 1:1 exchange, the original 55 ± 10 % coverage of copper would equate to an estimate of 64 ± 12 % surface coverage of platinum due to the larger atomic radius of platinum. This coverage estimate agrees well with the reported 70 ± 6 % coverage on a similarly prepared platinum coated substrate on

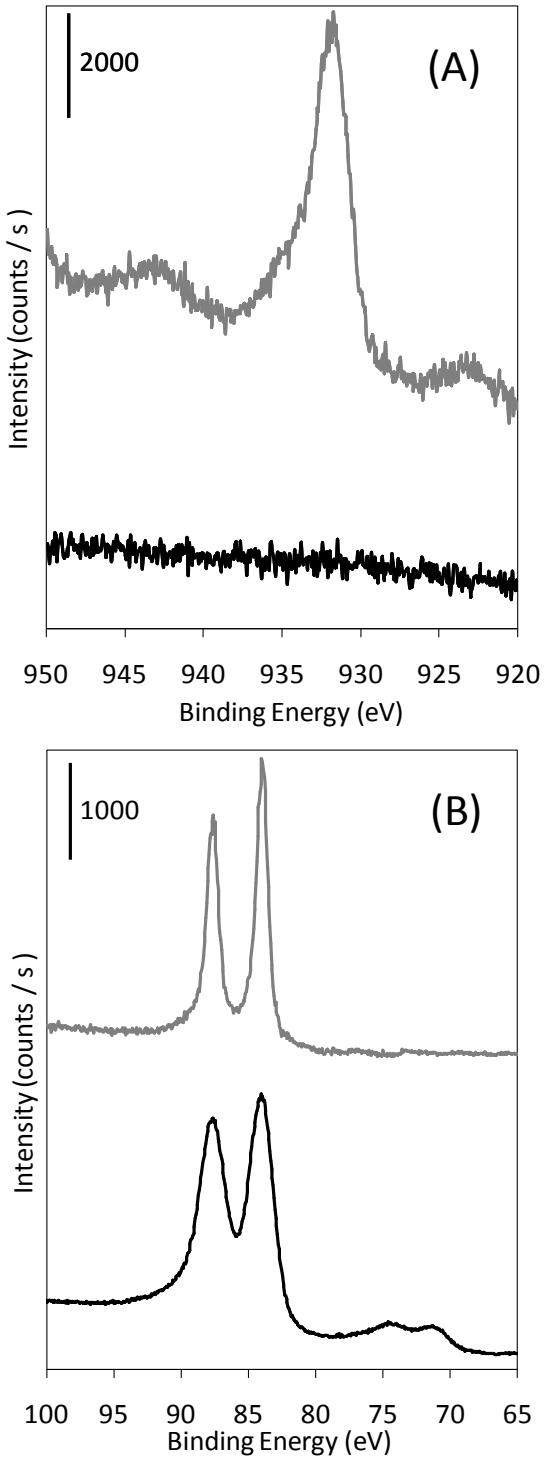

Figure 6.3. XPS spectra of gold-coated substrates after the underpotential deposition of copper (grey line) and after the subsequent exchange with platinum (black line). The spectra have been offset vertically for clarity.

a Au(111) surface.[11] This corresponds to a cathode catalyst loading of 0.14 μg/cm^2, a three order of magnitude reduction over conventional MEA cathode loadings of 0.5 mg/cm^2.[13]

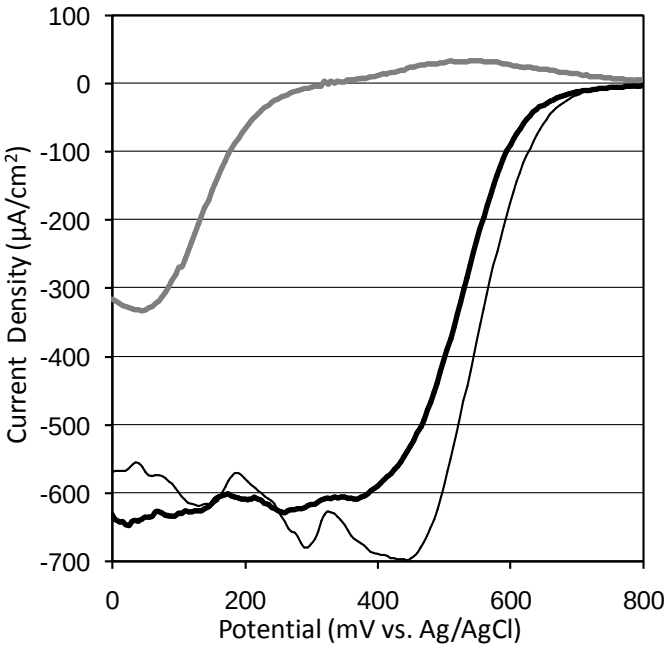

Figure 6.4. Representative potential sweeps of Pt coated planar gold substrates with (thick black) and without (thin black) a sulfonated pNB coating in O_2 saturated 0.1 M H_2SO_4 (aq). A cathodic sweep of unmodified planar gold substrates (grey) in O_2 saturated 0.1 M H_2SO_4 (aq) is given as reference.

Evaluation of ORR catalytic activity for this Pt/Au surface was monitored through cyclic voltammetry in an oxygen saturated 0.1 M H_2SO_4 (aq) solution. Samples were first electrochemically cleaned through potential sweeps between 1000 and -200 mV vs. Ag/AgCl/saturated KCl. Then ORR data for planar gold and platinum coated planar gold substrates and were collected between 800 and 0 mV vs. Ag/AgCl/saturated KCl and are shown in Figure 6.4. Consistent with previous reports,[11] the planar gold substrate exhibits poor ORR catalytic activity (330 μA/cm^2, 150 mV vs. Ag/AgCl). The addition

of a submonolayer of platinum on the planar gold substrate increases the reduction potential from 150 mV to 560 mV and doubles the maximum current density (700 $\mu A/cm^2$). Previously reported platinum monolayers deposited on Au(111) have similar ORR potentials (550 mV).[11]

After depositing a platinum submonolayer onto the planar gold substrate, we grow ~70 nm of polynorbornene sulfonate as an ionomer coating through the surface initiated growth of polynorbornene and subsequent sulfonation (discussed in detail in Chapter V). We have shown in Chapter V that surface-initiated sulfonated polynorbornene is a uniform, surface-tethered film. We also demonstrated through electrochemical impedance spectroscopy in 0.1 M H_2SO_4 (aq) that surface-initiated sulfonated polynorbornene has a low resistance to proton transport. Here, we have examined surface-initiated polynorbornene sulfonate as an ionomer coating for a fuel cell cathode by monitoring the oxygen reduction reaction. The addition of ~70 nm of sulfonated polynorbornene over the platinum-coated substrate resulted in a 6% decrease in ORR current density (660 $\mu A/cm^2$). While currents are comparable, the onset potential for ORR is 40 mV lower with the ionomer overlayer. While there is a low resistance to proton transport in sulfonated polynorbornene films, the transport of oxygen through these films has not been discussed. The permeability of oxygen in commercial ionomer membranes is lower than that of oxygen in water.[19] Furthermore, oxygen transport is believed to occur within hydrophobic domains formed through the self-organization of the ionomer upon exposure to water.[19] The large concentration of sulfonate groups and hydroxyl groups in sulfonated polynorbornene should cause the film to be so hydrophilic that it lacks hydrophobic domains.[20,21] Without hydrophobic domains, the oxygen

permeability in sulfonated polynorbornene is expected to be low. The lack of oxygen transport thought the ionomer would lower the reductive currents seen in ORR as well as the potential at which the reaction occurs, due to a deficiency of oxygen (the species to be reduced in equation 3-6).

Nanoporous Gold Electrode Assembly

We have used a nanoporous gold substrate to transfer technologies and concepts from a planar gold substrate to a three dimensional system without changing the surface chemistry of the system. As in the planar system, we use the underpotential deposition of copper as the first step in catalyst immobilization. The potential was cycled between 500 mV and 50 mV vs. a copper wire reference in a 1.0 mM $CuSO_4$ and 0.1 M H_2SO_4 aqueous solution. The potential was held at ~ 100 mV as the samples were emersed from solution. Figure 6.2 shows the underpotential deposition and removal of copper at the nanoporous gold substrate using a flat cell to selectively expose 1.0 cm^2 of geometric surface area. The anodic and cathodic copper UPD peak positions (250 mV and 210 mV, respectively) are higher than those observed in UPD onto planar substrates. A similar trend was observed in a more thorough study of the dependence of the silver UPD peak position on gold substrate feature size. Silver UPD peak positions were recorded on polycrystalline gold substrates and nanoporous gold substrates coarsened for times between 15 min and 3 h. We observed a systematic increase in Ag UPD peak potential with an increase in porosity (in order of increasing potential: Au(111),[22] polycrystalline planar gold, nanoporous gold coarsened 3h, 1 h, and 15 min). The shift towards higher UPD potentials for both copper and silver is indicative of a stronger bond between the

substrate and the adatom that results from a difference in the surface structure of the nanoporous gold substrate.

Since the current is proportional to the amount of copper deposited and removed, the ratio of the anodic UPD peak area of the nanoporous substrate to that of the same peak on the planar substrate corresponds to the ratio of the electrochemically active surface area in the nanoporous substrate to that on the planar substrate. The nanoporous gold substrate was found to have ~ 10 fold greater surface area than the planar substrate through comparison of the UPD peak areas.

Analogous to the planar system, the copper-coated gold samples were placed in a solution of 1.0 mM K_2PtCl_4 in 0.1 H_2SO_4 (aq) for 5 min to stoichiometrically exchange the underpotentially deposited Cu layer for a Pt adlayer. Zeis et al. have previously estimated the platinum loading of a monolayer of platinum coated nanoporous gold substrates to be 5.0 $\mu g/cm^2$,[13] equating to a 23 fold increase over a monolayer loading on a planar substrate (0.23 $\mu g/cm^2$). The lower surface area in our nanoporous gold substrate, as determined by UPD peak ratios, is attributed to a longer dealloying time which results in coarsening of the substrate.[12] We also note that the monolayer used to bond the nanoporous gold substrate to the planar support should prevent the deposition of catalyst onto the surface area of the planar support as well as the bottom surface of the nanoporous gold, rendering it virtually inactive to ORR.[11]

The resulting nanoporous gold supported Pt structure is catalytically active for ORR (Figure 6.5). The onset potential for Pt on the nanoporous support (590 mV) is comparable to that of the Pt on the planar gold structure (560 mV). While there is an increase in current density of 21% in the oxygen reduction reaction on platinum for the

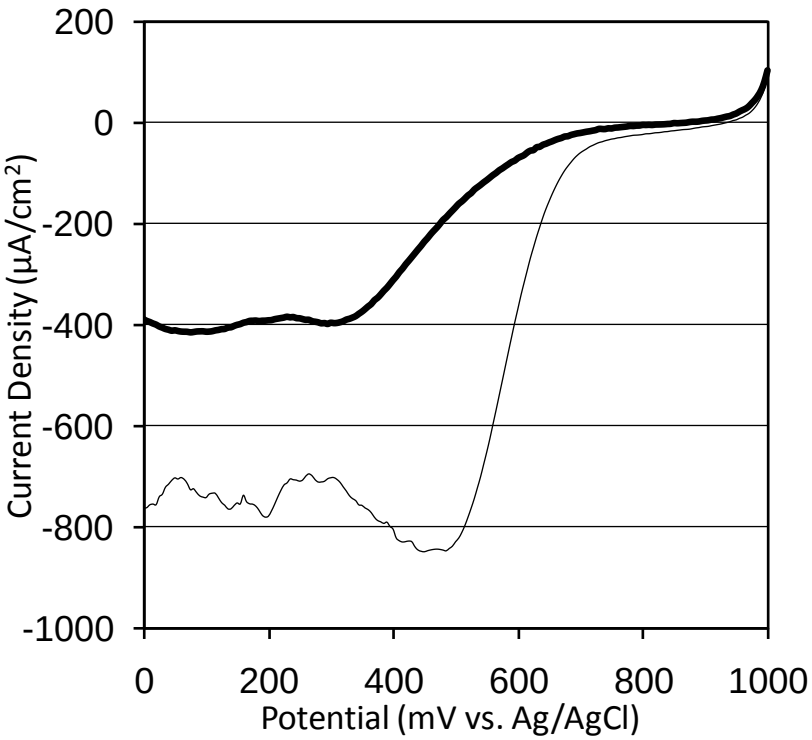

Figure 6.5. Representative potential sweeps of Pt-coated nanoporous gold substrates with (thick black) and without (thin black) a sulfonated pNB coating in O_2 saturated 0.1 M H_2SO_4 (aq).

3D system (850 μA/cm^2) over the planar system (700 μA/cm^2), the increase in current is not comparable to the ~10 fold increase in current seen in the UPD of copper onto the same substrates. The difference in the current density increase between the UPD and ORR is due to the transport of the consumed species. The Cu UPD system is not depleted of the reactive species (Cu^{2+}) during the experiment as the Cu^{2+} species is regenerated on the anodic sweep. In addition, the regeneration of the Cu^{2+} species at the site of consumption negates any diffusion limitations. In the ORR reaction, the oxygen in the aqueous electrolyte is quickly consumed through higher current densities than in UPD and must be replenished through a constant bubbling of oxygen. The transport of the

oxygen to the catalyst sites within the pores of the support is likely limited by the rapid consumption of the reactants at the outermost surface of the nanoporous support.

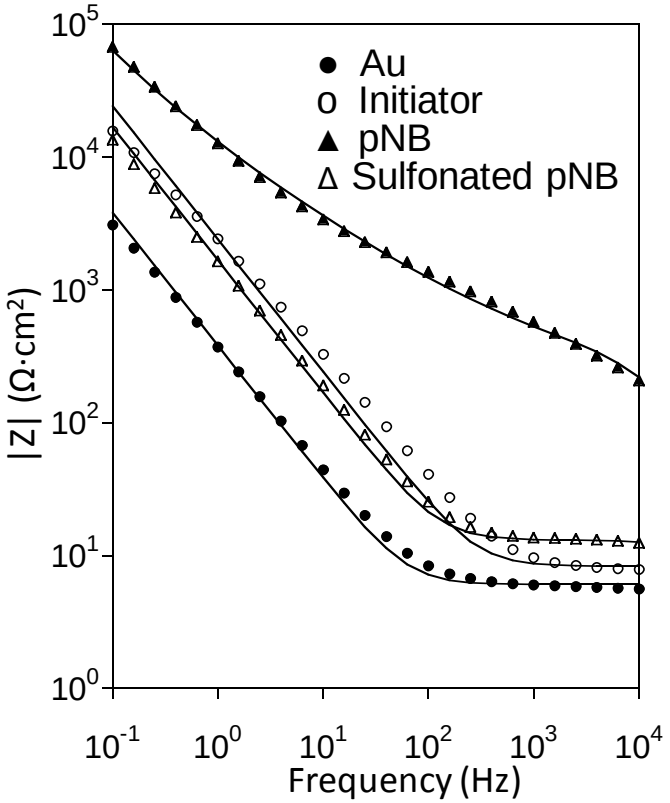

Figure 6.6. Electrochemical impedance spectra obtained in 0.1 M H_2SO_4 (aq) for the indicated films on the 3D gold substrate. Solid curves represent fits of the data using appropriate equivalent circuit models.

We used electrochemical impedance spectroscopy (EIS) in 0.1 M H_2SO_4 (aq) with a Ag/AgCl/saturated KCl reference electrode to probe the resistance to proton transfer of the polymer films grown from the nanoporous gold substrate (Figure 6.6). At high frequencies, the unsulfonated polynorbornene (pNB) film provides an additional 1.5 order of magnitude impedance to proton transport over that of the sulfonated polynorbornene film. The barrier properties of the unsulfonated film are markedly lower

on the nanoporous support than on the planar gold support, which may indicate regions of poor film coverage within the porous support. As observed in the EIS spectra for planar gold substrates, the sulfonated pNB film offers little resistance to proton transfer (4.3 $\Omega \cdot cm^2$). As in the planar substrate (see Chapter V), the interfacial capacitance of the sulfonated polynorbornene (98 μF) and the initiator layer (68 μF) are comparable, indicating a similar environment for both films at the gold/organic interface. The addition of the ionomer film to the nanoporous substrate decreases the current density to 420 $\mu A/cm^2$, a 51% decrease from that of the electrode without the ionomer film (Figure 6.5). As in the planar electrode, the onset potential and current density of the three-dimensional gold structure is likely limited by oxygen transport. Distinct to the nanoporous support, the sulfonated polynorbornene film will impede the oxygen transport not only through an additional resistance to oxygen transfer,[23] but also through a reduction of available space for solution phase oxygen diffusion by partially filling of the nanoporous support. A lack of oxygen would lower the oxygen reduction potential and decrease ORR currents (*vide infra*). In the future, this oxygen deficiency may be alleviated by using more hydrophobic, self-organizing ionomers and by lowering the thickness of the film to shorten the oxygen diffusion path. In addition, the future use of a testing apparatus which uses gaseous O_2 fed directly to the nanoporous electrode would be more consistent with the actual fuel cell environment and would alleviate O_2 transfer limitations of aqueous O_2 delivery. The incorporation of fluorinated ionomers as well as O_2-backfed electrochemical cells are described in detail in Chapter VIII.

Conclusions

A planar polycrystalline gold support was used to investigate the deposition of the catalyst and ionomer systems. A monolayer of platinum was deposited through electroless replacement of an underpotentially deposited submonolayer of copper atoms. The platinum deposited was catalytically active in the oxygen reduction reaction, as demonstrated through cyclic voltammetry. Deposition of the ionomer over the platinum-coated substrate left the underlying platinum catalytically active. We demonstrated the use of nanoporous gold as a catalyst support. We used underpotential deposition to demonstrate the nanoporous support had a 10-fold greater electrochemically active area at a constant geometric surface area. The platinum-coated nanoporous support allowed a 21% increase in ORR current density over that of the planar gold substrate. Oxygen transport due to ionomer flooding appears to lower ORR potentials and currents. Further refinements through ionomer design should lower oxygen transport limitations. We have demonstrated an effective method for modifying electrode interfaces with proton conducting films while preserving catalytic activity in both planar and nanoporous gold substrates.

References

1. Zhou, Z. L.; Dominey, R. N.; Rolland, J. P.; Maynor, B. W.; Pandya, A. A.; DeSimone, J. M. *Journal of the American Chemical Society* **2006,** 128, (39), 12963-12972.

2. Tang, J. M.; Jensen, K.; Waje, M.; Li, W.; Larsen, P.; Pauley, K.; Chen, Z.; Ramesh, P.; Itkis, M. E.; Yan, Y.; Haddon, R. C. *Journal of Physical Chemistry C* **2007,** 111, (48), 17901-17904.

3. Middelman, E. *Fuel Cells Bulletin* **2002**, (11), 9-12.

4. Janssen, G. J. M.; Sitters, E. F. *Journal of Power Sources* **2007,** 171, (1), 8-17.

5. Yang, Q.; Wang, L.; Xiang, W. D.; Zhou, J. F.; Tan, Q. H. *Journal of Polymer Science Part a-Polymer Chemistry* **2007,** 45, (15), 3451-3459.

6. Jennings, G. K.; Brantley, E. L. *Adv. Mater.* **2004,** 16, 1983-1994.

7. Mizuhata, H.; Nakao, S.; Yamaguchi, T. *Journal of Power Sources* **2004,** 138, (1-2), 25-30.

8. Jordi, M. A.; Seery, T. A. P. *J. Am. Chem. Soc.* **2005,** 127, (12), 4416-4422.

9. Buchmeiser, M. R., Metathesis polymerization to and from surfaces. In *Surface-Initiated Polymerization I*, 2006; Vol. 197, pp 137-171.

10. Brankovic, S. R.; Wang, J. X.; Adzic, R. R. *Surface Science* **2001,** 474, (1-3), L173-L179.

11. Kongkanand, A.; Kuwabata, S. *Journal of Physical Chemistry B* **2005,** 109, (49), 23190-23195.

12. Ding, Y.; Kim, Y. J.; Erlebacher, J. *Advanced Materials* **2004,** 16, (21), 1897-+.

13. Zeis, R.; Mathur, A.; Fritz, G.; Lee, J.; Erlebacher, J. *Journal of Power Sources* **2007,** 165, (1), 65-72.

14. Tran, Y.; Auroy, P. *Journal of the American Chemical Society* **2001,** 123, (16), 3644-3654.

15. Jennings, G. K.; Laibinis, P. E. *Journal of the American Chemical Society* **1997,** 119, (22), 5208-5214.

16. Jennings, G. K. Stability, Structure, and Barrier Properties of Self-Assembled Films on Metal Supports. Massachusetts Institute of Technology, Cambridge, MA, 1998.

17. Manolova, M.; Ivanova, V.; Kolb, D. M.; Boyen, H. G.; Ziemann, P.; Buttner, M.; Romanyuk, A.; Oelhafen, P. *Surface Science* **2005,** 590, (2-3), 146-153.

18. Mason, M. G. *Physical Review B* **1983,** 27, (2), 748-762.

19. Kocha, S. S.; Yang, J. D. L.; Yi, J. S. *Aiche Journal* **2006,** 52, (5), 1916-1925.

20. Mauritz, K. A.; Moore, R. B. *Chemical Reviews* **2004,** 104, (10), 4535-4585.

21. Gebel, G.; Moore, R. B. *Macromolecules* **2000,** 33, (13), 4850-4855.

22. Chen, C. H.; Vesecky, S. M.; Gewirth, A. A. *Journal of the American Chemical Society* **1992,** 114, (2), 451-458.

23. Ayad, A.; Bouet, J.; Fauvarque, J. F. *Journal of Power Sources* **2005,** 149, 66-71.

CHAPTER VII

LOOSELY-PACKED, HYDROXYL-TERMINATED SAMS ON GOLD

Introduction

In Chapter IV, we demonstrated the significant contribution of the self-assembled monolayer (SAM) in the overall resistance to transport of our surfaced-tethered films. The development of SAMs with diminished lateral packing density would allow us to decrease the impedance due to the polymer linkage to the underlying substrate and increase the overall efficiency of proton transport. In addition, loosely-packed SAMs allow for changes in molecular level conformation that are precluded in crystalline, densely packed monolayers. The additional freedom of chain motion within the SAM allows additional applications as biological interfaces[1] and as responsive films.[2] For example, some proteins adsorb with faster kinetics and have a higher steady-state surface concentration on loosely packed monolayers than on densely packed monolayers due to the unique conformation of the chains within the monolayer that allows partial penetration of the protein into the outer monolayer surface.[1,3] The use of spaced monolayers also allows for conformational changes within a film to create stimuli responsive interfaces.[2]

Several approaches have been used to prepare loosely packed monolayers. A common approach is to expose silicon oxide substrates to adsorbates containing trifunctional silane head groups for a short time. This method has been successful in creating SAMs with diminished packing or lateral packing gradients.[1,3,4] Unfortunately,

this method does not readily translate to SAMs prepared from thiols on gold as thiols will adsorb to form macroscopic islands of dense functionality at submonolayer coverages.[5,6] A similar approach is to coadsorb long and short chain thiols to prepare a mixed SAM, but this method has also been ineffective due to phase segregation of the adsorbates into macroscopic islands of common functionality.[7] The use of asymmetric disulfides with one long and one short chain is an approach which offers a variety of functionalities in a presumably well-mixed, 1:1 molar ratio.[8-11] However, conflicting evidence[7-13] exists regarding the extent of surface diffusion of these chains upon adsorption, allowing for nanoscopic phase segregation similar to that observed in the coadsorption of long and short chain thiolates. While significant surface diffusion is unlikely,[7-10] strong evidence supports preferential surface exchange that causes a disproportionate amount of the longer chained moiety to be present in the monolayer.[12] Lee and co-workers have synthesized chelating dithiols and trithiols that contain bulky head groups with short side chains. These adsorbates form well packed regions at the metal surface but leave loosely packed hydrocarbon chains exposed at the film surface.[14-17] These approaches have been effective in producing a loosely packed monolayer but are currently limited to methyl-terminated chains.[14-18]

Lahann et al.[2] have prepared loosely packed, carboxylate-terminated monolayers through a two-step process. First, they formed a SAM by adsorption of a thiol that contains a bulky, ester-linked triphenyl terminal group. Next, the terminal ester was hydrolyzed to produce a loose carboxyl-terminated monolayer. These loose SAMs resulted in a negatively charged interface that served as a model for an electrically

induced, reversibly switching surface. Applied potentials resulted in conformational changes which exposed different functionalities at the surface.

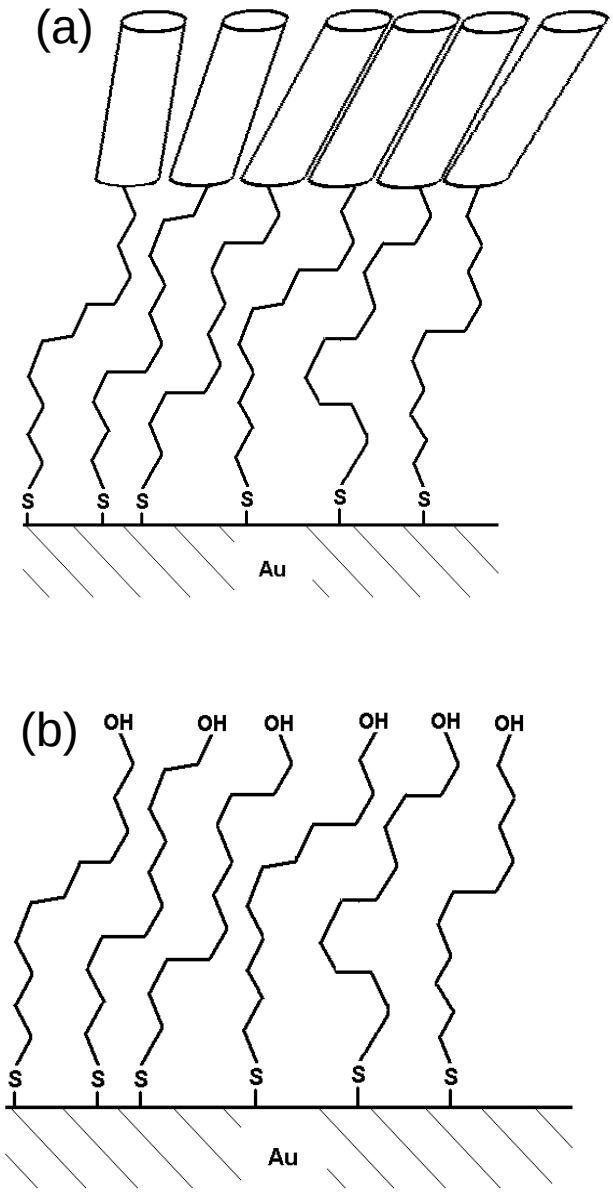

Figure 7.1. Schematic illustration of the possible arrangement of (a) -$SC_{11}O_2F_7$ and (b) loosely packed -$SC_{11}OH$ on gold substrates.

Here, we report the formation of hydroxyl-terminated self-assembled monolayers with diminished lateral packing density on gold surfaces. Our strategy is inspired by the

two-step approach of Lahann et al.[2] and prior work from Lee and co-workers[19] on the formation of SAMs from partially fluorinated alkanethiols. We begin by preparing a SAM from bis(11,11'-dithioundecyl) perfluoroheptanoate [$(S(CH_2)_{11}OC(O)(CF_2)_7F)_2$] where an undecyl tether is attached to a fluorocarbon tail group through an ester linkage. In an ideal case, the larger lateral dimension of the fluorocarbon helix (~5.6 Å)[20] dictates the chain structuring and forces the smaller alkyl chains (~4.6 Å)[21] into a less dense state. A previous AFM study estimates a chain packing of ~3.4 x 10^{14} chains cm^{-2} for a similar $Au/SC_{11}O_2F_9$ monolayer compared to ~4.6 x 10^{14} chains cm^{-2} for n-alkanethiolate SAMs, which translates to 35% greater lateral area occupied by the partially fluorinated chain.[22] These monolayers are stable at room temperature,[9] and the exposed fluorinated surface is low-energy to resist the adsorption of adventitious carbon**.** The fluorocarbon group can then be cleaved via base-mediated hydrolysis to yield a highly non-crystalline, hydroxyl-terminated monolayer (see Figure 7.1). We have demonstrated that this base-mediated hydrolysis rapidly reverts fluorinated ester groups back to alcohols in surface-initiated films of fluorocarbon-modified poly(hydroxyethyl methacrylate).[23] Our approach exploits the slow surface diffusion (~10^{-18} cm^2s^{-1})[24] for thiolates on gold to inhibit aggregation of the chains into densely packed domains.

Loosely packed, hydroxyl-terminated monolayers should have an intermediate surface energy due to exposure of methylene and hydroxyl functionality. These monolayers may be ideal for the adsorption of proteins such as Photosystem I, which preferentially adsorbs to surfaces of intermediate energy.[25] Other possibilities for loosely packed monolayers have yet to be investigated. As a potential use, conformational changes within a monolayer may facilitate surface reactions that would ordinarily be

sterically inhibited by a dense SAM. Schonherr and coworkers have shown the surface confinement of an ester linkage hinders the kinetics of hydrolysis.[26,27] A monolayer of adsorbates with more freedom of movement should also improve the kinetics of other surface reactions over a conformationally constrained adsorbate.

The loosely packed monolayer will contain significant interchain spacing for the penetration of water, ions, solvents, and other adsorbates. We discuss several examples of how this monolayer behaves in a manner consistent with that of a loosely packed monolayer.[16] Improved penetration of water, ions, and solvents into this loosely packed monolayer over densely packed monolayers is demonstrated through electrochemical impedance spectroscopy. We assess the unique exchange characteristics of these SAMs by exposing the monolayer to n-docosanethiol in THF and contrasting the results against those of well packed SAMs. The dynamics of surface bound thiolate exchange is of great importance in the design of functionalized alkanethiolate monolayer protected gold clusters.[28] Current thiolate exchange processes are kinetically localized to monolayer defect sites.[28-31] The development of monolayers with uniformly spaced packing may hold the key to a non-localized method of thiolate exchange and cluster functionalization.

Experimental Procedures

Synthesis of bis (11,11'-dithioundecyl) perfluoroheptanoate ($(SC_{11}O_2F_7)_2$ adsorbate)

Procedures followed to make bis (11-hydroxyundecyl) disulfide are similar to those reported by Shah et al.[32] Bis (11-hydroxyundecyl) disulfide (0.412 g, 1.01 mmol) and perfluorooctanoyl chloride (0.9744 g, 2.25 mmol) were added to dichloromethane

(15 mL) in a round bottom flask. The solution was stirred for 1 h at room temperature. Solvent was removed via rotary evaporation to yield a white solid. Approximately 8 mL of hexane at 35°C was added to solvate the solid. The solution was filtered, then chilled to -10°C. The remaining solution was decanted, and the white crystals were dried and weighed (1.098 g, 0.889 mmol; 87.8%). ^{1}H NMR (400 MHz, $CDCl_3$): δ = 1.3 (α-methylene, 28H), 1.65 (β-disulfide, 4H), 1.75 (β-ester, 4H), 2.68 (α-disulfide, 4H), 4.37 (α-ester, 4H).

Formation of SAMs

Au/$SC_{11}OH$ monolayers were prepared via immersion of gold substrates in a 0.5 mM bis (11-hydroxyundecyl) disulfide solution in ethanol for 24 h. Au/$SC_{11}O_2F_7$ monolayers were prepared via immersion in a 0.5 mM bis (11,11'-dithioundecyl) perfluoroheptanoate solution in THF for 24 h. The samples were then removed, rinsed with ethanol and dried in a stream of nitrogen. Au/$SC_{11}O_2F_7$ monolayers were exposed to 0.1 M KOH (aq) for 5 min to form loosely packed monolayers of Au/$SC_{11}OH$.

Exchange Study

Loosely and densely packed Au/$SC_{11}OH$ monolayers were immersed in a 1.0 mM solution of n-docosanethiol (HSC_{22} adsorbate) in THF. The exchange process was monitored ex situ with RAIRS, ellipsometry, and contact angle goniometry before and after a 24 h exposure.

Results and Discussion

$Au/SC_{11}O_2F_7$ Monolayer Composition and Structure

We used RAIRS to investigate the composition and conformation of SAMs prepared from bis (11,11'-dithioundecyl) perfluoroheptanoate. Figure 7.2 shows the hydrocarbon and fluorocarbon regions of the IR spectra for all monolayers studied. The fluorocarbon region of the $Au/SC_{11}O_2F_7$ RAIR spectra consists mainly of peaks due to C-F stretching with the transition dipole moments perpendicular (υ_{pd} 1190-1270 cm^{-1}) or parallel (υ_{ax} 1300-1380 cm^{-1}) to the axis of the fluorocarbon helix.[19] The $Au/SC_{11}O_2F_7$ monolayer exhibits a υ_{pd} stretching peak at 1255 cm^{-1} and a υ_{ax} stretching peak at 1335 cm^{-1}. These positions compare well with those observed for SAMs prepared from partially fluorinated alkanethiols with similar chain lengths.[19] The relative intensity of the υ_{ax} to υ_{pd} intensities implies that the fluorocarbon segments are, on average, canted beyond that observed by us for a SAM prepared from a partially fluorinated alkanethiol ($F(CF_2)_6(CH_2)_{10}SH$) with similar chain length.[19] Well-packed, trans-extended hydrocarbon monolayers typically exhibit characteristic asymmetric ($\upsilon_{as}(CH_2)$) and symmetric ($\upsilon_s(CH_2)$) methylene absorbances at 2919 and 2850 cm^{-1}, respectively.[19] $Au/SC_{11}O_2F_7$ monolayers exhibit distinct $\upsilon_{as}(CH_2)$ and $\upsilon_s(CH_2)$ peaks at 2927 cm^{-1} and 2856 cm^{-1} (Table 7.1), indicative of a significant deviation from a trans-extended, crystalline hydrocarbon monolayer. This shift is consistent with reports of $\upsilon_{as}(CH_2)$ = 2929 cm^{-1} and $\upsilon_s(CH_2)$ = 2855 cm^{-1} by Schonherr and Ringsdorf for the ester linked bis(2,2'-dithioethyl) dodecanoate.[8] Ryswyk et al. reported a similar ester disruption of the hydrocarbon packing, $\upsilon_{as}(CH_2)$ = 2928 cm^{-1}, in SAMs formed from 11-

mercaptoundecyl isonicotinate on gold.[33] Previous results[19] suggest that the larger size of the fluorocarbon helix alone does not destroy the crystallinity of the underlying

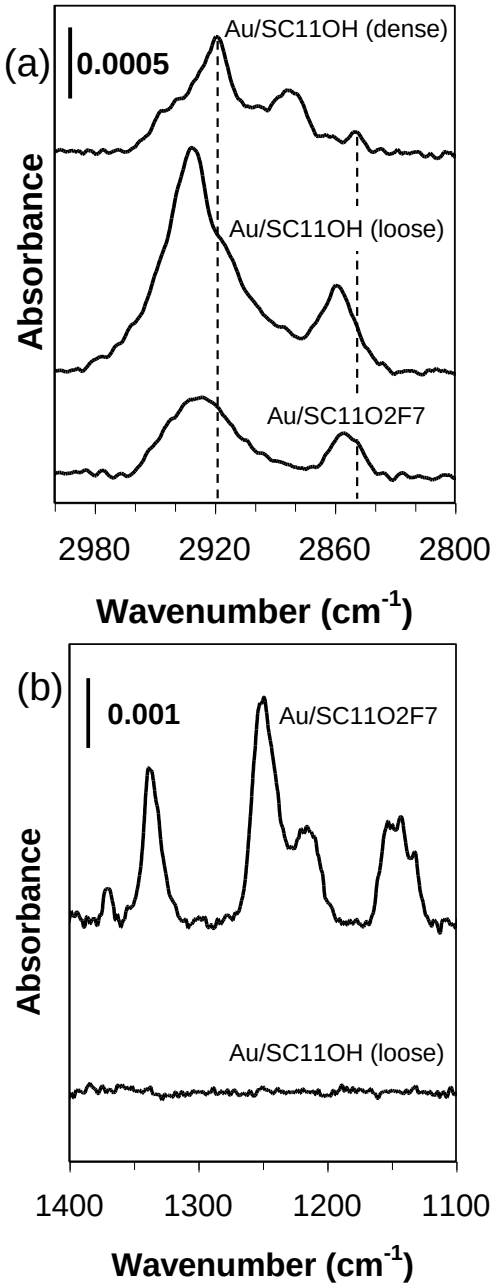

Figure 7.2. Reflectance-absorption infrared spectra of the (a) C-H and (b) C-F stretching regions for the indicated SAMs. The spectra have been offset vertically for clarity. The dashed lines in (a) represent the position of $\upsilon_{as}(CH_2)$ at 2919cm^{-1} and $\upsilon_{s}(CH_2)$ at 2849cm^{-1}, those observed in the dense Au/SC_{11}OH monolayer.

hydrocarbon region, $\upsilon_{as}(CH_2)$ = 2919 cm^{-1}, based on hexadecanethiols that were partially fluorinated in the outer region but did not contain an ester linkage. Thus, the $\upsilon_{as}(CH_2)$ and $\upsilon_s(CH_2)$ shifts are consistent with a poorly structured hydrocarbon region due to a disruption of hydrocarbon packing by the ester or a combined influence from the ester and the fluorocarbon terminal group.

Table 7.1. Peak Positions from RAIR Spectra

	Wavenumber (cm^{-1})		
Mode	$SC_{11}OH$ - dense	$SC_{11}OH$ – loose	$SC_{11}O_2F_7$
υ_{as} - CH_2	2919	2931	2927
υ_s - CH_2	2849	2860	2856
υ_{ax} – CF	-	-	1335
υ_{pd} – CF	-	-	1255

The thickness of the Au/$SC_{11}O_2F_7$ monolayer (20 Å, Table 7.2) agrees well with the 21 Å thickness[34] of Au/$S(CH_2)_{11}(CF_2)_{10}F$ monolayer. The experimental thickness is lower than that reported for a 20 equivalent carbon monolayer prepared from eicosanethiol (25 Å).[35] The discrepancy in thickness is likely due to the estimation of refractive index for both the Au/$SC_{11}O_2F_7$ and the Au/$S(CH_2)_{11}(CF_2)_{10}F$ monolayers as that for a purely hydrocarbon monolayer (1.45). The true refractive index of the partially fluorinated monolayer is most likely between that of a hydrocarbon and a fluorocarbon film (1.37).[36] For our Au/$SC_{11}O_2F_7$ monolayer, a highest possible experimental thickness was found to be 23 Å by fitting the ellipsometric data using a refractive index of 1.37.

We used contact angle measurements to qualitatively assess the surface composition of Au/$SC_{11}O_2F_7$ monolayers (Table 7.2). Advancing contact angles of water (127°) and hexadecane (78°) indicate hydrophobic and oleophobic surface properties and are consistent with a predominate perfluoromethyl (-CF_3) surface.[23] The advancing contact angle of hexadecane, which is ~3° lower than that measured on a partially fluorinated SAM prepared from $HS(CH_2)_{10}(CF_2)_6F$, suggests that some -(CF_2)- functionality is exposed at the outermost interface and is consistent with the increased average cant of the fluorocarbon terminal groups here.[19] This difference in contact angle and fluorocarbon cant is likely due to structural perturbations caused by the fluorinated ester linkage. The combined analyses imply a structure for the Au/$SC_{11}O_2F_7$ SAM in which the fluorocarbon chains are slightly canted on average to expose a predominate -CF_3 surface, and the hydrocarbon chains underneath are disordered and in a loosely packed state.

Table 7.2. Water and Hexadecane Advancing and Receding Contact Angles (deg) and Ellipsometric Film Thicknesses for Monolayers on Gold

	water		hexadecane		
Monolayer	θ_A	θ_R	θ_A	θ_R	thickness (Å)
$SC_{11}OH$ - dense	20 ± 4	< 10	<15	~ 0	11 ± 1
$SC_{11}OH$ - loose	68 ± 3	43 ± 7	<15	~ 0	10 ± 1
$SC_{11}O_2F_7$	127 ± 2	109 ± 2	78 ± 2	65 ± 2	20 ± 1

Influence of $SC_{11}OH$ Packing Density on Monolayer Structure

Exposure of the Au/$SC_{11}O_2F_7$ SAM to 0.1 M KOH(aq) for 5 min results in complete removal of the fluorocarbon helix via base-mediated hydrolysis, as evidenced by the complete diminution of peaks in the fluorocarbon region of the spectrum (Figure

7.2b). This hydrolysis yields a loosely packed Au/$SC_{11}OH$ monolayer. The loose packing is confirmed by the position of $\upsilon_{as}(CH_2)$ and $\upsilon_s(CH_2)$ peaks at 2931 and 2860 cm^{-1}, indicating significant shifts from those of the Au/$SC_{11}O_2F_7$ SAM. The poor packing inferred via RAIRS demonstrates the lack of formation of densely packed domains due to surface diffusion. In addition, the increase in $\upsilon_{as}(CH_2)$ and $\upsilon_s(CH_2)$ intensities for the loosely packed Au/$SC_{11}OH$ monolayer indicates a greater average chain cant as compared to the hydrocarbon segment within the Au/$SC_{11}O_2F_7$ SAM. This relaxation of the hydrocarbon chains, likely motivated by intermolecular hydrogen bonding,[37] provides further support that the fluorocarbon terminal group governs the packing in the pre-cleaved Au/$SC_{11}O_2F_7$ SAM.

From Figure 7.2a and Table 7.1, the densely packed Au/$SC_{11}OH$ monolayer prepared by direct adsorption of $(S(CH_2)_{11}OH)_2$ exhibited asymmetric and symmetric methylene peak positions at 2919 and 2849 cm^{-1}, indicative of a crystalline monolayer. The enhancement in the methylene peak intensity for the loosely packed Au/$SC_{11}OH$ monolayer over that for the densely packed monolayer is attributed to the increased cant of the hydrocarbon chains in the loosely packed state, which increases the surface normal component of the transition dipole moment of the CH_2 stretching vibration and hence, its absorbance.[38]

The average cant angle can be estimated from the RAIRS intensity via the relationship of peak intensity (I) to the average angle between the transition dipole moment and the surface normal (θ_{mz}) [38]

$$I \propto \cos^2(\theta_{mz}) \tag{7-1}$$

From equation 1, we estimate θ_{mz} for both the $\upsilon_{as}(CH_2)$ and $\upsilon_s(CH_2)$ peaks and determine an average all-trans alkyl chain cant of 59° from the surface normal for the loosely packed Au/$SC_{11}OH$ SAM by assuming a 30° cant for the densely packed monolayer.[39] This estimation of cant angle corresponds to a 40% lower thickness for the loosely packed monolayer as compared to the densely packed monolayer and is in agreement with a theoretical estimation of a 33% lower thickness than the densely packed monolayer, based solely on the lateral area occupied by a fluorocarbon helix versus a hydrocarbon chain. The agreement between RAIR results and theory draws attention to the small change in ellipsometric thickness (~1 Å; 9%) between the well packed and loosely packed Au/$SC_{11}OH$ SAMs and more notably, the low thickness of the well packed Au/$SC_{11}OH$ (11 Å). While other authors have also reported comparable thicknesses values[35,40-42] for well packed Au/$SC_{11}OH$ monolayers, the actual thickness is likely more comparable to that of a well packed monolayer prepared from n-dodecanethiol (16 Å).[43] If the thickness for the densely packed SAM is indeed 16 Å, RAIRS estimations yield a thickness for the loosely packed SAM of 11 Å, which is comparable to our ellipsometric thickness of 10Å. Despite the disagreement between RAIRS and ellipsometric thickness results, both methods quantitatively demonstrate the cleaved Au/$SC_{11}OH$ SAM in a less dense state when compared to that of a well packed monolayer prepared by adsorption of $(S(CH_2)_{11}OH)_2$.

The advancing water contact angles for the loosely packed Au/$SC_{11}OH$ monolayer were not consistent with that of a well packed, pure hydroxyl surface. The low packing density of the monolayer likely exposes methylene functionality at the surface in addition to the hydroxyl terminal group, resulting in a mixed surface yielding

an intermediate surface energy. The most widely adopted method for determination of composition at surfaces with mixed functionality is the Cassie equation [44]

$$\cos\theta_{meas} = \varphi_{OH}\cos\theta_{OH} + (1-\varphi_{OH})\cos\theta_{CH2} \quad (7\text{-}2)$$

where φ_{OH} denotes the fraction of the surface with hydroxyl functionality, θ_{meas} is the measured contact angle (68°), θ_{OH} is the measured contact angle on a pure hydroxyl surface (~20°), and θ_{CH2} is the reported contact angle on a methylene-terminated surface (~107°).[44] From eq 2, we estimate that 54% of the surface is covered by hydroxyl groups and the remainder by methylene groups due to the loosely packed nature of the SAM.

Barrier Properties

We used electrochemical impedance spectroscopy (EIS) to investigate the barrier properties of the monolayers in the presence of $K_3Fe(CN)_6$ and $K_4Fe(CN)_6$ in 0.1 M Na_2SO_4 (aq). Representative impedance spectra in the form of Bode plots are presented in Figure 7.3. The symbols indicate experimental data, where the solid lines represent the fits of the data using appropriate equivalent circuit models.[45]

Based on the fits of impedance spectra by equivalent circuit models, mean charge transfer resistances and film capacitances for each of the monolayers are compiled in Table 7.3. The Au/$SC_{11}O_2F_7$ monolayer (R = $1.26\text{x}10^4$ Ω cm^2) is a markedly poorer barrier than monolayers of similar composition without an ester linkage ($HS(CH_2)_{10}(CF_2)_6F$) (R = $1.4\text{x}10^6$ Ω cm^2) that we have previously studied.[19] The lower resistance for the Au/$SC_{11}O_2F_7$ SAM implies that this monolayer contains a much higher

density of defects than the SAMs prepared from partially fluorinated thiols and is qualitatively consistent with the structure (fluid-like hydrocarbon, canted fluorocarbon)

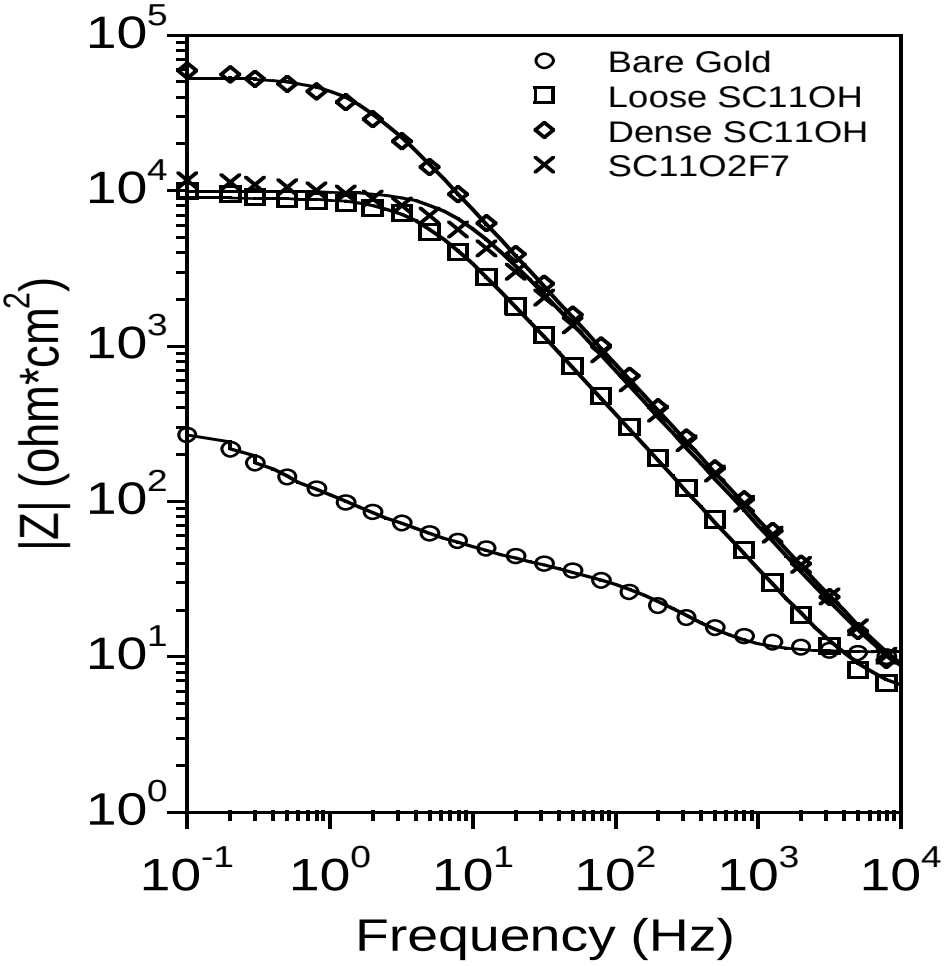

Figure 7.3. Electrochemical impedance spectra obtained in 1 mM $K_3Fe(CN)_6$ and 1 mM $K_4Fe(CN)_6$ in 0.1 M Na_2SO_4 (aq) for monolayers on gold. Spectra are shown for -$SC_{11}O_2F_7$, densely packed -$SC_{11}OH$ and loosely packed -$SC_{11}OH$, and bare gold (for reference). Solid curves represent fits of the data using appropriate equivalent circuit models.

and wettability (more -CF_2- groups exposed) of the monolayer. These defects are most likely distributed across the surface and result from inefficient monolayer packing caused by the fluorinated ester linkage. Thus, while steric effects due to inefficient filling of

defect sites may play a role, that effect is expected to be smaller than the two order of magnitude decrease in resistance that we observe here. This large effect is more likely due to the ester linkage between the hydrocarbon and fluorocarbon, which may work in two ways to weaken barrier properties. First, the ester region is a layer of ion affinity within the monolayer. This layer could act as an ion "stepping stone" across the hydrophobic hydrocarbon and fluorocarbon regions. The second affect of the ester is to perturb the monolayer chain packing in both the hydrocarbon and fluorocarbon regions, leading to defects and free space for water and ion transfer. The perturbation of the hydrocarbon chain packing can be seen in the RAIR spectra (Figure 7.2a) in the shift of the $\upsilon_{as}(CH_2)$ and $\upsilon_s(CH_2)$ peaks towards higher wavenumbers. The perturbation of the fluorocarbon region is most apparent in the increased cant of the fluorocarbon termini and the lower hexadecane contact angles as compared to CF_3-terminated monolayers without the ester linkage.[19]

When the ester in the $Au/SC_{11}O_2F_7$ is cleaved, the resulting loosely packed $Au/SC_{11}OH$ monolayer has a higher capacitance than the pre-cleaved state due to the decrease in monolayer thickness,[46] but surprisingly, both the cleaved and pre-cleaved monolayers have similar resistances against ion transfer. This impedance behavior suggests either that the fluorocarbon terminal group has a negligible effect on the resistance or more likely, that the relaxation of the hydrocarbon upon cleaving reduces some of the pathways for ion transfer that existed in the less canted, pre-cleaved state to yield a comparable resistance, even in the absence of the fluorocarbon terminus. Either of these interpretations implies that the free volume in the hydrophobic region near the Au surface is a dominant factor in film resistance. Consistent with this conclusion, a

densely packed Au/$SC_{11}OH$ monolayer exhibits a factor of 5 higher resistance and 46% lower capacitance than that of the loosely packed Au/$SC_{11}OH$ monolayer. The resistance is higher in the well packed monolayer due to a higher density of the hydrocarbon chains at the Au surface that reduce pathways for ion transfer. The enhanced thickness of the densely packed monolayer, combined with the lower free volume for water uptake, also results in significantly lower capacitance as compared with the loosely packed monolayer.

Table 7.3. Values for Monolayer Capacitance and Resistance In Water and THF/Water

	water		THF/water	
monolayer	C_{dl} ($\mu F/cm^2$)	log (R_f) ($\Omega \cdot cm^2$)	C_{dl} ($\mu F/cm^2$)	log (R_f) ($\Omega \cdot cm^2$)
$SC_{11}OH$ - dense	2.4 ± 0.3	4.7 ± 0.4	2.4 ± 0.6	5.0 ± 0.2
$SC_{11}OH$ - loose	3.5 ± 0.7	4.0 ± 0.4	4.1 ± 0.6	4.4 ± 0.3
$SC_{11}O_2F_7$	2.2 ± 0.3	4.1 ± 0.4	-	-

Barrier Properties with a THF Cosolvent

The alteration of the barrier properties of a film by cosolvent addition provides insight into the ability of the cosolvent to penetrate into the film. In a similar cosolvent study, French et al.[47] proposed a explanation for an observed enhancement of well-packed monolayer barrier properties through the use of 1-octanol as an aqueous cosolvent. They attributed the increase in barrier properties to octanol filling the defect sites within alkanethiolate SAMs. We studied the influence of a THF cosolvent on the impedance behavior of the loose and well packed $SC_{11}OH$ monolayers due to its strong solvation of the $SC_{11}OH$ adsorbate. THF was added (1:3 vol., THF:water) as a cosolvent to the aqueous ferrocyanide and ferricyanide solution. In the dense monolayer, the film

capacitance remained unchanged while the charge transfer resistance doubled. While in the loosely packed monolayer, the film capacitance increased by 19 ± 5 % and the charge transfer resistance also doubled. The increases in capacitance and resistance were observed in all six runs of this experiment. An increase in both resistance and capacitance is unusual and is plausibly attributed to an intercalation of THF into the monolayer. In the dense monolayer, the THF would only be able to intercalate into the film at defect sites in the monolayer. The filling of the defect sites would increase the charge transfer resistance, which is greatly affected by defect density, while, the capacitance of the well-packed film would be relatively unaffected, represented by the dense THF-impenetrable domains. In the loose monolayer, THF could conceivably intercalate into the entire film, increasing ion transfer inhibition in a similar manner and magnitude to that of the dense monolayer. The 19% increase of the capacitance is attributed to the intercalated THF ($\varepsilon = 7.6$)[48] increasing the dielectric constant of the film from near that of polyethylene ($\varepsilon = 2.3$)[21] to a higher value.

Table 7.4. Water and Hexadecane Contact Angles and Ellipsometric Film Thicknesses after 24 h Exchange with HSC22

	water		hexadecane		
monolayer	θ_A	θ_R	θ_A	θ_R	thickness (Å)
$SC_{11}OH$ - dense	82 ± 8	46 ± 7	<15	~ 0	22 ± 2
$SC_{11}OH$ - loose	112 ± 4	88 ± 6	41 ± 2	18 ± 1	27 ± 2
SC22 (control)	114 ± 2	98 ± 1	48 ± 1	37 ± 1	27 ± 1

Exchange of the Monolayer with $HS(CH_2)_{22}H$

Exchange or displacement of adsorbates within a SAM by competing adsorbates in solution is an important step in the preparation of complex, multifunctional

interfaces.[28] Several prior studies agree that the most rapid exchange in well packed SAMs occurs at isolated defect sites;[28-31] thus, loosely packed SAMs that exhibit a high density of defect sites may enable a more uniform and rapid exchange. Here, we expose both loose and dense Au/$SC_{11}OH$ monolayers, in addition to a bare gold surface (control), to a 1 mM solution of $C_{22}SH$ in THF for 24 h to assess the extent of exchange or incorporation of the long-chained thiol (Table 7.4). The 24 h exposure to $C_{22}SH$ results in a nearly complete exchange of the loosely packed monolayer based on thicknesses and contact angles that approach those values for the complete Au/SC_{22} monolayer. In contrast, the dense Au/$SC_{11}OH$ monolayer is only partially exchanged. In particular, the hexadecane contact angle for the loosely packed surface after a 24 h exchange (41°) is approaching that of a well packed Au/SC_{22} surface (48°), whereas that of the densely packed surface after exchange (<15°) remains low, indicating large areas of poor -SC_{22} coverage. Contact angle hysteresis is commonly used as a measurement of surface homogeneity, where a low hysteresis is consistent with highly uniform, homogeneous surfaces. The relatively high water contact angle hysteresis (36°) and low advancing water contact angle (82°) observed on the densely packed Au/$SC_{11}OH$ monolayer after exchange are indicative of a mixed, heterogeneous surface. The lower contact angle hysteresis in the loosely packed $SC_{11}OH$ monolayer after exchange supports our assertion that the loosely packed monolayer fosters a more rapid and extensive exchange process that provides a more uniformly exchanged surface. We attribute the more extensive exchange in the loosely packed system to engineered defect sites located more uniformly across the monolayer, as opposed to the localized defect site propagation[29] for the well packed monolayers. In the loosely packed Au/$SC_{11}OH$

monolayer, these defect sites, which have been shown above to allow for water, ion, and solvent penetration, allow for rapid thiolate insertion into the monolayer, resulting in a faster exchange and a more homogeneous surface. A more uniform and rapid exchange, as demonstrated here, can be powerful in the preparation of complex interfaces through place exchange reactions.[28]

Conclusions

The preparation of fluid-like, hydroxyl-terminated SAMs on gold is easily achieved via base-mediated cleavage of an ester bound fluorocarbon terminal group. The resulting loosely packed films have greater chain spacing and defect density, reduced thicknesses, and intermediate surface energy. The larger alkyl chain spacing, when compared to its well packed analogue, creates a more permeable SAM with decreased barrier properties against water, ion, and solvent transport. The additional chain spacing in the loose SAMs enabled more uniform and extensive thiolate exchange behavior unlike the defect-mediated exchange propagation of well packed SAMs. These hydroxyl-terminated SAMs should prove useful in the preparation of polymer/gold linkages with a reduced resistance to proton transfer.

References

1. Choi, E. J.; Foster, M. D.; Daly, S.; Tilton, R.; Przybycien, T.; Majkrzak, C. F.; Witte, P.; Menzel, H. *Langmuir* **2003,** 19, (13), 5464-5474.

2. Lahann, J.; Mitragotri, S.; Tran, T. N.; Kaido, H.; Sundaram, J.; Choi, I. S.; Hoffer, S.; Somorjai, G. A.; Langer, R. *Science* **2003,** 299, (5605), 371-374.

3. Choi, E. J.; Foster, M. D. *Langmuir* **2002,** 18, (2), 557-561.

4. Chaudhury, M. K.; Whitesides, G. M. *Science* **1992,** 256, (5063), 1539-1541.

5. Xu, S.; Cruchon-Dupeyrat, S. J. N.; Garno, J. C.; Liu, G. Y.; Jennings, G. K.; Yong, T. H.; Laibinis, P. E. *Journal of Chemical Physics* **1998,** 108, (12), 5002-5012.

6. Stranick, S. J.; Atre, S. V.; Parikh, A. N.; Wood, M. C.; Allara, D. L.; Winograd, N.; Weiss, P. S. *Nanotechnology* **1996,** 7, (4), 438-442.

7. Chen, S. F.; Li, L. Y.; Boozer, C. L.; Jiang, S. Y. *Journal of Physical Chemistry B* **2001,** 105, (15), 2975-2980.

8. Schonherr, H.; Ringsdorf, H. *Langmuir* **1996,** 12, (16), 3891-3897.

9. Schonherr, H.; Ringsdorf, H.; Jaschke, M.; Butt, H. J.; Bamberg, E.; Allinson, H.; Evans, S. D. *Langmuir* **1996,** 12, (16), 3898-3904.

10. Tsao, M. W.; Rabolt, J. F.; Schonherr, H.; Castner, D. G. *Langmuir* **2000,** 16, (4), 1734-1743.

11. Noh, J.; Hara, M. *Langmuir* **2000,** 16, (5), 2045-2048.

12. Heister, K.; Allara, D. L.; Bahnck, K.; Frey, S.; Zharnikov, M.; Grunze, M. *Langmuir* **1999,** 15, (17), 5440-5443.

13. Ishida, T.; Yamamoto, S.; Mizutani, W.; Motomatsu, M.; Tokumoto, H.; Hokari, H.; Azehara, H.; Fujihira, M. *Langmuir* **1997,** 13, (13), 3261-3265.

14. Garg, N.; Lee, T. R. *Langmuir* **1998,** 14, (14), 3815-3819.

15. Park, J. S.; Smith, A. C.; Lee, T. R. *Langmuir* **2004,** 20, (14), 5829-5836.

16. Park, J. S.; Vo, A. N.; Barriet, D.; Shon, Y. S.; Lee, T. R. *Langmuir* **2005,** 21, (7), 2902-2911.

17. Lee, S.; Shon, Y. S.; Colorado, R.; Guenard, R. L.; Lee, T. R.; Perry, S. S. *Langmuir* **2000,** 16, (5), 2220-2224.

18. Bao, H. F.; Peng, Z. Q.; Wang, E. K.; Dong, S. J. *Langmuir* **2004,** 20, (25), 10992-10997.

19. Weinstein, R. D.; Moriarty, J.; Cushnie, E.; Colorado, R.; Lee, T. R.; Patel, M.; Alesi, W. R.; Jennings, G. K. *Journal of Physical Chemistry B* **2003,** 107, (42), 11626-11632.

20. Fukushima, H.; Seki, S.; Nishikawa, T.; Takiguchi, H.; Tamada, K.; Abe, K.; Colorado, R.; Graupe, M.; Shmakova, O. E.; Lee, T. R. *Journal of Physical Chemistry B* **2000,** 104, (31), 7417-7423.

21. Brandup, J.; Immergut, E. H.; Grulke, E. A., *Polymer Handbook*. Fourth ed.; Wiley: New York, NY, 1989.

22. Schonherr, H.; Vancso, G. J., AFM Study on Lattice orientation and tribology of sams of fluorinated thiols and disulfides on Au(111) by AFM: The influence of the molecular structure. In *Fluorinated Surfaces, Coatings, and Films*, 2001; Vol. 787, pp 15-30.

23. Brantley, E. L.; Jennings, G. K. *Macromolecules* **2004,** 37, (4), 1476-1483.

24. Imabayashi, S.; Hobara, D.; Kakiuchi, T. *Langmuir* **2001,** 17, (9), 2560-2563.

25. Ko, B. S.; Babcock, B.; Jennings, G. K.; Tilden, S. G.; Peterson, R. R.; Cliffel, D.; Greenbaum, E. *Langmuir* **2004,** 20, (10), 4033-4038.

26. Dordi, B.; Schonherr, H.; Vancso, G. J. *Langmuir* **2003,** 19, (14), 5780-5786.

27. Schonherr, H.; Feng, C. L.; Shovsky, A. *Langmuir* **2003,** 19, (26), 10843-10851.

28. Hostetler, M. J.; Templeton, A. C.; Murray, R. W. *Langmuir* **1999,** 15, (11), 3782-3789.

29. Collard, D. M.; Fox, M. A. *Langmuir* **1991,** 7, (6), 1192-1197.

30. Nishida, N.; Hara, M.; Sasabe, H.; Knoll, W. *Japanese Journal of Applied Physics Part 1-Regular Papers Short Notes & Review Papers* **1997,** 36, (4A), 2379-2385.

31. Schlenoff, J. B.; Li, M.; Ly, H. *Journal of the American Chemical Society* **1995,** 117, (50), 12528-12536.

32. Shah, R. R.; Merreceyes, D.; Husemann, M.; Rees, I.; Abbott, N. L.; Hawker, C. J.; Hedrick, J. L. *Macromolecules* **2000,** 33, (2), 597-605.

33. VanRyswyk, H.; Turtle, E. D.; WatsonClark, R.; Tanzer, T. A.; Herman, T. K.; Chong, P. Y.; Waller, P. J.; Taurog, A. L.; Wagner, C. E. *Langmuir* **1996,** 12, (25), 6143-6150.

34. Colorado, R. J.; Graupe, M.; Shmakova, O. E.; Villazana, R.; Lee, T. R. In *Structural Properties of Self-Assembled Monolayers (SAMs) on Gold Generated from Terminally Fluorinated Alkanethiols*, Washington, DC, 2001; Overney, J. E. F. a. R., Ed. American Chemical Society: Washington, DC, 2001; pp 276-292.

35. Bain, C. D.; Troughton, E. B.; Tao, Y. T.; Evall, J.; Whitesides, G. M.; Nuzzo, R. G. *Journal of the American Chemical Society* **1989,** 111, (1), 321-335.

36. Sandrin, L.; Silverstein, M. S.; Sacher, E. *Polymer* **2001,** 42, (8), 3761-3769.

37. Tsukamoto, K.; Kubo, T.; Nozoye, H. *Applied Surface Science* **2005,** 244, (1-4), 578-583.

38. Nuzzo, R. G.; Dubois, L. H.; Allara, D. L. *Journal of the American Chemical Society* **1990,** 112, (2), 558-569.

39. Porter, M. D.; Bright, T. B.; Allara, D. L.; Chidsey, C. E. D. *Journal of the American Chemical Society* **1987,** 109, (12), 3559-3568.

40. Whitesides, G. M.; Laibinis, P. E. *Langmuir* **1990,** 6, (1), 87-96.

41. Li, X.; Wei, X. L.; Husson, S. M. *Biomacromolecules* **2004,** 5, (3), 869-876.

42. Sabapathy, R. C.; Crooks, R. M. *Langmuir* **2000,** 16, (4), 1777-1782.

43. Jennings, G. K.; Laibinis, P. E. *Journal of the American Chemical Society* **1997,** 119, (22), 5208-5214.

44. Laibinis, P. E.; Palmer, B. J.; Lee, S.-W.; Jennings, G. K., The Synthesis of Organothiols and their Assembly into Monolayers on Gold. In *Thin Films*, Ulman, A., Ed. Academic Press: Boston, 1998; Vol. 24, pp 1-41.

45. The spectra for SC11O2F7 and loose and well packed SC11OH are fit to a traditional Randle's equivalent circuit, consisting of a solution resistance (Rs) in series with both a film resistance (Rf) and double layer capacitance (Cdl) in parallel. For these SAMs the solution resistance dominates in the high frequency range of the Bode plot, while the film capacitance and resistance are the dominant factors in the intermediate and low frequency ranges, respectively. The spectrum of bare gold is provided as a reference, and is the only spectrum fit by an equivalent circuit incorporating a Warburg impedance in series with the charge transfer resistance in the traditional Randle's equivalent circuit. The Warburg impedance results from mass transfer limitations caused by rapid charge transfer between the redox probes and the bare gold surface.

46. Jennings, G. K.; Munro, J. C.; Yong, T. H.; Laibinis, P. E. *Langmuir* **1998,** 14, (21), 6130-6139.

47. French, M.; Creager, S. E. *Langmuir* **1998,** 14, (8), 2129-2133.

48. Israelachavilli, J., *Intermolecular & Surface Forces*. Second ed.; Academic Press: 1992.

CHAPTER VIII

CONCLUSIONS AND FUTURE WORK

Conclusions

In this body of work, we aimed to take initial steps toward the development of technologies which allow for a more controlled, idealized integration of the elements of the membrane electrode assembly (MEA) in proton exchange membrane (PEM) fuel cells. The MEA is traditionally prepared from bulk solution casting methods[1-4] which lead to poorly defined interfaces and low utilization of catalyst.[2] Our bottom up approach integrates the cathode, gas diffusion layer, catalyst layer and ionomer (Figure 1.2).

The results presented in Chapter IV demonstrate the sequential and rapid reactions used in the preparation of surface-initiated ROMP-type poly(n-alkylnorbornene) films. Uniformity in surface coverage is dependent upon the length of the n-alkyl side chain on the monomer. Films prepared from butylnorbornene and hexylnorbornene yield dense films whereas decylnorbornene polymerizes into discrete polymer clusters. The length of the monomer side chain is inversely proportional to the reactivity of the monomer and limits the maximum possible film thickness using Grubbs first generation catalyst. The surface energy of the polyalkylnorbornene films is decreased beyond that of a polynorbornene film by the methyl terminus of the alkyl side chain. With the exception of the clustered polydecylnorbornene film, the polyalkylnorbornene films offer greater resistance against redox probes as compared to polynorbornene films.

The internal olefin groups of ROMP-type films enable further reactive processing including sulfonation to provide proton conductivity to the films. In Chapter V, surface-tethered sulfonated polymer films are prepared through the exposure acetyl sulfate to surface-initiated ROMP-type films. Film loss is observed through ellipsometric thickness measurements and was independent of the sulfonation agent. Film loss likely occurs as a result of cleavage at the olefin site which is present in the backbone of all ROMP-type polymers. The sulfonation process results in a non-uniform surface morphology which can be relaxed to a more uniform surface through exposure to DMSO. The component of the sulfonated film's resistance to proton transfer is small and attributed to the polymer linkage to the metallic support. The developed ionomer system is promising for inclusion into the proposed integrated electrode network.

Loosely-packed hydroxyl terminated self assembled monolayers (SAMs) are prepared in an effort to reduce the resistance at the ionomer / gold interface. Loosely packed SAMs are achieved through the cleavage of an ester-bound fluorocarbon group. The resulting films have larger interchain spacing and defect density, as well as lower film thickness and an intermediate surface energy. The loosely packed film has a lower impedance to redox probes than of its traditionally prepared anologue.

The deposition of a platinum-based catalyst for oxygen reduction was investigated on a planar gold substrate. Platinum is deposited through a two-step process requiring the underpotential deposition of a sub-monolayer of copper followed by the electroless replacement of the copper adlayer with platinum. The platinum adlayer is catalytically active in the oxygen reduction reaction. The activity of the catalyst is preserved during the deposition of a sulfonated polynorbornene ionomer overlayer.

Nanoporous gold substrates can be prepared through the exposure of an alloy of gold and silver to nitric acid. The nanoporous gold substrate demonstrates a 10x improvement in surface area available for copper underpotential deposition. Platinum is deposited onto the nanoporous gold substrate in a fashion analogous to the planar gold substrate. The platinum-coated nanoporous support has a marginally improved oxygen reduction current than that of the platinum coated planar substrate. The incorporation of the sulfonated polynorbornene into the platinum coated support decreases the oxygen reduction capacity of the electrode, likely due to poor oxygen permeability in the ionomer as well as reduced volume for oxygen transport within the nanoporous support.

Future Work

Development of a Fluorinated Surface-Initiated Ionomer

Fluorinated ionomers offer many advantages over purely hydrocarbon ionomers. The nature of proton transport through traditional ionomers is based on the reorganization of the ionomer into hydrophilic and hydrophobic domains.[2,5] The greater hydrophobicity of fluoropolymers would result in a larger driving force for reorganization and lower resistances to proton transport.[6] Fluorinated ionomers also have greater oxygen permeability than current hydrocarbon ionomers.[7] Poor oxygen transport is the likely cause of reduced catalytic activity in our integrated electrode structures, and a fluorinated ionomer should increase power output in our electrode assemblies.

While norbornene monomers with fluoroalkyl side chains are not commercially available, they can be synthesized though a Diels-Alder approach (Figure 8.1). The

Diels-Alder reaction is class of cycloaddition reactions between an alkene and a conjugated diene. The reaction applicable to this research is the reaction of cyclopentadiene and a partially fluorinated 1-alkene to form a mixture of endo and exo isomers of the appropriate alkyl-norbornene. While the endo product is predominant in the Diels-Alder reaction due to a favorable overlap of *p* orbitals,[8] it is the exo product that is more ROMP active. If the activity of the exo isomer is desired, isolation of the isomers is possible via low pressure distillation.[9]

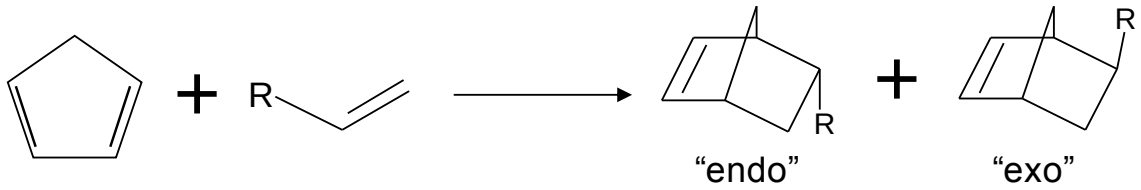

Figure 8.1. Diels-Alder reaction to generate functionalized norbornenes. R represents a partially fluorinated 1-alkene.

Preparation of Alternative Nanoporous Electrodes

Porous electrodes with high surface area offer the ability to greatly enhance power per geometric area and seamlessly integrate catalyst, gas diffusion channels, and proton conducting ionomer into a single network. We have demonstrated preparing such porous electrodes, where commercially available Ag/Au alloy leaf structures (100 nm thick) were dealloyed and deposited onto a substrate. A greater control over the processing of these electrodes could be obtained by preparing our own alloy structures for subsequent dealloying and porosity development. Jia et al.[10] have recently shown that Zn can be electrodeposited atop Au, Ag, and Cu films and heated at low temperatures (150 °C) to

induce alloy formation. Dealloying of this system produces porous Au, Ag, or Cu electrodes.

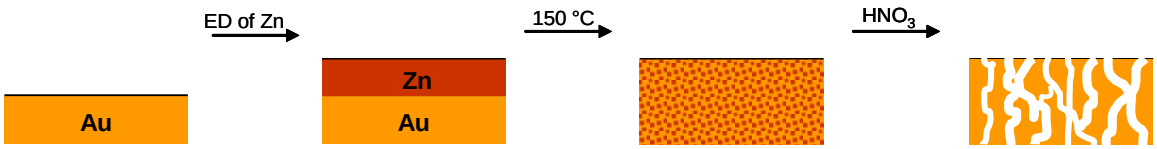

Figure 8.2. Proposed approach for preparing NPG films by electrodeposition of Zn, annealing to alloy, and dealloying by etching to produce a porous gold film.

Inspired by the method of Jia et al.[10] (Figure 8.2), we can use the dealloying process to prepare nanoporous gold electrodes in which thickness (50 – 300 nm), pore diameter (20-100 nm), and porosity (30 – 70%) are controlled to investigate fundamental interfacial issues including surface area, catalyst integration, and ionomer attachment/composition on the cathodic reaction. The thickness of the nanoporous electrode film is proportional to the thickness of the deposited gold (vacuum deposition or electroless) and the ultimate porosity after dealloying, which is dependent on the initial amount of Zn electrodeposited atop the gold surface up to thermodynamic saturation limits. Average pore size can be varied from ~20 nm to ~100 nm by exposure time of the alloy to the dealloying solution. Through this process, we could fabricate porous electrodes to enable tremendous control over further processing, including catalyst and ionomer deposition. These electrodes could be grown onto any surface that supports a thin gold film, and alternately, could be transferred from one surface to another through interfacial bonding and detachment.

Extension to Carbon Supports

Surface-initiated ROMP can be performed from virtually any surface provided that an appropriate metathesis catalyst can be attached in a preceding step. To extend the ionomer to carbon supports (carbon cloth, carbon black, etc.), we would first generate alcohol functionality on the carbon surface by exposure to formaldehyde or through oxidation in nitric acid (Figure 8.3).[11] The resulting alcohol groups will then be exposed to a norbornene containing di(acid chloride) groups to generate a covalent ester linkage of the norbornene to the carbon surface. If the surface alcohols are sufficiently spaced that only one ester linkage is created, then the unreacted acid chloride will be converted to a carboxylic acid by rinsing in water. We have performed analogous chemistry by using alcohol-modified gold surfaces. The surface-attached norbornene will bind Grubbs' first generation catalyst, which can then be used to grow the target polymer from the carbon surface.

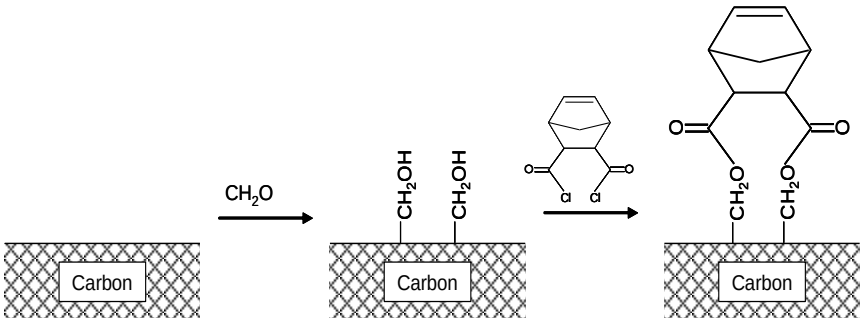

Figure 8.3. Modification of carbon supports to allow for SI-ROMP. The attached norbornene will bind Grubbs' First generation catalyst to enable polymerization of the various monomers described herein.

Based on the research of others, we expect to graft from 1 in ~250 surface carbons,[12] but the degree of polymerization for surface-initiated ROMP is such that the

carbon surface should be well coated. A selective feature of this ionomer growth is that it will occur only from carbon so that any Pt present as catalyst, such as adsorbed onto a carbon nanoparticle, will not be functionalized. Surface-initiated ROMP offers advantages in kinetics, composition, and internal structuring when compared to other approaches for growing ionomer from carbon supports.[11,12]

New Electrochemical Characterization of Ionomers

Figure 8.4 shows a schematic of a test cell that we could use to measure the performance of our integrated 3-D cathodes. Protons are conducted through a bulk membrane (Nafion®) to the top of the 3-D cathode while oxygen is fed through the bottom. The use of a bulk membrane is motivated to assess any impedance to proton transfer from the membrane to the porous electrode and the role of interfacial ionomer in facilitating this transfer. We can vary thickness, average pore size, and porosity of the electrode, in addition to the ionomer composition, thickness, and attachment to investigate these pertinent interfacial effects on the oxygen reduction reaction and on the overall impedance of the system. For each ionomer composition and attachment, we seek to measure the limiting current by continually increasing the flux of protons in excess O_2 until the electrode interface can no longer provide an increase in current. This would enable us to quantify performance benefits for the following effects: fluorocarbon versus hydrocarbon side groups, ion channel orientation, chemisorbed versus non-bound, and extent of pore filling. Such information could be used to molecularly optimize the interfacial environment within these 3-D electrodes and provide guidelines for the molecular design of interfaces for other geometries and types of fuel cells.

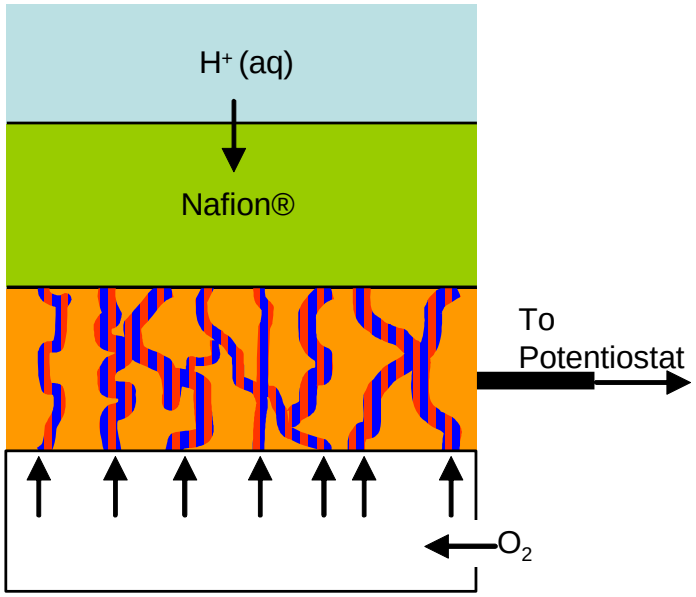

Figure 8.4. Experimental setup to test performance of catalyst-ionomer integrated 3-D cathodes through voltammetry or impedance.

References

1. Barbir, F., *PEM Fuel Cells: Theory and Practice*. Elsevier Academic Press: Boston, 2001.

2. Middelman, E. *Fuel Cells Bulletin* **2002**, (11), 9-12.

3. Mehta, V.; Cooper, J. S. *Journal of Power Sources* **2003,** 114, (1), 32-53.

4. Litster, S.; McLean, G. *Journal of Power Sources* **2004,** 130, (1-2), 61-76.

5. Saito, M.; Arimura, N.; Hayamizu, K.; Okada, T. *J. Phys. Chem. B* **2004,** 108, 16064-16070.

6. Suresh, G.; Pandey, A. K.; Goswmi, A. *Journal of Membrane Science* **2007,** 295, (1-2), 21-27.

7. Ayad, A.; Bouet, J.; Fauvarque, J. F. *Journal of Power Sources* **2005,** 149, 66-71.

8. Sauer, J.; Sustmann, R. *Angewandte Chemie-International Edition in English* **1980,** 19, (10), 779-807.

9. Seehof, N.; Grutke, S.; Risse, W. *Macromolecules* **1993,** 26, (4), 695-700.

10. Jia, F.; Yu, C.; Deng, K.; Zhang, L. *J. Phys. Chem. C.* **2007,** 111, 8424-8431.

11. Mizuhata, H.; Nakao, S.; Yamaguchi, T. *Journal of Power Sources* **2004,** 138, (1-2), 25-30.

12. Qin, S.; Qin, D.; Ford, W. T.; Resasco, D. E.; Herrera, J. E. *Macromolecules* **2004,** 37, 752-757.

APPENDIX A

PROPERTIES OF POLYNORBORNENE FILMS GROWN USING NORBORNENE FROM DIFFERENT COMMERCIAL SOURCES

There are several suppliers for norbornene. In the preparation of this manuscript, we used norbornene from two sources and observed differences between norbornene supplied from MP Biomedicals (99%) and norbornene supplied from Acros (99%). Monomers were used as received. Features similar to those seen in the Acros material have been observed by other research groups[1,2] in norbornene (purity not specified by authors) supplied by Aldrich.

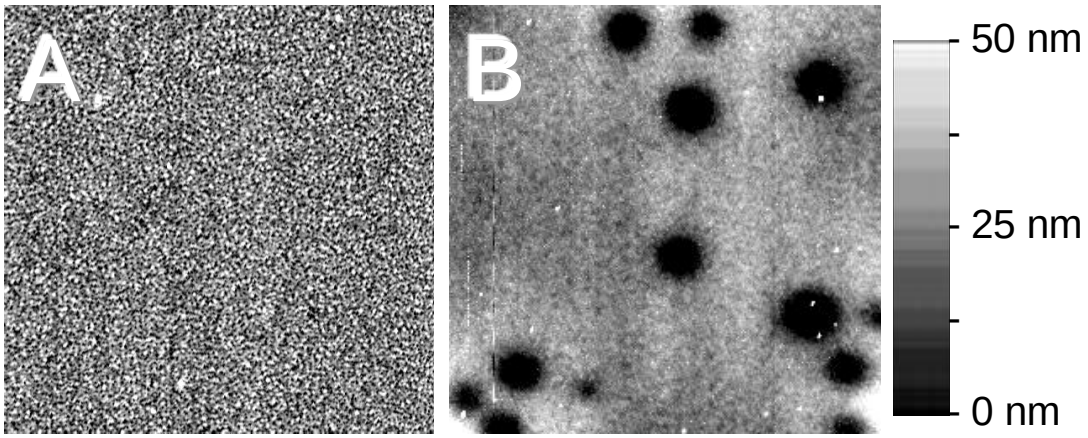

Figure A.1. AFM images (25 μm x 25 μm) of pNB films grown from norbornene from MP Biomedicals (A) and Acros (B).

Table A.1. Film Capacitance, Resistance and Ellipsometric Thickness Values for pNB films

film	thickness (nm)	$\log(R_f)$ ($\Omega \cdot cm^2$)	C_f (nF/cm^2)	Z_w ($\Omega \cdot s^{-1/2}$)
pNB - MP Biomedicals	49 ± 2	4.3 ± 0.6	250 ± 170	11000 ± 17000
pNB – Acros	41 ± 5	2.9 ± 0.4	790 ± 300	490 ± 260

References

1. Rutenberg, I. M.; Scherman, O. A.; Grubbs, R. H.; Jiang, W.; Garfunkel, E.; Bao, Z. *J. Am. Chem. Soc.* **2004,** 126, 4062-4063.

2. Rutenberg, I. M., *Functionalized Polymers and Surfaces via Ring-Opening Metathesis Polymerization*. California Institute of Technology: Pasadena, CA, 2005.